ELECTRON AND LIGHT EMISSION FROM ISLAND METAL FILMS AND GENERATION OF HOT ELECTRONS IN NANOPARTICLES

R.D. FEDOROVICH, A.G. NAUMOVETS, P.M. TOMCHUK

Institute of Physics, National Academy of Sciences of Ukraine, 46 Prospect Nauki, UA-03039, Kiev 39, Ukraine

ELSEVIER

AMSTERDAM – LAUSANNE – NEW YORK – OXFORD – SHANNON – TOKYO

ELSEVIER

Physics Reports 328 (2000) 73–179

PHYSICS REPORTS

www.elsevier.com/locate/physrep

Electron and light emission from island metal films and generation of hot electrons in nanoparticles

R.D. Fedorovich, A.G. Naumovets*, P.M. Tomchuk

Institute of Physics, National Academy of Sciences of Ukraine, 46 Prospect Nauki, UA-03039, Kiev 39, Ukraine

Received July 1999; editor: G. Comsa

Contents

* Corresponding author. Fax: +(380) 44 265 15 89.
E-mail address: naumov@iop.kiev.ua (A.G. Naumovets)

PII: S0370-1573(99)00094-0

Abstract

We review experimental and theoretical works devoted to electron and photon emission from island metal films (IMFs) representing ensembles of small metal particles deposited onto a dielectric substrate and coupled via penetrable potential barriers. Electrons and photons are emitted when the films are energized by passage of current through them or by laser irradiation. In either case the primary recipient of the energy is the electron gas, which can be heated up to temperatures much higher than the particle lattice temperature. A theoretical substantiation of the model of hot electrons in nanoparticles is presented. The major physical factor that permits generation of hot electrons in IMFs is the dramatic reduction (by orders of magnitude) of the electron–lattice energy transfer in the particles whose size is smaller than the mean free path of electrons in the volume. In such particles with a ballistic motion of electrons, the energy is being lost mainly in surface scattering acts which are less effective in energy transfer than generation of volume phonons. Thus, the electron temperature can become substantially higher than the lattice temperature provided the absorbed power density is high enough and the lattice of the island is intensively cooled by the substrate. The model of hot electrons is used to interpret experimental data. Non-equilibrium electron heating in IMFs can be observed even under stationary conditions, so the island metal films basically differ in their electronic properties from continuous metal films and bulk metals where hot electrons can be obtained only for very short times ($\leq 10^{-11}$ s). Thus, the island metal films represent an important variety of nanomaterials having rather unusual physical properties. IMFs can be utilized to fabricate cathodes having interesting application potentialities in vacuum microelectronics, information display technologies and infrared image conversion. Hot electrons generated in nanoparticles may also play a significant role in various dispersed systems exposed to energy fluxes.

PACS: 73.50.Fq; 79.60.Jv; 78.66.Vs; 73.61.Tm; 36.40.Vz; 79.40. + z

Keywords: Island films; Nanoparticles; Hot electrons; Electron emission; Photon emission; Optical absorption

1. Introduction and outline

Various kinds of dispersed systems have attracted intense interest for many decades due to their peculiar properties caused by the fact that these objects represent ensembles of small particles. As the size of the particles R is being reduced, the number of surface atoms in relation to that of volume atoms is growing as R^{-1}. Thus, the specific surface area of dispersed matter can attain huge values, and many aspects of behaviour of such systems are known to be determined by surface processes. This is actually a geometric size effect. However, there are a number of other size effects which come into play whenever the particle size becomes equal to some characteristic physical length like the electric field screening length, mean free path of electrons, de Broglie wavelength, etc.

An interesting example of dispersed systems are island metal films (IMFs), representing quasi-two-dimensional ensembles of small particles. Such films can easily be prepared, e.g. by evaporating a small amount of metal upon a dielectric substrate which is unwettable by the metal. If the mean distance between the metal islands is small enough, the islands are coupled by electron tunneling and thus represent an entity. Nevertheless, the properties of such an object carry an imprint of the properties of the small particles making up the film. Important factors that determine the peculiar characteristics of IMFs are: size effects in properties of small particles; the ability of such particles to pass high-energy fluxes without destruction due to strong cooling effect of the substrate; the tunnel coupling between the particles; possible existence of high local fields around them. Interest in IMFs was sparked more than 30 years ago when Borziak, Fedorovich and Sarbei discovered that passing a current through an IMF gives rise to electron and light emission originating from some small ($\leq 1\,\mu m$) spots called emission centers [1]. Later on, the same effect was observed in the films being irradiated by a sufficiently powerful infrared laser beam [2–4] or microwave radiation [5].

This field has a comparatively extensive literature, including some monographs and reviews. The first 15 years of investigations on IMFs were summarized in Borziak and Kulyupin's monograph [6]. The subject was also partially covered in Nepijko's book [7] published in 1985. Switching phenomena in IMFs were reviewed by Pagnia and Sotnik ten years ago [8]. There is also our brief review which summarizes more recent works [9]. Meanwhile, a considerable progress has been achieved quite recently both in understanding the physics of hot electrons in small metal particles and in applications of the island films. This problem starts to attract renewed interest in the context of the rapid advancement of nanophysics and nanotechnologies. Therefore we hope that a review giving a more or less self-contained coverage of the problem may be timely and useful, especially when one considers that many essential works are scattered over not easily accessible journals and proceedings.

This article is devoted mainly to phenomena of electron and light emission from island metal films and to nonequilibrium heating of electrons in small metal particles. The review is organized as follows. After this introductory section, we shall consider methods of preparation of IMFs (Section 2). Experimental data on the conductivity of IMFs and electron emission from them are presented in Section 3 which also discusses the main concepts suggested for interpretation of these results. Section 4 is concerned with light emission from the films. Sections 5–7 give a rigorous theoretical substantiation of the model of hot electrons in small metal particles. The readers who are not interested in the theoretical details, may skip these sections or just read their summaries. Examples of practical applications of IMFs are considered in Section 8. Finally, Section 9 contains

general conclusions as well as some remarks about outlooks for further studies in the field and possible implications of hot electrons in various dispersed systems. It should be noted that figures are numbered independently in each section.

Let us start with a closer look at the objects whose properties are discussed in this review: the island metal films (IMFs).

2. Island metal films: preparation and major experimental findings

2.1. Substrates and contact electrodes

Substrates for preparation of IMFs are made from various dielectric materials, most often from glass, quartz and mica. Their surfaces are cleaned by rinsing in standard chemical solutions and distilled water. In some studies the films were deposited on alkali-halide crystal surfaces which were obtained by cleaving the crystals immediately before the vacuum evaporation of the film.

The contact electrodes whose typical geometry is illustrated in Fig. 2.1 represent continuous films with thickness of ~ 100 nm which are prepared either by thermal evaporation in vacuum through a mask or by standard photolithographic technique. In the former case, there is a transition ("penumbral") region near the boundary of the continuous contact film where the film has an island structure with variable mass thickness (Fig. 2.2a). Its existence can substantially affect the growth and structure of the island film which is subsequently prepared in the gap between the contacts (see Section 2.2).

For structural studies by transmission electron microscopy, the island films were evaporated onto carbon films 10–30 nm thick deposited on meshes by the standard method. When structure and electrical characteristics were investigated in parallel, special substrates were used representing thin mica plates with a hole in the middle for passing the electron beam (Fig. 2.3). Each plate was first entirely (including the hole) coated with a Formvar film about 20 nm thick, and then a 50 nm SiO_x film was deposited over the Formvar sublayer. In the next step this sublayer was removed from the hole by heating at 150–200°C leaving there only the SiO_x film. This film served as the substrate for deposition of Au contact electrodes (by evaporation through a mask) and of an island film to be studied in the electron microscope. To prevent electrostatic charging of the SiO_x film by the probing electron beam, its rear side was coated with a carbon layer 5–10 nm thick.

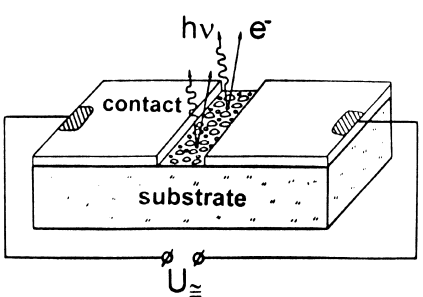

Fig. 2.1. Schematic of the sample with an island film between two contact electrodes.

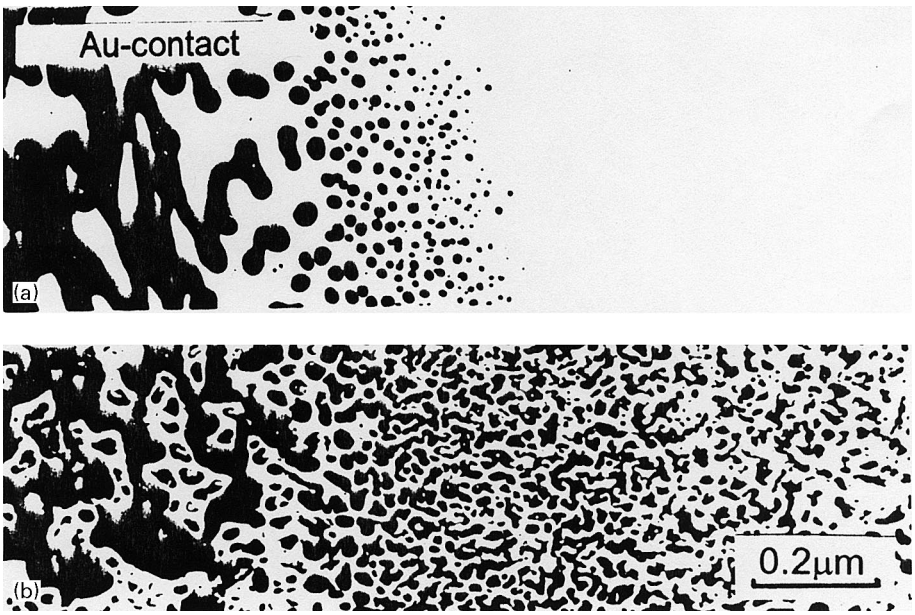

Fig. 2.2. (A) A "penumbral" region near the edge of a contact electrode. (B) Structure of an Au island film with a mass thickness of 5 nm near the contact with the "penumbral" edge.

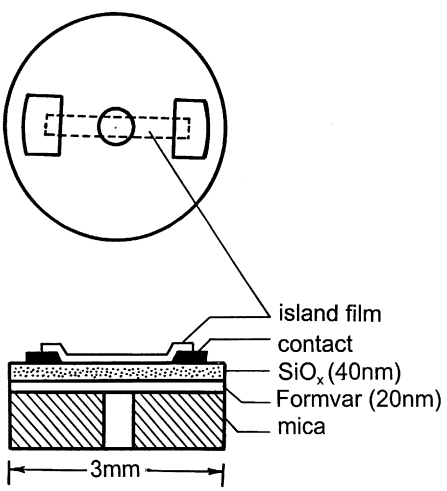

Fig. 2.3. Schematic of a sample for in situ electron microscopic experiments with IMFs.

2.2. Preparation of IMFs

The simplest way of preparation of IMFs is vacuum evaporation of a metal onto a dielectric substrate [10]. One can also apply cathode sputtering in a noble gas atmosphere [11], electrodeposition from solutions [12] as well as spraying of a suspension containing fine solid particles

[13]. Up to now, the most widely used method has been vacuum evaporation. The metals utilized for fabricating IMFs have been Au, Ag, Pd, Pt, Cu, Cr, Mo and some others. Graphite island films also show very good characteristics. It is seen that metals with sufficiently high melting points, whose atoms have a comparatively low mobility at room temperature, are deposited. This ensures a reasonably good stability of the film properties. Prior to preparing the island film, a pair of contact electrodes is deposited on the substrate as considered in the previous section. Then a smaller amount of a metal is additionally evaporated upon the whole surface which allows one to create an island film within the gap between the contacts (Fig. 2.2b). Typically the gap is about 10 μm.

Since metals normally do not wet dielectric surfaces, the equilibrium growth mode corresponds in this case to the Volmer–Weber mechanism [14]. Thus, if the mass thickness of the deposited film is small enough, the metal atoms coalesce during deposition or subsequent annealing into islands to minimize the surface and interface free energy [15–17]. The nuclei appearing at the early stage of the film growth have an atomic size. They grow three-dimensionally as the metal deposition is continuing, but their dimension parallel to the surface increases much faster than normal to the surface (Fig. 2.4). The average size of the islands and their distribution over the substrate depend on many factors such as temperature of the substrate, evaporation rate, the mass thickness of the evaporated film, the chemical nature of the adsorbate and the substrate as well as on the temperature and duration of subsequent annealing. It is also well known that the spatial arrangement of the islands is sensitive to the presence and nature of surface defects (the decoration of the defects by metal atoms is routinely used in electron microscopy to visualize atomic steps and other surface imperfections). By choosing all the factors listed above, one can vary the parameters of IMFs within broad limits. The late stages of deposition result in coalescence of adjacent islands, then in the attainment of the percolation limit at some critical coverage, and finally in the formation of a continuous film. Typically, the mass thickness of IMFs described in this article is about 4–10 nm.

The evolution of the structure of growing island films could be investigated simultaneously with measurements of their electrical properties immediately in an electron microscope equipped with a built in vacuum chamber [18]. A pressure of $\sim 10^{-8}$ Torr around the sample under study was provided by differential pumping. In other works, investigations of this type have been performed in a high-vacuum electron microscope [19]. To study the structure of the films deposited on thick substrates, it is necessary either to transfer the film onto another substrate which is transparent for electrons in the transmission electron microscope or to use the well-known method of replicas. In any case the film must be protected from changes which may occur while carrying the sample through atmosphere. This is achieved by coating the film, prior to its exposure in air, with a layer of SiO_x or carbon about 30–40 nm thick. The films obtained on 50 nm SiO_x substrates are the most convenient objects, since all the measurements can be carried out in situ. The method of preparation of such substrates has been described in Section 2.1.

The electron microscopic investigations have shown that the size distribution of the islands is rather wide: there are relatively few islands about 10^2 nm in size and at the same time a large number of nanosized islands in between. It is also evident that the structure of the deposited island film can be peculiar in the "penumbral" region of the contacts where these electrodes themselves have an island structure. Such peculiarities do occur and are manifested both in a nonuniform potential drop across the film when a voltage is applied to it [20] and even in a specific optical

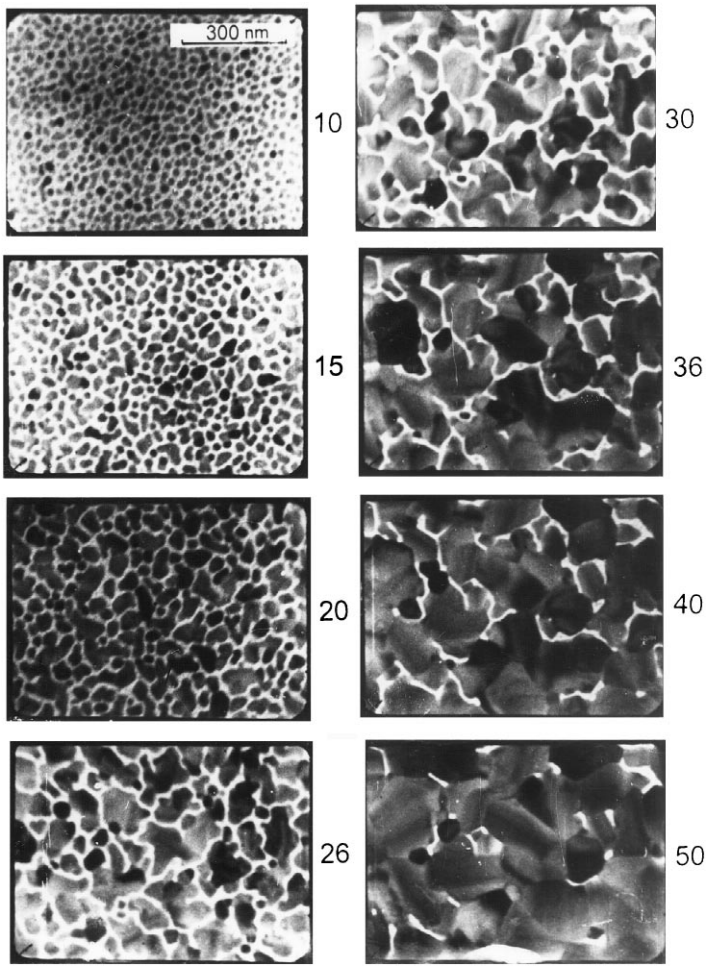

Fig. 2.4. Structure of thin Bi films on a carbon substrate at various mass thicknesses (in nm). Substrate temperature during Bi evaporation was 100°C [21].

absorption in the near-contact areas [21]. If the edges of the contact electrodes are sharp, as e.g. in the case when the gap is obtained by scratching a continuous film (Fig. 2.5), the structure of the island film forming in the gap is found to be statistically homogeneous.

Although our review is focused on the properties of metal island films, it is appropriate to mention here the possibilities of preparation of semiconductor island films, since some experiments reveal similarity in emission properties of metal and semiconductor films (see Section 3.6). In principle, there are no obstacles to fabrication of semiconductor island films. Actually the corresponding methods have been (and are being) intensively developed in connection with investigations of quantum dots [22–24]. In Section 3.6, we describe a method in which a Si island film is obtained as a result of controlled evaporation of thin Si single crystal epitaxially grown on sapphire.

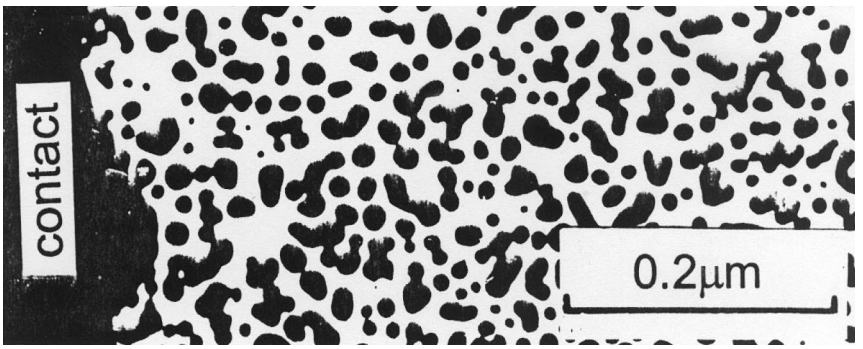

Fig. 2.5. Structure of an Au island film on glass substrate near the contact electrode with a sharp edge. The mass thickness of the film is 4 nm.

An important physical effect that probably can be used to better control the properties of island films is a pronounced self-organization which occurs, under proper conditions, in the course of thin film growth. This phenomenon has been much investigated in recent years (see e.g. [22–33]). The process starts at submonolayer coverages and continues at later stages when mesoscopic islands are being formed. Diverse mechanisms are predicted to drive the self-organization [34–36]. The most universal of them seems to be connected with elastic strains induced in the substrate by the growing film. Due to this effect, both the distances between the islands and the size of the islands can have rather narrow distributions around their average values. For example, the size of the islands can be obtained uniform to within $\pm$ 10% [22,23], supposedly due to reduction in adatom attachment probability caused by strain around the islands.

2.3. Electroforming of IMFs

The current channels with emission centers in them can be electroformed in films of various thickness (from island films to semicontinuous ones) [6,8].

It has been found that the flow of a conduction current through the film is a necessary condition of its electroforming. Indeed, experiments carried out at rather high electric fields (up to $\sim 5 \times 10^5$ V/cm parallel to the substrate surface) have shown that the presence of such a field alone (without current) does not produce any appreciable effect on the island film properties [37]. Some other authors [15] reported on sensitivity of the film structure to the electric fields as low as $\sim 10^3$ V/cm, but their experiments were made at film thicknesses when a considerable current could pass through their films [38].

To electroform a gold or silver island film of "standard" geometry (see Section 2.1), it is usually sufficient to raise the voltage applied to the film up to about 20–30 V for a time of 0.5–2 min. The island films prepared from refractory metals are electroformed at somewhat higher voltages. The presence of overlayers such as BaO or some organic species on IMFs facilitates the electroforming process, probably due to reduction of the surface free energy. The electroforming can also be carried out by applying a pulsed voltage of about 100 V at a pulse width of the order of milliseconds.

The electroforming proceeds more controllably when the contact electrodes have a special geometry which favours the emergence of the current channels in some particular places. The same effect is attained in chain island films (see Section 2.5).

The current flow, which first sets in at increased voltages only, seems to induce the process of electromigration in the film facilitated by some Joule heating, which results in the formation of clear-cut tunneling percolation paths ("current channels") and, as a consequence, in a sharp and irreversible decrease of the film resistance [39]. The current channels can be visualized with the aid of a thermosensitive film deposited on the surface of a sample through which a current is passed [40]. The film becomes decolorized over the channels, which can be seen under an optical microscope. The current channels were also investigated at a higher resolution by electron microscopy [41]. With this aim, the island films were prepared on thin SiO_x substrates transparent to probing electrons (see Section 2.1). The evaporation of the films as well as the investigation of their structure, conductivity and emission characteristics were performed in situ. To reveal the current channels, the films deposited between the contacts were decorated by a very thin metal layer [42]. When a current is passed through the film, the previously deposited decorating metal atoms drift along the channels (and maybe are partially evaporated from them, since the current density in the channels can amount to 10^6–10^7 A/cm^2). If the decoration is being made while passing the current, one obtains the impression that the decorating atoms are not at all adsorbed by the channels. Thus the channels appear as winding light lines (Fig. 2.6) [41].

High-resolution electron microscopy has shown that the current channel consists of an ultra-dispersed system of nano-islands separated by nm distances. They are coupled with each other by a tunneling process and in this way provide a continuous conduction path in the film. The channels contain also a small number of larger islands which are shaped in the process of electroforming.

Thus, after irreversible switching of the film to the low-resistance state, an appreciable conduction current flows even at voltages 5–10 V, much lower than those used for electroforming, and this current is concentrated predominantly within the individual channels. It is just in the electroformed

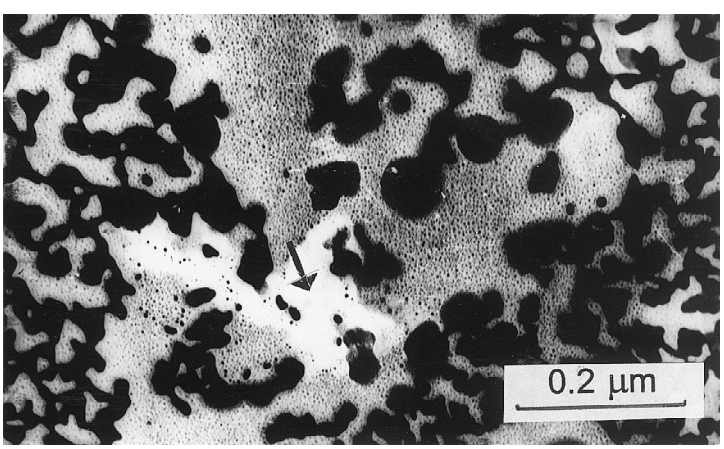

Fig. 2.6. An Au-decorated island film of Au on SiO_x with a region previously identified as an emission center. The decoration with Au was carried out while a current passed through the film. The current channel shown by an arrow appears as a light path, since Au being evaporated was carried away from it.

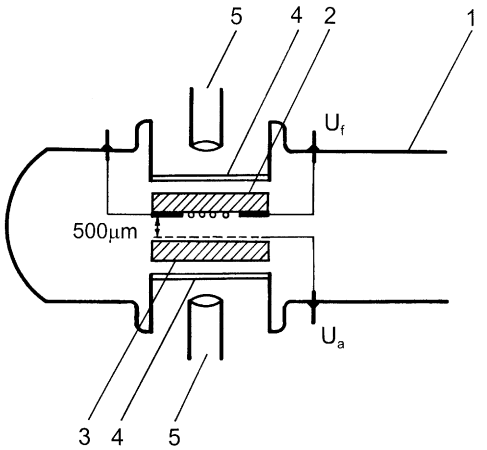

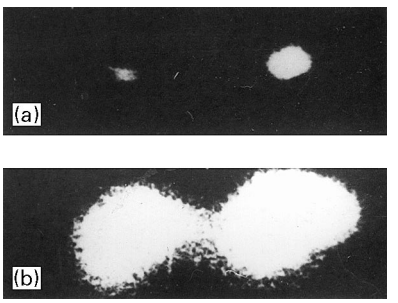

Fig. 2.7. A device for simultaneous observation of electron and light emission centers. 1, a glass bulb, 2, the sample with an island film, 3, cathodoluminescent screen, 4, window, and 5, an optical microscope.

Fig. 2.8. Centers of light emission in an IMF (a) and the corresponding image of electron emission centers in the same film on a cathodoluminescent screen (b).

state of IMFs that Borziak et al. [1] discovered the electron and light emission which accompany the passage of the conduction current through the films. In the following sections, we shall give and discuss the emission characteristics in closer detail. At this point we only note that electrons and photons are emitted not from the whole film, but emerge from small areas (spots) sized $\leq 1\,\mu m$ and termed emission centers. This was found in a device where the spatial distribution of emitted electrons was visualized on a cathodoluminescent screen [43] (Fig. 2.7). It was also stated that, within the resolution provided by optical microscopy, the emission of electrons and photons originates from the same centers (Fig. 2.8). Under an optical microscope, the centers appear as spots somewhat different in colour and scattered rather chaotically over the film. A colour micrograph of the luminous centers in a gold island film was published in the first work on the emission effects in IMFs [1]. As the voltage applied between the contact electrodes is increased, the emission current and light intensity grow both due to increase of the emissivity of each center and due to possible appearance of new centers. However, some centers can be extinguished if the applied voltage becomes too high and induces irreversible changes in the film structure.

2.4. Emission centers

Electron microscopic investigations have shown that the emission centers are located within the current channels, one center per channel [44,45]. The location of the emission centers is actually unpredictable on the substrates with flat surfaces prepared by ordinary methods such as mechanical polishing or cleavage. This is caused by the uncontrolled configuration of the current channels which reflects the statistical character of the nucleation of the islands. A typical emission center is a structure consisting of a relatively large ($\sim 100\,nm$) island surrounded by nano-sized islands (Fig. 2.9) [44]. Such configurations are created in the course of electroforming. It is well known that

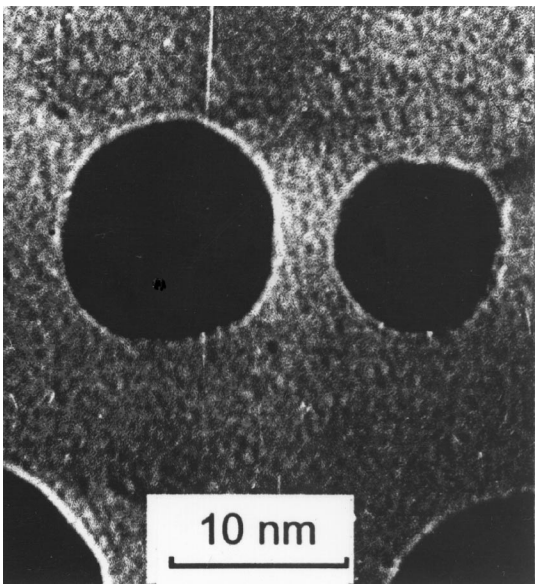

Fig. 2.9. Structure of an Au island film in the vicinity of an emission center. The substrate is a SiO_x film 50 nm thick.

in the process of the Ostwald ripening of dispersed systems the large particles are growing at the sacrifice of smaller ones due to the difference of the saturation vapour pressures over them. Thus, the emergence of local configurations "a large island + nano-islands around it" should be quite probable, and such structures have indeed been documented in many works on thin films (see e.g. a recent paper [31] and references therein). However, as noted above, usually a single emission center appears within a current channel so the number of the centers in a film cannot be larger than the number of the channels in it. There is a depletion zone around the large island and due to this a considerable potential drop occurs at this place. As will be shown in Section 3.4, this plays an important role in the electron and photon emission from IMFs, since a substantial part of the power fed into the current channel is released within the center.

The process of electromigration in IMFs is so far poorly investigated. Generally, the phenomenon of electromigration is rather complicated and highly sensitive to the chemical nature and the structure of systems under study. For example, electromigration in a number of bulk metals (Al, Ag, Au, In, Sn) and in their continuous thin films is driven by the scattering of electrons ("electron wind"), i.e. occurs towards the anode [46–50]. The films of the same metals being deposited on a semiconductor surface grow by the Stranski–Krastanov mechanism, i.e. form a continuous monolayer with three-dimensional islands on it, and often exhibit electromigration towards the cathode (see e.g. review [51]). Probably, the emission centers arise as a result of an intricate interplay between the structure of the film and the processes of electro- and thermal migration. In particular, electromigration depends on the local current density and resistivity, depending in turn on the film structure. If a considerable enhancement of the current density appears in some place in the current channel, it can be anticipated that the electromigration, perhaps combined with somewhat enhanced Joule heating, may cause a progressing destruction ("burning") of this segment

of the channel. This results in a growth of the voltage drop across this segment at the cost of the potential drop across the remaining parts of the channel. This avalanche-like process appears as a kind of instability of the uniform potential distribution which, however, does not lead to a complete burning of the channel if the voltage applied to the film is not too high. The result is that only one emission center survives in a channel. Probably, at some stage of the process there occurs a stabilization of the film structure through coming into play of a mechanism of self-limitation. This is mirrored in the fact that electroformed IMFs show practically stable conductivity and emission properties for thousands of hours under appropriate exploitation conditions (see Section 8). We have dwelt so much on this point, because it is just the segment in the current channel with a sharp potential drop across it that gives the electron and light emission. The mechanisms of this effect will be discussed in the following sections.

2.5. Chain island films

As noted in the previous section, the electroforming of the current channels and emission centers in them is actually a poorly controlled process on the substrates with flat surfaces prepared by standard methods. The electrons in the film are seeking paths with the lowest resistance where the electromigration forms eventually a well conducting percolation channel. Since the arrangement of the islands reflects a chaotic distribution of the nucleation centers (various defects), the shape of the current channels is usually very winding and their position is unpredictable. Correspondingly, the emission centers are also scattered rather randomly over the film. It was found, however, that the centers appear more frequently in the vicinity of the contact electrodes [52] which may reflect some specifics of the film structure in the "penumbral" regions of the contacts (see Section 2.1). For this reason the emission centers appear as a discrete and irregular chain stretched more or less parallel to the contacts.

There is, however, a possibility of making the process of the generation of emission centers in IMFs more controllable. To this end, the film is evaporated at a grazing angle onto a substrate whose surface is grooved (the incidence plane of the atomic beam is orthogonal to the grooves) (Fig. 2.10). Under such an evaporation geometry, the film has the largest mass thickness on the walls of the grooves whose orientation with respect to the atomic beam axis is closest to normal. After annealing, one obtains a film consisting of the chains of islands located in the grooves. A micrograph of such a film is given in Fig. 2.11. Such "chain" island films exhibit a high anisotropy

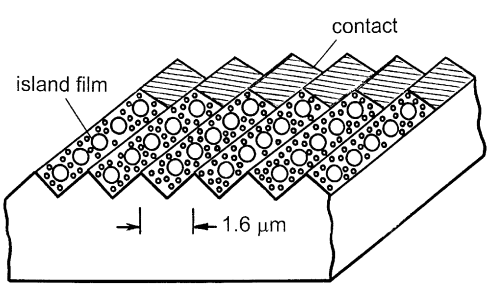

Fig. 2.10. Schematic of a grooved substrate with a chain island film on it.

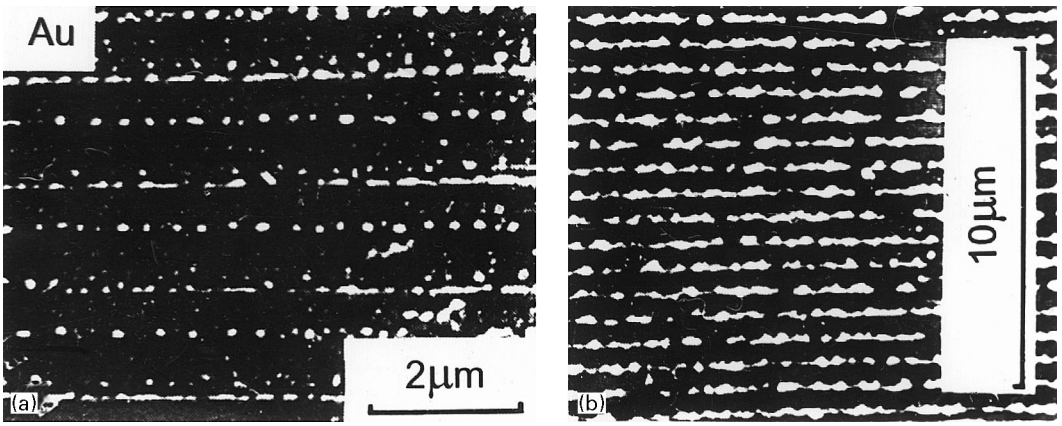

Fig. 2.11. Electron microscopic images of chain island films on (a) glass substrate with a diffraction grating and (b) a corrugated surface prepared by photolithography.

of conductivity: the ratio of the conductivities along and across the grooves (chains) amounts to $\sim 10^2$ [53].

An island chain appears as an almost ready current channel, and actually no special electroforming of the chain island film is needed for obtaining the electron and light emission from it. The emission is observed at once as a "normal" (not increased) operating voltage is applied to the film. It is interesting, however, that the potential drop along the chains nevertheless appears nonuniform. The region of an enhanced potential drop emerges in all the chains, and this region, which just marks the position of the emission center, is located for all chains at approximately the same distance from one of the contacts. As a result, the position of the emission centers in such a film is more controllable. Instead of randomly scattered luminous spots, one sees a narrow luminous strip formed by the individual centers located in all the grooves (chains). The strip is stretched across the grooves. Probably, the emergence of the emission centers in the chain films occurs faster and at lower voltages (below or equal to the operating voltage).

3. Electrical conductivity and electron emission properties of IMFs

3.1. Major experimental findings in brief

Experiments carried out in [1] and in later works on emission properties of IMFs have revealed the following main features.

(1) The conduction current–voltage characteristics of IMFs are linear at low voltages, but become superlinear at higher voltages.

(2) Electron emission and light emission set in at voltages at which the conduction current–voltage characteristics of IMFs exhibit deviation from Ohm's law. The emission is observed in both the continuous and pulse regimes. In the latter case, the measurements were made in the range of pulse durations $\tau = 10^{-7}$–10^{-3} s and frequencies $f = 1$–10^6 Hz.

(3) The conduction current grows substantially as an island film is covered with an overlayer that lowers the work function. For instance, the deposition of a BaO monolayer increases the conduction current by a factor of 10–15. At the same time, the emission current is enhanced by 3–4 orders of magnitude. Some organic overlayers cause the occurrence of a section of negative differential resistance in the conduction current–voltage characteristics of IMFs (see Section 3.5).

(4) The local density of the emission current estimated at the emission centers can amount to 10^6–10^7 A/cm^2. The total emission current can reach up to 10^{-2} of the total conduction current. The energy spectrum of the emitted electrons is rather broad. In the cases when it appears to be Maxwellian, the electron temperature amounts to $\sim 10^3$ K.

(5) The emitted light spectra usually have maxima in the red region, but deviate from the Planck law in the sense that they contain more energetic photons. The spectra are considerably narrower for the chain island films than for "irregular" ones.

(6) After the electroforming procedure in which the IMF structure and conductivity undergo substantial and rapid changes, the IMF properties are stabilized at a constant level. Under moderate exploitation conditions, they can be maintained for 10^3–10^4 h.

(7) The electron and light emission from IMFs can also be observed when the film is exposed to infrared laser radiation. In this case, previous electroforming of the island film is not required.

(8) The emission phenomena observed in IMFs occur also in the island films of semiconductors.

In Sections 3.2–3.7 we shall consider these points in detail. Let us start with the discussion of the conduction current–voltage characteristics which are very important for understanding the peculiar properties of IMFs.

3.2. Electrical conductivity of IMFs

The electrical conductivity of IMFs has been addressed in many papers and a number of monographs [54–58]. Their message is that the conductivity of IMFs on dielectric substrates is basically distinct from that of bulk metals and resembles to some extent the conductivity of semiconductors. The main questions are the mechanisms of charge transfer between the islands, the explanation of the non-ohmic conduction current–voltage characteristics and the exponential temperature dependence of the conductivity, the influence of adsorbates on the conductivity, and aging effects.

As mentioned above, the dependence of the conduction current *versus* voltage applied to an IMF obeys Ohm's law at weak fields, but deviates from it at $E \sim 10^3$–10^4 V/cm (E is the average electric field in the film) (Fig. 3.1). Within a narrow interval of thicknesses of IMFs, the temperature resistance coefficient is found to be negative. So a possible explanation for the superlinear conduction current–voltage characteristics could be the Joule heating of the islands. However, this hypothesis was discounted by the experimental data [59]. Since the dependence $\ln I_c$ versus $1/T$ appears linear in a given temperature range, some authors introduced the concept of the activation energy of conductivity, E_a. The value of E_a decreases with increasing mass thickness of the film and in the limiting case, as the metal film becomes continuous, the temperature resistance coefficient turns positive. In terms of E_a, the non-ohmic current–voltage characteristics were attributed to a change in the activation energy with increasing field and to a mechanism of "activated tunneling" [60]. Below, we shall describe another model, which substantiates the possibility of nonequilibrium

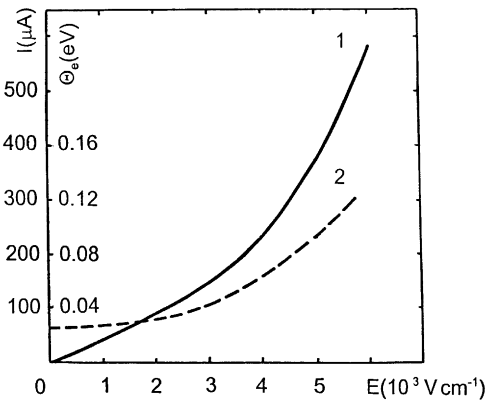

Fig. 3.1. Dependences of the conduction current (1) and electron temperature (2) on the average field strength in a 4 nm gold island film.

heating of electron gas in small particles and allows a consistent explanation of all unique electronic properties of IMFs.

Whatever the mechanism of the conductivity may be, the islands must exchange electrons and in the general case the current from the ith to the $(i+1)$th island can be written as

$$I_{i(i+1)} = e\int \Phi_{i(i+1)}(\mathscr{E}, T) D_{i(i+1)}(\mathscr{E}_x)\,\mathrm{d}\mathscr{E} \ . \tag{1}$$

Here $\Phi_{i(i+1)}(\mathscr{E}, T)$ is a function that determines the number of electrons with energy $\mathscr{E}$ which are able to pass from island i to island $(i+1)$ at temperature T, and $D_{i(i+1)}(\mathscr{E}_x)$ is the probability of the transition for an electron having an energy $\mathscr{E}_x$ connected with the motion along direction x. If an idealized system of identical islands located at equal distances from each other is placed in an external field, the total current will be equal to the difference of currents between the adjacent islands:

$$I = e\int [\Phi_{i(i+1)} - \Phi_{(i+1)i}] D(\mathscr{E}_x)\,\mathrm{d}\mathscr{E} \ . \tag{2}$$

To obtain an explicit dependence of the current on voltage, temperature, the film structure and electronic properties of the islands, it is necessary to specify the model. In principle, charge transfer between the islands can occur by means of thermionic emission into vacuum [61] or into the substrate [62], by tunneling through barriers metal–vacuum–metal or metal–substrate–metal [57,60,63–67], or by transport through impurity levels in the substrate [68]. For the films consisting of islands ~ 5 nm in size separated by distances 2–5 nm, the most probable mechanism seems to be the tunneling of electrons between the islands. Judging from the strong effect of adsorbed BaO molecules on the conduction current [69] and the weak sensitivity of this current to the substrate material [6], the tunneling should occur via vacuum.

The non-ohmic conduction current–voltage characteristics can be explained in terms of nonequilibrium heating of electrons in the IMFs at high electric fields [64,70]. One further

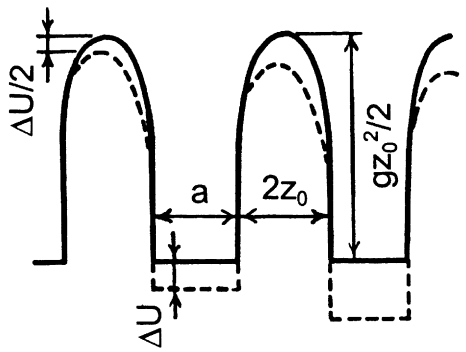

Fig. 3.2. A diagram of potential energy of an electron in an island metal film in the absence (solid line) and in presence (dashed line) of electric field. See text for explanations.

consequence of electron heating is electron emission from IMFs. Let us consider the concepts of this model in greater detail.

Suppose we have a linear chain of identical islands with equal spacings between them. The potential barriers separating the islands are assumed to be parabolic (Fig. 3.2):

$$U_0(z) = (gz_0^2/2) - (g/2)(z - z_0)^2 \ , \tag{3}$$

where $U_0(z)$ is the barrier height in the absence of electric field, $2z_0$ is the distance between the islands and g is a parameter. In the presence of an electric field the barrier is lowered and its maximum is displaced:

$$U_E(z) = (g/2)[z_0^2 - (z - z_0)^2] - eEz = (g/2)[z_0 - (eE/g)]^2 - (g/2)\{z - [z_0 - (eE/g)]^2\} \ . \tag{4}$$

Here $U_E(z)$ is the height of the barrier in point z in the presence of the field and e is the electron charge. Usually, the lowering of the barrier is not very strong, so one has $z_0 \gg eE/g$ and therefore

$$U_E(z) = (gz_0^2/2) - eEz_0 - \{z - [z_0 - (eE/g)]^2\} \ . \tag{5}$$

It can be seen that under the above assumptions the barrier is lowered by $eEz_0 = \Delta U/2$, where ΔU is the potential difference between the adjacent islands. The transparency of such a barrier is

$$D(\mathscr{E}) = \left\{\exp\left[-\frac{\mathscr{E} + (\Delta U/2)}{\varepsilon_0}\right] + 1\right\}^{-1} \ , \tag{6}$$

where $\varepsilon_0 = (h/2\pi)(g/m)^{1/2}$ is a parameter characterizing the barrier shape and m is the electron mass. Since the Fermi levels of the adjacent islands are shifted by ΔU, the electrons tunneling to an island from its neighbour are "hot" with respect to other electrons in this island. The redistribution of the excess energy between all electrons in the island results in a raising of the electron temperature. In principle, the functions $\Phi_{i(i+1)}(\mathscr{E}, T)$ in (1) can be distinct in different islands. The distinction can be caused, for instance, by different heating of the electron gas. For

simplicity, we assume the electron temperature to be equal in all the islands. Then the function $\Phi_{i(i+1)}(\mathscr{E}, T)$ can be taken as a Fermi function with an effective temperature θ_e (expressed in energy units), which depends on the power pumped into the island:

$$f(\mathscr{E}) = \left\{\exp\left(\frac{\mathscr{E}+\varphi}{\theta_e}\right)+1\right\}^{-1} . \tag{7}$$

Substituting (6) and (7) into Eq. (2) gives

$$I = A\int_{-\infty}^{\infty}\left\{1+\exp\left[-\frac{\mathscr{E}+(\Delta U/2)}{\varepsilon_0}\right]\right\}^{-1}\left\{1+\exp\left(\frac{\mathscr{E}+\varphi}{\theta_e}\right)\right\}^{-1} d\mathscr{E} \tag{8}$$

with $A = 4\pi me\Delta U/(2\pi\hbar)^3$.

To obtain an explicit dependence of the conduction current on voltage, temperature and other parameters, it is necessary to find the relationship between the electron temperature, the lattice temperature and the power fed into the film by passing current. The peculiarities of the dissipation of the energy of electrons in small particles will be treated at length in Sections 5 and 6. Here we note only that the motion of electrons is ballistic in the particles whose size is smaller than the electron mean free path in the bulk metal. For this reason electrons lose their energy in collisions with defects and with the island as a whole when they are reflected from the potential barrier. The reflection is almost elastic and the transferred momentum equals $\Delta p = 2p$, where p is the electron momentum. Thus the transferred energy is $\Delta\mathscr{E} = \mathscr{E}m/M$, where m and $\mathscr{E}$ are respectively the mass and energy of electron and M is the mass of the atom (or the island). It should be noted that the factor m/M, which determines the part of the energy lost by electron in a collision, remains somewhat uncertain. However, this fact need not concern us, since the factor enters into a phenomenological coefficient which may be determined from experiment. The number of collisions per unit time equals $1/\tau = v/a$, where v is the electron velocity and a is the island dimension. Hence the power transferred from an electron to the lattice is

$$\Delta P = \Delta\mathscr{E}/\tau \sim (\sqrt{m/M})(\mathscr{E}^{2/3}/a) . \tag{9}$$

The total power transferred by electrons to the whole film can be obtained by averaging (9) over the nonequilibrium component of the electron energy distribution and multiplying the result by the volume of the islands. Under steady-state conditions, this power must be equal to the power fed into the film $P = IU$, where U is the applied voltage. Hence the following expression can be obtained for the electron temperature:

$$\theta_e = kT_e = \sqrt{\theta_0^2 + \alpha^* IU} . \tag{10}$$

Here θ_0 is the lattice temperature in energy units and α^* is a coefficient which is independent of the field and temperature and determines the efficiency of electron heating. In the case $\varepsilon_0 > \theta_e$, the current is carried mainly by electrons tunneling near the Fermi level, because the barrier is rather steep and its transparency depends on energy less sharply than the electron energy distribution function. Then the expression for the current becomes

$$I = A\varepsilon_0 \exp(-\varphi/\varepsilon_0)\{1+(\pi^2/6)(\theta_e/\varepsilon_0)^2\}\exp(\Delta U/2\varepsilon_0) , \tag{11}$$

where φ is the work function. In the opposite case $\varepsilon_0 < \theta_e$, when the transparency depends on energy stronger than the distribution function, the current is carried predominantly by electrons tunneling near the top of the barrier and we obtain

$$I = A\theta_e \exp(-\varphi/\varepsilon_0)\{1 + (\pi^2/6)(\theta_e/\varepsilon_0)^2\} \exp(\Delta U/2\varepsilon_0) \ . \tag{12}$$

Thus, the maximum contribution to the tunneling current belongs to the group of electrons which are located at some distance from the Fermi energy, depending on the shape of the barrier (characterized by the parameter ε_0) and electron temperature θ_e. If θ_e is low, the tunneling occurs just above the Fermi level. As θ_e increases, the maximum of the tunneling flux is shifted to the top of the barrier. Some contribution to the conduction current can also originate from overbarrier electrons, but their part seems to be comparatively small (since the emission current is found to be much smaller than the conduction current, see Section 3.3). All these factors cause the deviation from the Ohm law.

In work [64], we proposed a method for determination of the model parameters ε_0 and α^*, and hence of the electron temperature, from the dependences of the conduction current on the applied voltage (field) and temperature. The typical electron temperature corresponding to beginning of the deviation of conduction current–voltage characteristics from linearity was found to be about 0.15 eV ($\approx 2 \times 10^3$ K) (Fig. 3.1). This model not only explains the variation of the conduction current versus electric field, temperature and work function, but also allows one to understand the main regularities of electron emission from the island films, which will be discussed in the following sections.

To conclude, a few additional comments are in order. Proposing the model of electron heating described above, we were guided by the following considerations. The deviation of the conduction current from Ohm's law and the occurrence of the electron and light emission (discussed in detail below) set in at approximately the same voltage applied to the film. This suggests that these phenomena should have a common cause. Such a cause may be the generation of hot electrons. Taking into consideration the weak temperature dependence of the conduction current in the Ohmic region, we have assumed the tunnelling conduction mechanism. In the case of the thermionic mechanism, the conduction current would be strongly dependent on temperature, which is not observed.

The next comment is connected with the work function of the islands. We have assumed that the work function as well as the Fermi energy are the same in all the islands. However, this assumption can be not valid for very small islands where the effects of the Coulomb blockade can be essential. Generally, such effects should not be pronounced in the conductivity of two-dimensional ensembles of islands at room temperature. It is known (see e.g. [71]) that two major prerequisites must exist for the observation of the Coulomb blockade: (1) one should provide the condition $e^2/2C \gg kT$ (C is the capacitance of an island with respect to its environment); (2) the tunneling resistance of the gaps between the island and its neighbors ("contacts") must be larger than the resistance quantum $h/2e^2$ so that the electrons are well localized on the island. The first condition is fulfilled only for extremely small islands (with the radius $\lesssim 3$ nm at 300 K). The second condition demands a favorable arrangement of the islands. A further obstacle to observing effects of the Coulomb blockade in the conductivity of *two-dimensional* ensembles of islands is caused by the possibility for electrons to bypass the blocked islands and thus to find the paths of a lower resistance. This consideration is corroborated by the fact that the Coulomb blockade is observed rather easily in the *single* island chains [72].

3.3. Electron emission from IMFs under conduction current excitation: integral characteristics

Electron emission from IMFs is always observed in the non-Ohmic region of the conduction current–voltage characteristic. Typical dependences of the emission current on the voltage applied to the contact electrodes of the film and on the anode (extracting) voltage are depicted in Fig. 3.3. Such dependences have been used by many authors to consider the mechanism of the electron emission. Two alternative mechanisms have been discussed: field emission and emission of hot electrons. The former model [73,74] considers that, despite the low value of the voltage applied to the film, rather high electric fields can exist in the narrow gaps between the islands. The fields can have elevated values near the smallest islands and in the emission centers where the potential drop is found to be enhanced [73,75–78]. These fields can give rise to field emission currents flowing from one island to another (in other words, the conduction current should be field emission by its nature), and it may be imagined that a part of this current can be sucked off by the extracting electrode (anode). Qualitatively, this model may seem rather reasonable. In support of this interpretation its adherents argue that in a number of cases the dependences of the emission current, I_e, on the voltage applied to the film, U, appear linear when plotted in the Fowler–Nordheim ("field-emission") coordinates lg (I_e/U^2) versus $1/U$ (see e.g. Fig. 3.4). Notice that U is the voltage between the contact electrodes of the film and not the anode voltage U_a, which is kept constant in the experiment. (Incidentally, I_e as a function of U_a is nonexponential and exhibits a tendency to saturation at high values of U_a (Fig. 3.3).) It is therefore tacitly assumed that

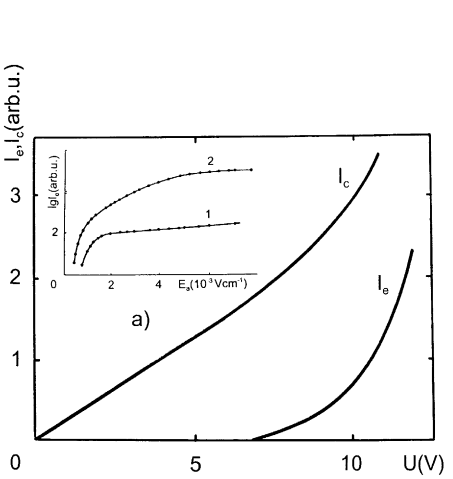

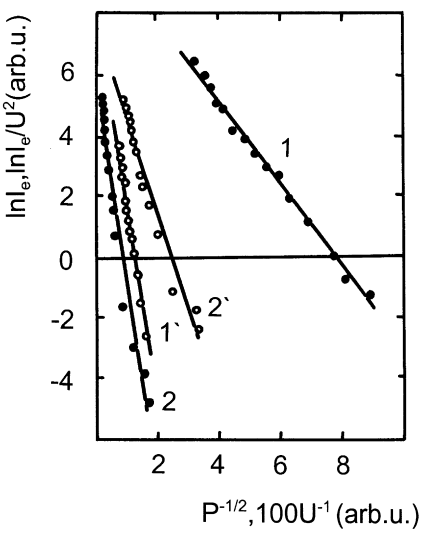

Fig. 3.3. Dependences of the conduction current I_c and electron emission current I_e on the voltage applied to an Au IMF. Inset: Dependences of electron emission current I_e on the average electric field applied between the IMF (cathode) and anode. The average electric fields within the film are respectively 10^3 V/cm for curve 1 and 4×10^3 V/cm for curve 2.

Fig. 3.4. Dependences of the electron emission current I_e on the power fed into film ($P = I_c U$) and the voltage applied across the film (U). In plots 1 and 2, the data for two different films are presented in the coordinates $\ln I_e$ versus $P^{-1/2}$. In plots 1′ and 2′, the same data are presented in the coordinates $\ln I_e/U^2$ versus $1/U$ (from Ref. [6]).

the part of the conduction current branched off to the anode remains constant as the current varies. It has to be admitted, however, that results similar to those depicted in Fig. 3.4 can hardly be considered as a convincing proof of the field emission model. The range of the voltages in which such dependences can be recorded is usually rather narrow, so it is not very surprising that a straight line can be fitted more or less satisfactorily to $\log I_e/U^2$ within this range. Further still, this model is in poor agreement with experimental data on the effect of adsorbed layers: as one covers an IMF with an overlayer reducing its work function, the conduction current increases several-fold (or by an order of magnitude at most) whereas the emission current grows by a few orders of magnitude (see Section 3.5 for more details). This finding is in evident contradiction with the expectations of the field emission model that the electron emission current should vary proportionally with the conduction current (or at least to its field-emission component). The results [75] about the high sensitivity of the electron emission current to the deformation of the film substrate ("the tensoeffect") are also poorly compatible with the field emission model [73] which suggests the emission from nanosized ($\lesssim 10^2$ nm) island "cathodes" to large islands serving as "anodes" and located at a distance of ~ 1 μm from the "cathodes". It is well known from the field emission experiments that in such a geometry the emission current should be weakly dependent on the cathode–anode spacing and therefore on the substrate deformation. There are also discrepancies of the data on the temperature dependence of the electron emission from IMFs [79] with predictions of the field emission model.

Let us turn now to the model of hot electrons. Recall that it also considers the tunneling of electrons between the islands, but, contrary to the field emission model, the sufficient transparency of the potential barriers is attributed just to small inter-island spacings rather than to the effect of the external electric field. This model predicts [70] (see also Section 3.2) that the emission current should be a linear function in the coordinates $\log I_e$ versus $1/(P)^{1/2}$, where P is the power pumped into the emission center. Some experimental results obtained in the case of the conduction current excitation of thin films are consistent with this prediction (Fig. 3.5) [6] while others are not [73,74]. (It is important to note that actually one plots the dependence of $\log I_e$ versus reciprocal square root of the total power fed into the film, which is believed to be proportional to the power fed into individual emission centers.)

Obviously, a vulnerable point of the above experimental arguments is that characteristics of the phenomena occurring in the emission centers, which are ≤ 1 μm in size and take just a minor part of the total film surface area, are correlated with integral values such as the voltage or the power applied to the whole film. It is therefore necessary to test both the models on a larger set of experimental data including the electron energy distributions, the electron emission stimulated by infra-red irradiation and the light emission from IMFs. This will be done in the following sections.

3.4. Electron emission from a single emitting center

For typical geometries of IMFs, the electroforming procedure usually results in emergence of many emission centers. It is clear that examination of a single center is much more informative from the physical standpoint than analysis of integral characteristics which contain contributions from a set of the centers. (In addition, their number can change if the voltage is varied within a broad range.) The investigation of individual centers is especially important when it is necessary to analyze the electron energy distribution. If the integral retarding field characteristics of the

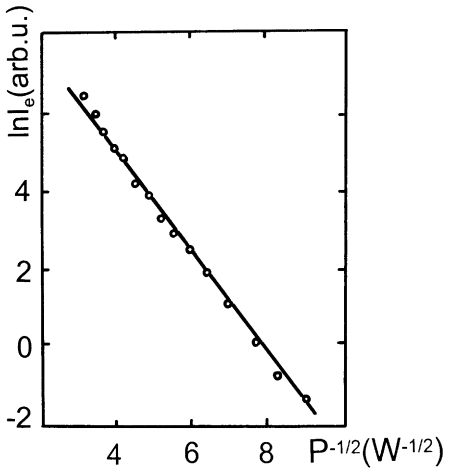

Fig. 3.5. Dependence of the electron emission current I_e from an Au island film on $P^{-1/2}$, where $P = I_c U$ is the power fed into the film [6].

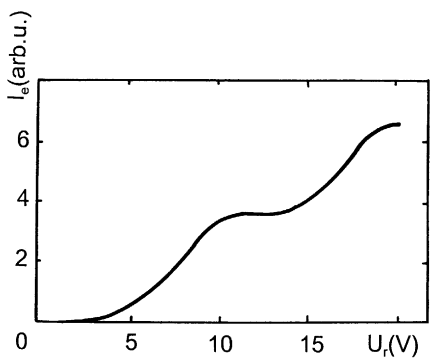

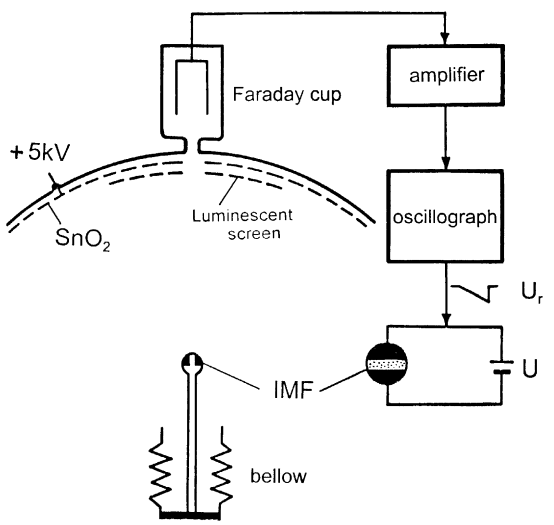

Fig. 3.6. Retarding-field curve of electron emission current in a device with plane-parallel geometry.

Fig. 3.7. Schematic of a device for recording the retarding-field curves of electron emission from a single emitting center.

emission current are measured in a device of the flat capacitor type, one usually records curves with two saturation terraces (Fig. 3.6). This indicates that the current comes from two groups of emission centers located in different areas of the film (typically near the contacts) having different potentials. In the case when the centers are grouped near one of the contacts only, the retarding field curves have an ordinary shape with one saturation level. To obtain such a curve for an

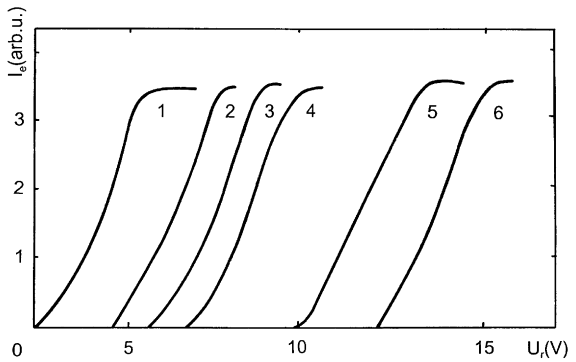

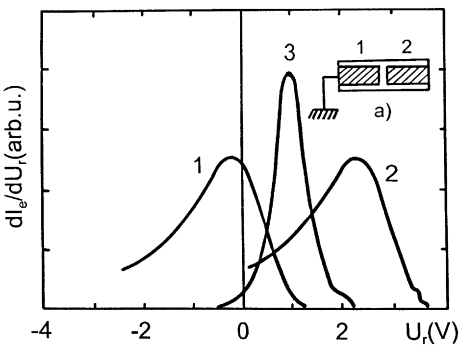

Fig. 3.8. Retarding-field curves of electron emission current from a single emitting center at various voltages applied to the film: 1–10 V; 2–15 V; 3–17.5 V; 4–20 V; 5–24 V; 6–30 V.

Fig. 3.9. Energy spectra of secondary electrons emitted from the contact electrodes (1,2) and of electrons emitted from a center in an Au film (3). The energy of the bombarding electrons is 25 keV and the voltage applied to the film is 2.5 V [82]. Inset: schematic of the sample under study (1 and 2 are contact electrodes).

individual center, a device of spherical geometry ("a spherical capacitor") was used which allowed the electrons emitted from a selected center to be directed into the energy analyzer (Fig. 3.7) [43,80]. The device represented a spherical glass bulb 150 mm in diameter whose inner wall was coated with a transparent conducting layer and a cathodoluminescent screen. The bulb had a probe hole in the screen and a retarding field analyzer placed behind it. The film studied was deposited onto a glass sphere 2 mm in diameter located at the end of a glass rod which could be moved with a manipulator. Fig. 3.8 depicts examples of the retarding field curves recorded for an emission center at various voltages applied to the film. The width of the steep ("retarding field") section of the curve, ΔV, is determined by the spread in electron energies, the potential drop within the center and the resolution of the analyzer. ΔV was found to be only weakly dependent on the voltage applied to the film which means that only a small part of this voltage drops across the center. Anyway, the retarding field curves showed that the sum of the electron energy spread and the voltage drop within the center does not exceed ~ 3 V. The minimum value of ΔV recorded experimentally was ~ 1 V.

The electron energy distribution was also studied in a scanning electron microscope equipped with a retarding field analyzer having an immersion objective [81,82]. The experiments were carried out with gold IMFs which were prepared within a 20 μm gap between two gold contact electrodes. The secondary electron emission from the contacts was used for calibration of the energy scale of the analyzer. To minimize the effect of electric microfields existing over the islands [76] on the energy spectra recorded, the measurements were made at voltages on the film equal to 2–3.5 V (the emission current was at the level $\sim 10^{-12}$ A). Fig. 3.9 shows the energy distributions for electrons originating from an emission center and for secondary electrons emitted from the contacts. The position of the energy spectrum of electrons between the curves corresponding to the secondary emission from the contacts is determined by the potential drop across the film. The high energy wing of the energy distribution was found to be Maxwellian, and the electron gas

temperature within the emission center was estimated at $T_e \sim 3400\,K$ [82]. This value agrees by order of magnitude with the electron temperatures evaluated by other methods [83–85].

3.5. *Effect of overlayers on the conductivity and electron emission from IMFs*

Let us start with electropositive overlayers. The evaporation of BaO on island films leads to a significant increase of the conduction current (Fig. 3.10, curves 2–4) and to a drastic, by several orders of magnitude, growth of the emission current (Fig. 3.10, curves 2′–4′). Both the effects can be ascribed to the reduction of the work function. The variation of the work function was monitored by recording the shift of the red boundary of photoemission from a continuous Au film deposited adjacent to the island film and exposed to the same BaO molecular beam.

The model of nonequilibrium heating of electrons in small particles (Sections 3.2, 5 and 6) interprets the observed electron emission from IMFs as the Richardson emission of the hot electrons. With this assumption we used the work function dependence of the emission current to estimate the electron temperature T_e and obtained its value at $\approx 2000\,K$. Contrary to this, the lattice temperature of the islands remains much lower which ensures the long-term operation of such IMF cathodes.

If the BaO coating over an IMF is only about one monolayer thick, the emission current, which is initially very strongly enhanced, decreases with time to a new steady-state level which still remains much higher than in the absence of the BaO layer. The current can be increased again by repeated evaporation of BaO. The measurements of the emission current–voltage curves for individual emission centers performed in a quasi-spherical energy analyzer have shown that the decay of the emission current is caused by some work function increase [86]. Probably, this can be associated with the field induced drift of BaO molecules out of the emitting center. It should be recalled that in the case of a polar adsorption bond, the direction of the field drift is dependent on the mutual orientation of the electric field and the dipole moment [87,88]. To ensure a long-term effective electron emission, with an emission-to-conduction current ratio of ≈ 10–15%, it is necessary to provide a continuous supply of BaO to the emitting center. This effect can be achieved by deposition of island films onto a substrate previously coated with a thick BaO layer (see Section 8).

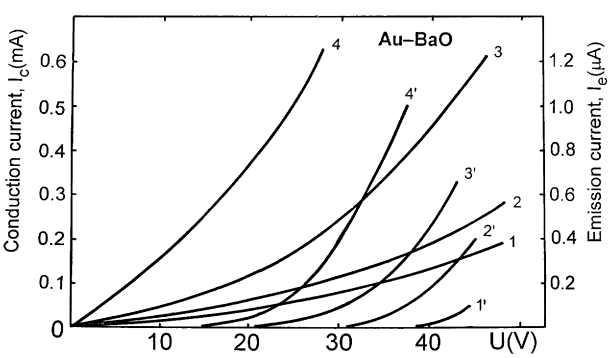

Fig. 3.10. Current–voltage curves for conduction current (1–4) and emission current (1′–4′). Curves 1 and 1′: clean Au film; curves 2–4 and 2′–4′: Au film with various BaO overlayers.

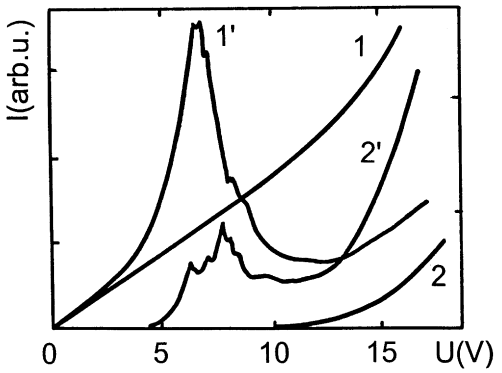

Fig. 3.11. Current–voltage curves of conduction current (1) and electron emission (2) for an Au island film. (1′) and (2′) are the same characteristics after deposition of organic molecules.

A similar effect of BaO as well as Ba overlayers on the electron emission was also found for graphite island films. These films were excited both by the conduction current and by pulsed CO_2 laser irradiation ($\lambda = 10.6\,\mu m$, $\tau = 200\,\mu s$) (Section 3.7).

Adsorption of BaO molecules represents a comparatively simple example of the effect of overlayers on properties of IMFs. There are, however, more complicated cases. Early experiments with IMFs detected that quite often the conductivity current becomes unstable when the film is kept in vacuum obtained using oil diffusion pumps [89,90]. In particular, under certain conditions the conduction current–voltage characteristics were found to become nonmonotonic (N-shaped), i.e. to reveal a voltage-controlled negative resistance (VCNR). An example of such characteristics is given in Fig. 3.11. It is known that in MIM (metal–insulator–metal) structures, the VCNR and switching from low-resistanse to high-resistance state and vice versa are frequently observed effects (see e.g. [91–93]). Obviously, the systems considered (IMFs and MIM structures) bear some similarity to each other. This similarity becomes even more far-reaching if one considers that electroforming of the MIM structures can produce current channels which contain small metal particles arising due to the partial destruction of one of the electrodes [94,95]. A detailed review of the VCNR and switching effects in the island films (planar MIM diodes) and in sandwich MIM diodes was given by Pagnia and Sotnik [8], so we shall discuss here only the points which received less attention in [8] as well as some results of later works.

Major experimental findings regarding VCNR in island metal films can be summarized as follows.

1. VCNR effects have not been found for the island films prepared in ultrahigh vacuum on well outgassed substrates. A prerequisite to the observation of such effects is the presence of specific kinds of adsorbates on the film surface, in particular of some organic compounds or of water containing their traces [96]. There are data suggesting that at least in some cases it is just the hydrated molecules of these compounds that may cause the occurrence of VCNR [41]. It is also important to add that, in order to prepare an island film exhibiting VCNR, it is necessary to apply an appropriate voltage to the film either during or immediately after the deposition of the overlayer, i.e. to “polarize” it.

2. Electron microscopic investigations performed with a resolution of 2–3 nm did not reveal any structure changes in the film during its transition from low-resistance to high-resistance state or in the opposite direction [41]. The film structure starts to show visible changes only when the applied voltage exceeds several-fold its value corresponding to the current maximum in the current–voltage curve. However, in this case the film is irreversibly destroyed.

3. Scanning electron microscopy was used to visualize the potential distribution within the films displaying VCNR behaviour [77]. The distribution was found to be uniform in the low-resistance state, i.e. in the voltage range preceding the negative differential resistance. In the high-resistance state, potential jumps localized within the regions of ≤ 0.1–$1.0\,\mu m$ were observed. Later STM investigations [78] confirmed the existence of the potential jumps and showed that regions of their localization are even narrower.

4. In the low-resistance state of the films with VCNR, the temperature resistance coefficient in the interval 20–300 K is positive and close to its values typical of metals. This coefficient becomes negative in the high-resistance state and its value is characteristic of the clean IMFs [97].

5. The VCNR behaviour disappears if the film coated with the overlayer is annealed at 500–600 K. However, this behaviour is restored after repeated adsorption.

6. The return trace of the *I-U*-hysteresis loop (Fig. 3.12), segment BA' is sluggish. If this trace is passed fast (in a time < 0.1 s), the current changes along the path BCO, and the high-resistance state can keep indefinitely long (a "field memory"). To restore the low-resistance state, it is sufficient to increase the voltage by 0.1–0.2 V with respect to point *C*. Then the further change of the current proceeds along path ODA.

7. The shape of the *I-U*-curve depends on the number of the current channels in the film (equal to the number of the emission centers – see Section 2.4) and on the spread in their properties. If these properties are sufficiently uniform or if only one current channel is present, the transition from the high- to low-resistance state becomes extremely sharp indicative of a switching process [72].

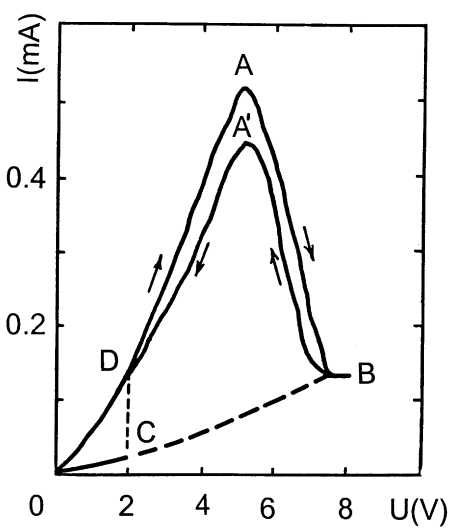

Fig. 3.12. Conduction current–voltage curves for an Au island film covered with a naphthalene layer. ODA: low-resistance state. BCO: high-resistance state. OC: region of field memory.

8. If in the low-resistance state the temperature of the film is lowered to $< 100\,K$, the negative resistance segment is observed only once and further changes of the current proceed along path OCB (Fig. 3.12). The VCNR behaviour is restored as temperature is raised above 100 K. Therefore such films possess a "temperature memory".

9. The shape of the *I-U*-curve and the height of the maximum are sensitive to the pressure of residual gases [8]. If an IMF kept in the low-resistance state is coated with a thin dielectric layer, the VCNR segment OAB can be passed only once. The dielectric layer irreversibly prevents the restoration of the low-resistance state and the return trace proceeds along BO (Fig. 3.12). These results demonstrate that the VCNR behaviour is determined by surface electronic processes and not by processes in the substrate as was supposed in early studies [57,98].

10. The position of the maximum in the current–voltage curve shifts to lower voltages when a pulsed instead of a constant voltage is applied.

11. In the VCNR region, one observes electron and light emission from the film.

Here we shall exemplify the above regularities with data obtained recently for gold IMFs coated with stearone overlayers [69]. Stearone $[(C_{17}H_{35})_2CO]$ was evaporated onto island films with previously formed current channels and emission centers. The evaporation was performed while a voltage of ≈ 10–$15\,V$ was applied to the film. Stearone molecules adsorbed under such conditions induce an enhancement of the conduction current, and, what is more important, a VCNR section appears in the conduction current–voltage curves at voltages 4–6 V (Fig. 3.13a, curve I_c). Simultaneously the characteristics of electron and light emission are also changed (Fig. 3.13, curves I_e and I_L). Quite analogous effects were observed with naphthalene $(C_{10}H_8)$ overlayers evaporated on the island films [99].

As noted above, organic admolecules increase the conduction current and bring about the VCNR behaviour only upon holding the film under a voltage of 10–15 V either in the course of evaporation of the organics or after it. (By contrast, BaO enhances the conduction current without such procedure). It has been suggested that organic species are polarized in the high electric field existing near the islands (estimated at 10^5–10^6 V/cm) and pulled into the emission centers where

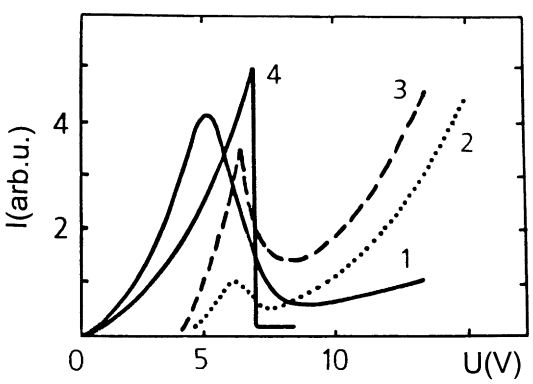

Fig. 3.13. Current–voltage curves of conduction current I_c (1), electron emission current I_e (2) and light emission intensity I_L (3) for an Au island film covered with a stearon layer. Curve 4 shows a conduction current–voltage curve I_c versus U for a chain island film covered with an organic adsorbate. Units at the ordinate axis are different for all curves.

they self-assemble into thin quasi-polymeric filaments spanning the gaps between the islands [45]. It should be recalled that the formation of molecular waveguides for electrons was observed a few decades ago in experiments with organic molecules adsorbed on metal tips in the field emission microscope [100,101]. The average diameter of the polymeric filaments, oriented along the field lines, was estimated at several nm [102], i.e. the same as the size of nano-islands. If similar organic bridges are formed in IMFs, the current density in them should be at least $\sim 10^5\,\mathrm{A/cm^2}$. Probably, such a high current density could be passed without destroying the filaments because of the very efficient withdrawal of the Joule heat to the substrate. However, at higher current densities the conducting filaments can be melted or even evaporated which may cause a decrease in the conduction with increasing voltage. When the voltage is reduced, the temperature decreases and organic conducting bridges can be restored (replenished) by migration of the adsorbate from adjacent areas to the emission centers. This "desorption/diffusion" model might, in principle, explain qualitatively both the occurrence of the N-shaped $I_c - U$ curve and its repeated reproduction ($> 10^4$ times) while cycling the voltage [39].

However, the data on the light emission from island films covered with organics (typical for electroluminescence in semiconductor structures – see Section 4) impel consideration of an alternative model. We suppose that organic admolecules arrange themselves into semiconducting bridges (which may be poorly ordered) between the islands. As a consequence, the VCNR region in the conduction current–voltage characteristics can arise through one of the mechanisms suggested for switching phenomena in semiconductors: thermal (structural), electronic or combinations of these. This interesting topic goes beyond the scope of our paper and we refer the reader to a recent review focused on switching in semiconductor thin films [103].

It should be noted that the slope of the VCNR section is an integral characteristic of the whole film which contains many current channels with distinct properties. Therefore, the peculiarities seen in the VCNR region (see small steps and terraces in curves shown in Fig. 4.6, Section 4) may originate from contributions of different channels. In the cases when the current channels have rather close parameters, e.g. in the chain island films, the VCNR section appears very steep so that one actually observes a switching regime [39,72].

A few works have been devoted to electron emission from the island films showing VCNR behaviour [72,79,96,104,105]. For example, Blessing and Pagnia [104] utilized a photoemission microscope with a spatial resolution of 100 nm and a Moelenstedt energy analyzer with an energy resolution of 0.5 eV (at acceleration voltage 20 kV) to study spatial and energy distribution of electrons emitted from Au IMFs. According to their interpretation, electron emission in the VCNR region is provided by hot electrons (perhaps with some contribution from microplasmas), while at higher voltages they argued for the field emission mechanism (see Section 3.3 for a discussion of this model). In later works of this group [105–108], a model of carbon islands has been suggested. They can arise in an oil-pumped vacuum due to cracking of residual hydrocarbons and subsequent graphitization. Owing to injection of fast electrons through tunneling junctions, the electron temperature in the carbon islands can be elevated up to $\sim 4000\,\mathrm{K}$ (as estimated from photon emission spectra [106]) which results in thermionic emission of hot electrons. (See also work [79] on the emission properties of carbon island films.) The carbon islands can be destroyed at high temperatures by residual oxygen and again be built up at lower temperatures. However, in the context of the experimental results listed above and obtained for various "coated" island films showing VCNR, the model of carbon bridges (islands or filaments) seems to be appropriate only in

some particular cases. The general conclusion is that it cannot be accepted as a universal explanation of the VCNR behaviour of the island films.

The results presented in this section show that deposition of various overlayers on nanodispersed thin films allows a wide-range modification of their properties. In particular, using this approach one can obtain planar composite structures whose characteristics combine the peculiar properties of nanoparticles and of the substance filling the gaps between them.

3.6. Electron emission from silicon island films

In this section, we present some data which demonstrate that in semiconductor island films phenomena can occur analogous to those observed in the case of metal films. If the model of hot electrons which is discussed in this review in application to metals is true, electron and light emission from small semiconductor particles caused by pumping energy into them should also be expected. Indeed, nonequilibrium heating of electrons in semiconductors (contrary to bulk metals) is a common phenomenon [109,110].

The experiments have been performed with Si. To obtain a Si island film, we first deposited epitaxially a continuous single-crystal n-Si film (100 nm thick, 10 Ω cm) on a sapphire substrate. The continuous film had in the middle a section 50 μm wide where its thickness was 50 nm. The contacts were evaporated on the thicker parts of the film. The film was first outgassed at $\sim 10^{-8}$ Torr and then a sufficiently strong current was passed through it which led to the formation of a Si island film in the thinner part of the sample. For comparison, some experiments were made with a porous Si sample prepared by electrochemical etching.

The conduction current $I - U$ curves for clean silicon island films are quite similar to those recorded for metal island films (Fig. 3.14), but neither electron nor light emission is observed until the work function of Si islands is reduced by some appropriate overlayer (e.g. BaO). Thus, the hot electrons which can be generated in Si islands cannot pass into vacuum if the Si surface is clean. This result resembles the experiments carried out in an attempt to obtain electron emission from Si p–n-junctions cleaved in high vacuum [111]. In that case, no emission was observed, too, which was attributed to the unfavorable relation between the impact ionization energy (2.25 eV) and the electron affinity (3.6 eV) in Si. Due to the low impact ionization energy, the electrons cannot be

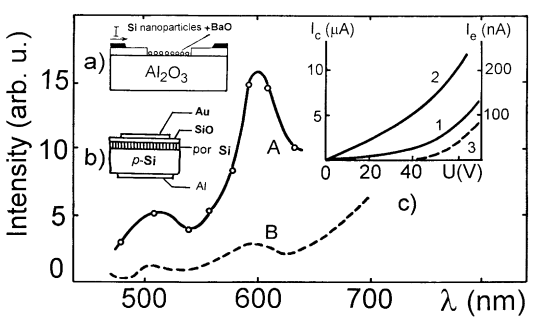

Fig. 3.14. (a) Structure with the island Si film; (b) structure for observation of electroluminescence of porous silicon; (c) $I - U$ curves for conduction current of clean silicon island film (1), BaO/Si island film (2) and for emission current from BaO/Si island film (3). (A) and (B) are light emission spectra for structures a and b.

heated enough to overcome the surface barrier. However, the emission emerged upon reducing the Si work function by a few eVs.

In the case of Si island films, the evaporation of a BaO overlayer lowering the work function by 2.2–2.5 eV resulted in a substantial enhancement of the conduction current and in the appearance of electron and light emission (Fig. 3.14; curve 3).

We have compared these results with data on electroluminescence and electron emission from a porous Si sample prepared by electrochemical etching of p-Si (0.01 Ω cm) plates. The size of the pores and the thickness of the walls between them was 5–10 nm. A sandwich test structure was used (Fig. 3.14b). The electroluminescence and electron emission were observed for as-prepared samples (no activating coating was needed). The spectrum of the electroluminescence of the porous Si is rather similar to that recorded for the Si island film covered with BaO (Fig. 3.14; curves A, B). It was found, however, that the electroluminescence, photoluminescence and the electron emission disappear after outgassing the porous Si sample. They could be restored after H_2O adsorption [112–114], which demonstrates that surface conditions strongly affect the behavior of porous Si. It should be recalled that there is a number of reports on electron emission from porous Si (see e.g. [115,116]). The photon emission from porous Si has also been recorded in the STM [117].

3.7. Electron emission from IMFs under infra-red laser excitation

As noted in Section 3.2, the physical interpretation of emission experiments with the island films excited by passing current cannot be accepted as conclusive. It was therefore desirable to obtain additional data on this phenomenon, in particular, to examine the electron emission from the films subjected to an alternative (currentless) excitation. Such an excitation has been effected by infra-red laser irradiation [2–4]. In Section 7, we give detailed physical arguments that using a sufficiently powerful IR laser one can very efficiently pump energy into small metal particles having a special shape.

A pulsed CO_2 TEA-laser ($\lambda = 10.6\,\mu m$, $\tau = 0.2$–$1.0\,\mu s$, $f = 1$–$30\,Hz$) was used to irradiate Au, Cu and graphite island films on Si [4,118]. The laser beam intensity was measured with a pyroelectric detector. Neutral filters were utilized to attenuate the beam irradiating the film. In the experiment, the same area of the film was exposed to the beam whose intensity was progressively increased. The structure of the film was investigated at different stages of the exposure in an electron microscope. The electron and photon emission set in as the power density P reaches a value of about $10^4\,W/cm^2$. It is known that in the case of bulk metals similar effects appear at $P > 10^7\,W/cm^2$ and are ascribed to various mechanisms (thermionic and field emission, many-photon photoeffect) [119,120]. Within the range of 10^4–$10^5\,W/cm^2$, the emission current from the island films is stable and the shape of the emission pulses reproduces quite closely that of the laser pulses. The delay time of the emission is estimated at $< 2 \times 10^{-8}\,s$. The work functions of the materials under study (≈ 4.5–$5.0\,eV$) are by a factor of ~ 40 higher than the quantum energy $h\nu = 0.12\,eV$ at $\lambda = 10.6\,\mu m$. Thus, the photoemission, both one-photon and many-photon, can be excluded as a possible emission mechanism. The field emission seems also improbable due to low electric fields ($\sim 10^4\,V/cm$) in the laser beams used. Taking into account the above work functions and the saturation vapour pressures of the materials, one is led to the conclusion that the thermionic mechanism, too, cannot ensure the observed stable current densities of $\sim 10^{-2}\,A/cm^2$, at least for Au and Cu films. The thermionic emission does come into effect, but at much higher power

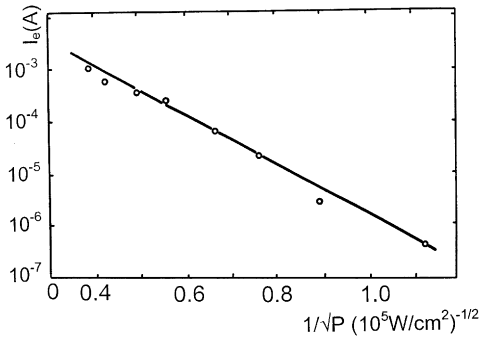

Fig. 3.15. Logarithm of the electron emission current from a carbon island film on Si excited by a CO_2 laser as a function of $P^{-1/2}$.

densities ($\sim 5\times10^5$ W/cm^2) at which the emission pulses become significantly lengthened and the islands are quickly destroyed thereby causing the emission to decay.

Fig. 3.15 shows the emission current as a function of the power density in the laser beam [121]. When plotted as log I_e versus $P^{-1/2}$, this dependence is seen to be linear in agreement with the theory [122] (see Section 3.3). We recall that such a behaviour of the emission current follows from the calculations which predict that, at large power densities fed into an island and independent of the mechanism of excitation, the electron temperature should be proportional to $P^{1/2}$. In other words, one obtains a Richardson dependence of emission current on the hot electron temperature. (The lattice temperature is much lower – see Section 5.)

Energy distributions of electrons emitted from IMFs under IR laser irradiation were investigated in work [123]. The gold IMFs were prepared on a Si wafer coated with a thin layer of silicon nitride. The sample was placed into a scanning electron microscope and the same energy analyzer was employed which had been used earlier to measure the energy spectra of electrons emitted from IMFs under current excitation (Section 3.4). The half-width of the energy distribution of electrons in the case of laser excitation was found to be ≈ 0.6 eV. This value was considerably larger than the estimated instrumental width and therefore corresponded, roughly speaking, to an electron temperature of $\sim 10^3$ K. However, the distribution was non-Maxwellian. Discussing the data in terms of the model of hot electrons, the authors [123] supposed that the non-Maxwellian character of the distribution may be caused by the fact that the measured emission current contains contributions from many islands which have different electron temperatures.

Thus the whole set of data suggests that the electron emission observed at moderate irradiation intensities is most probably due to nonequilibrium heating of electrons in metal islands. This model is also corroborated by the following findings: (1) the energy spectra of the emitted electrons reveal the existence of electrons with energies up to ≈ 3 eV (at $P = 5\times10^5$ W/cm^2); (2) the spectra of the concomitant light emission, if they were roughly ascribed to the equilibrium radiation from the islands, would correspond to $T \approx 1000$ K which is too low to provide any appreciable thermionic (equilibrium) emission. Strictly speaking, however, the light emission spectra of the island films do not at all obey Planck's law and show instead two or three more or less pronounced maxima [124,125] (see also Section 4). A detailed theoretical analysis has revealed that the light emission

may be caused by (i) bremsstrahlung, (ii) the inverse of surface photoelectron emission, (iii) inelastic tunneling of electrons and (iv) radiative decay of surface plasmons [126].

From the practical viewpoint, the electron emission from the island films is quite stable at moderate power densities (up to 10^5 W/cm^2 for Au and 10^6 W/cm^2 for graphite films). Thus such films can be utilized as photocathodes to visualize the intensity distribution in IR laser beams (see Section 8).

4. Light emission from island metal films

4.1. Light emission from clean IMFs

Here we shall first consider the light emission from IMFs which occurs under conduction current excitation. We recall that both electrons and light are emitted from the same centers which has been demonstrated in experiments comparing the relative position of the luminous spots on the film with the pattern produced by emitted electrons on a screen (see Section 3). This statement has been convincingly corroborated by measurements which have detected the existence of almost full correlation between the low-frequency fluctuations of the electron emission current and light intensity [127] (Fig. 4.1). The light emission as well as the electron emission starts at the voltages where a deviation from Ohm's law becomes apparent (Fig. 4.2). The light emission appears without perceptible time lag on applying voltage to an electroformed film. The emitting centers are readily visible and may be coloured differently within the same film. Fig. 4.3 shows typical spectra of light recorded from two simultaneously emitting centers in an Au island film (curves 1 and 2) [127]. It is seen that the spectra are rather broad and sometimes consist of distinct bands. A similar shape of the spectra has been found for silver island films (Fig. 4.4). The existence of several intensity maxima may suggest that a few light emission mechanisms are operating in parallel. Theoretically, one can predict that the light emitted by IMFs contains contributions from intraband quantum transitions, bremsstrahlung, inverse surface photoeffect and plasmon-mediated radiation (the plasmons being generated both in inelastic tunneling and by hot electrons). We shall address this question in more detail in Sections 5 and 7. For a chain island film (Fig. 4.3, curve 3), the light emission spectrum is considerably narrower.

Now, let us compare the above data with light emission spectra measured for other related systems. In particular, one can readily see an obvious similarity between a pair of adjacent metal islands on a dielectric substrate and a metal–insulator–metal (MIM) structure as well as a tunnel gap in STM. The difference is that the island structure is more open than the MIM structure, and two islands are separated from each other both by a gap on the insulator surface and by a vacuum gap. Therefore, the comparison of the characteristics of the objects listed above may be meaningful. The light emission from MIM tunnel junctions has been investigated in many works (see e.g. [67,128–135]). The spectra obtained have been attributed mainly to the radiative decay of surface plasmon-polariton modes excited by inelastic electron tunneling. There are also experimental arguments in favor of the radiative decay of surface plasmons that are generated by hot electrons injected into one of the metal electrodes without energy loss in the tunneling gap [132].

In Fig. 4.3 we compare spectra of the light emission from an Au IMF (curves 1 and 2) with the spectra recorded by Berndt et al. from a tunnel gap between an Au (110) surface and W tip in

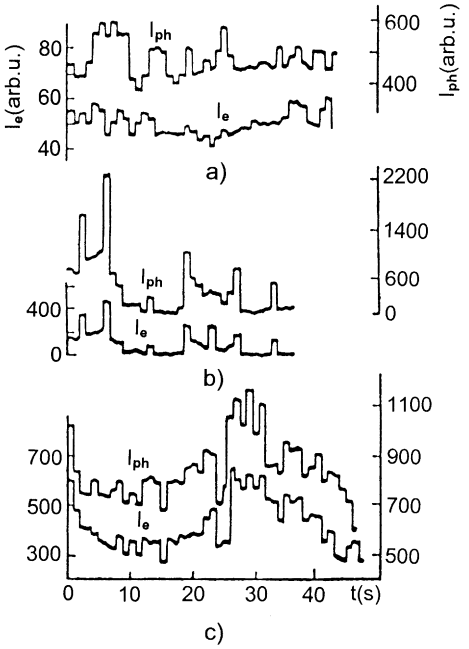

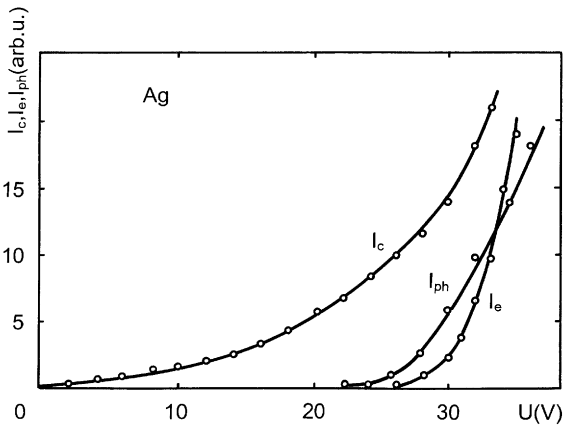

Fig. 4.1. Time fluctuations of the electron emission current (I_e) and of integral light intensity (I_{ph}) recorded at various values of power fed into a gold island film: (a) 0.02 W; (b) 0.04 W; (c) 0.2 W [6,127].

Fig. 4.2. The current–voltage curves of the conduction current (I_c), electron emission current (I_e) and light intensity (I_{ph}) on the voltage applied to the film.

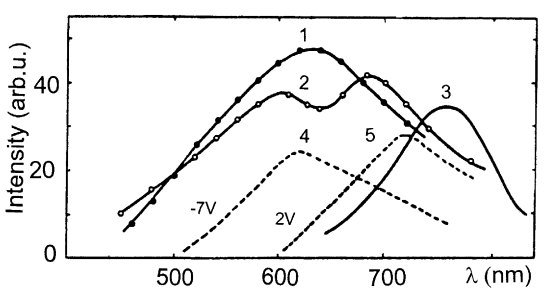

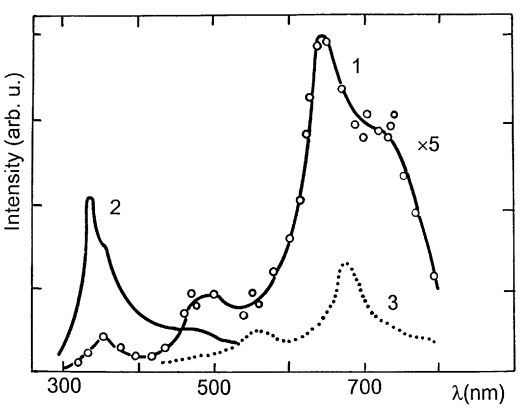

Fig. 4.3. Light emission spectra: (1) and (2) for two emitting centers in the same Au film; (3) for a chain Au island film; (4) and (5) for an Au/W tunnel gap in STM [136,137].

Fig. 4.4. Light emission spectra: (1) for an individual emitting center in a silver IMF excited by conduction current; (2) for the same film excited by electron bombardment (50–200 eV); (3) for a Ag-tip/Ag(111) tunnel gap [138].

a scanning tunneling microscope (curves 4 and 5) [136,137]. The STM spectra were taken at various tip bias voltages, and one can see some resemblance between them and the IMF spectra, although the latter are more complex in shape. A spectrum for an Ag IMF having a single light emitting center is juxtaposed in Fig. 4.4 with a spectrum of an Ag-Ag(111) tunnel gap in a STM [138]. This comparison is of special interest, because the STM data relate to the case when both the tip and the sample were made of the same material (Ag). A rather close similarity in some features of the spectra is evident. The photon emission spectra recorded in a STM are interpreted in terms of radiative decay of tip-induced plasmon modes excited in inelastic electron tunneling [136–147]. There are good reasons to believe that similar localized plasmons can form and decay in the tunnel gap between the adjacent nano-islands. However, the spectrum for the IMF has a few peaks (with wave lengths corresponding to photon energies 3.5, 2.5 and 1.9 eV). In particular, the ultraviolet peak ($\lambda \approx 350$ nm, $h\nu = 3.5$ eV) coincides with the maximum in the photon radiation observed under electron bombardment of the Ag island film from an external electron source. Thus, we hold to the view that several maxima seen in the photon spectra of IMFs may indicate the operation of diverse physical mechanisms of light emission from these films. This possibility can originate from the generation of hot electrons which are able to induce electromagnetic radiation due to various effects (see Section 5). As mentioned above, the spectra of the emitting centers in the chain island films are usually considerably narrower and exhibit only one maximum [69] (Fig. 4.3, curve 3). This behaviour seems to reflect the fact that conditions of electron and light emission in the chain films are more uniform than in the "irregular" films.

The light emission spectra were also investigated for IMFs prepared of Ag, Cu, Mo, Bi, Pd and some other metals. The films were excited both by conduction current [6,148] and by low-energy electron bombardment ("cathodoluminescence regime") (Fig. 4.4) [6,149–151]. Recently, such measurements for Ag IMFs were carried out in a wider frequency range using a more sensitive CCD detector system [152–154]. The Ag island films were prepared by vacuum evaporation and by a gas aggregation method [155]. It was found that the light emission spectra are independent of the manner of preparation of IMFs and the total intensity of radiation is growing with increasing voltage applied to the film U. The most pronounced intensity maxima are located in the red region ($\lambda \approx 600$–730 nm). It is important to note that the light emission in this region ($h\nu \approx 1.7 - 2.1$ eV) occurs even in the case when the voltage is as low as 1 eV. This result is readily explicable in the framework of the model of hot electrons (see Sections 3, 5 and 6). Starting from $U = 12$ eV, new features (in addition to the intensity maxima in the range 600–730 nm) appear in the ranges 300–460 and 900–950 nm. In particular, the peak emerging at $\lambda \approx 320$ nm ($h\nu \approx 3.9$ eV) corresponds to the energy of plasma oscillations. It is supposed [152,153] that the number of the hot electrons with energies sufficient to excite the plasmons, which generate photons in their radiative decay, may be too small at $U < 12$ eV. The absolute and relative intensities of the high energy radiation maxima increase with increasing U. The features observed in the near infra-red region are more intense than that recorded at $\lambda \approx 320$ nm and are ascribed to the processes of inelastic tunneling and reflection of hot electrons.

The dependence of the light emission spectra on the size of the Pd particles bombarded by electrons at $E = 10^2$–10^3 eV was recently investigated in [150]. The average size of Pd particles was varied in the range 0.5–7 nm. The spectra were recorded in the range $h\nu = 1.2$–6.2 eV, so the possible light emission stemming from the radiative decay of plasmons ($h\nu = 7.3$ eV for Pd) could not be detected in these experiments.

4.2. Effect of overlayers on light emission from IMFs

The BaO deposition within the limits of a monolayer affects (increases) mainly the intensity of the emitted light while its spectrum remains almost unchanged. However, as noted in Section 8.1, the long-term functioning of IMF cathodes can be achieved by their fabrication on substrates previously coated by a thick BaO layer. In such a case, especially when large emission currents are extracted, one observes significant changes in the spectrum of the emitted light due to electroluminescence of BaO itself.

In experiments with stearone overlayers (see Section 3.5), the enhancement of the conduction and electron emission currents and formation of N-shaped conduction current–voltage curves were accompanied by substantial changes in the characteristics of light emission (Fig. 4.5, curve I_L in the inset). There is a considerable difference between the light spectra corresponding to the rising and falling (VCNR) segments of the conduction current–voltage curves. In the former case the spectrum is nearly structureless, but shows a steep intensity growth in the red and infrared region ($\lambda > 600$ nm). In the latter case there are two broad maxima at $\lambda \approx 510$ and 610 nm, and the intensity strongly increases at $\lambda > 700$ nm [156]. Both the spectra are distinct from the spectrum for clean gold island films (Fig. 4.3) which shows a number of pronounced maxima in the visible region. As noted in Section 3.5, there are arguments suggesting that organic molecules evaporated in vacuum onto IMFs can self-assemble into thin quasi-polymeric bridges spanning the gaps between the islands. Fig. 4.6 displays a close correlation between variations in the conduction

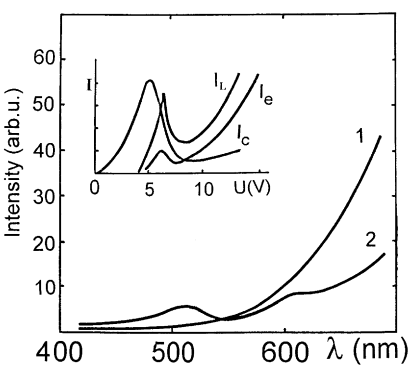

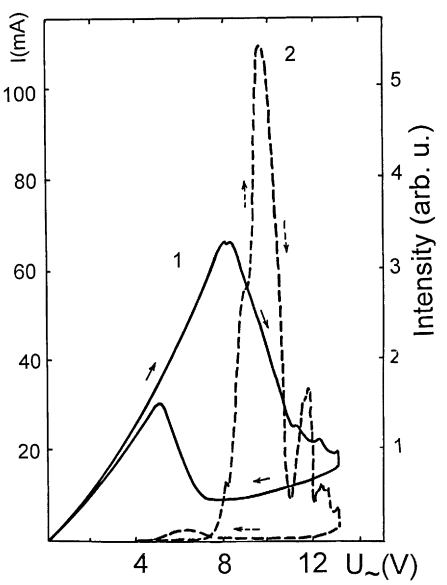

Fig. 4.5. Inset: conduction current I_c, emission current I_e and light intensity I_L versus AC voltage applied to an Au island film covered with stearone. Scales for I_c, I_e and I_L are different. (1) and (2) are light emission spectra in rising and falling section of the $I_c - U$ curve, respectively.

Fig. 4.6. Hysteresis loops for the conduction current (1) and light intensity at $\lambda = 615$ nm (2) recorded for an Au film covered with stearone. Voltage frequency: 500 Hz. Sweep time: 2 min.

current and light intensity ($\lambda = 615\,\text{nm}$). These results recorded in the alternating voltage regime show that the hysteresis loop for the light intensity mirrors rather closely the modulus of the derivative of the conduction current loop. Such a behaviour is quite typical for electroluminescence of semiconductors (see e.g. Refs. [157–159]). Thus we suppose that what is observed in our case may be the electroluminescence of organic bridges which are excited by hot electrons injected into them from adjacent metal islands.

The results presented in this section demonstrate the close correlation between the intensities of the electron and light emission from IMFs and thus evidence that a unified explanation should exist for both phenomena. Taking into account the nonequilibrium heating of the electron gas it is possible to explain the major origins of the electron and light emission from the island films.

5. Hot electrons in metal nanoparticles

5.1. Introductory remarks

Sections 5–7 are devoted to theoretical treatment of electronic kinetics and optical absorption in small metal particles and their ensembles. The peculiarities of these characteristics are caused both by the specific properties of individual particles and by interaction between the particles. The condition of the onset of a size effect is the comparability of the particle size to a physical value with the dimension of length (the de Broglie wavelength, the electron mean free path, the depth of the skin layer, the length of an electromagnetic wave, etc.). In what follows, we will show in detail that in the case when the particle size becomes smaller than the electron mean free path, the intensity of the electron–lattice energy exchange is strongly suppressed in comparison with its bulk value. Furthermore, in this situation the absorption of light by free electrons is determined by their scattering at the surface rather than in the volume. The optical properties of small particles as well as of their ensembles are also different depending on whether the particle size is smaller or larger than the length of the electromagnetic wave and the depth of the skin layer.

In the island metal films, additional features appear due to interaction between the metal particles. In the first place, the system of metal particles on a dielectric substrate can be coupled by electron tunneling and therefore can be conducting. However, the temperature and field dependence of the conductivity is different from that in continuous metal films and in bulk metals. Secondly, the dipoles which are induced in the particles by external alternating electromagnetic fields interact with each other giving rise to local fields. The local fields determine a diversity of phenomena in IMFs such as optical absorption and reflection, second harmonic generation, opto-acoustical effect etc. Thus there is a very broad scope of effects in which peculiar properties of small metal particles and their ensembles can come into play.

We will concentrate on the phenomena which occur in the process of feeding power into the electronic subsystem of IMFs. The power can be pumped by passing a current through the film and by laser or electron irradiation. In any case we are dealing with nonequilibrium electron–phonon systems. The most spectacular and unexpected peculiarity of IMFs is the possibility of generation of hot electrons in them under stationary (or quasistationary) conditions: the electron temperature can exceed by one to two orders of magnitude the lattice temperature of the islands which are sitting on a substrate with a good thermal conductivity. This effect appears unexpected, since the

hot electrons in continuous metal films and in bulk metals can be obtained just for very short times, when e.g. these objects are exposed to ultrashort laser pulses or to ultrashort electron pulses generated in explosion emission. Under such conditions, electrons are heated up during the time of $\sim 10^{-12}$ s. The lattice receives energy from the electron gas in $\sim 10^{-10}$ s, and the metal can be melted and evaporated after that if the pulse is powerful enough. By contrast, the hot electrons in IMFs can be generated under stationary conditions and without destruction of the film. In this section we will try to explain why this is possible.

The generation of hot electrons in IMFs allows one to understand the whole body of phenomena which occur when the films are excited by the conduction current as well as laser or electron irradiation. In particular, the model of hot electrons seems now to be the only model which accounts for the features of electron and photon emission from IMFs exposed to IR laser beams. It should be recalled that the electron emission is induced by photons whose energy is lower by a factor of 30–40 than the work function. This occurs at such laser beam intensities that the many-photon processes are unessential and the film remains stable for 10^3–10^4 h. No emission is observed under such irradiation intensities in bulk metals and continuous metal films.

As will be shown below, the heating of electrons in IMFs depends on the power pumped into the islands, on the special features of electron–lattice energy exchange in small particles and, finally, on the conditions of the heat transfer from the particles to the substrate. A strict analytical treatment of these factors will be given in Sections 6 and 7. In this section, we will begin with a graphic model which explains why the conditions in the small particles are favourable for nonequilibrium electron heating and then will discuss in more detail the consequences of the heating of the electron subsystem.

5.2. Heating up of electrons

Suppose power is fed into the electron subsystem of an IMF. This can be achieved by passing a current through the islands, which are coupled by transparent potential barriers, as well as by irradiation of the film by a laser or electron beam. Owing to existence of the electron–phonon interaction, the power absorbed by the electron subsystem is transferred to the phonon system of the islands and then is carried off to the substrate. It is evident from general considerations that the electron temperature should be higher than the lattice temperature. The point is how large this temperature difference can be and whether or not the IMF will be destroyed (melted and evaporated) through the power injection. Let us proceed from the system of equations that determine the electron (T_e) and phonon (T) temperature in a metal island:

$$\frac{\partial}{\partial t}(C_e T_e) = \mathrm{div}(K_e \nabla T_e) - \alpha(T_e - T) + Q \ , \tag{13}$$

$$\frac{\partial}{\partial t}(CT) = \mathrm{div}(K \nabla T) + \alpha(T_e - T) \ . \tag{14}$$

Here C_e and C are electron and phonon specific heats, K_e and K are electron and phonon heat conductivities, and Q is the specific power absorbed in the island. The coefficient α characterizes the intensity of electron–phonon interaction and correspondingly the product $\alpha(T_e - T)$ determines the power transferred from electrons to phonons. To avoid misunderstanding, it should be stressed

that the power is proportional to $(T_e - T)$ only in the case when this difference is not too large. In principle, the values Q, T_e and T can differ in different islands. The system of equations (13) and (14) is to be complemented by a boundary condition which describes the process of heat transfer from the metal island to the substrate.

But before discussing the specific behaviour of electrons in IMFs, it is appropriate to recall some basic data about the heating up of electrons in bulk metals [160]. Since the specific heat of the electron subsystem (C_e) is much smaller than that of phonons (C), the characteristic relaxation time for the electron temperature $\tau_e \sim C_e/\alpha$ is much shorter than the corresponding time for phonons.

To an order of magnitude, one usually has $\tau_e \sim 10^{-12}$ s and $\tau_{ph} \sim 10^{-10}$ s. For this reason the phonon temperature cannot change substantially in a time $t < \tau_e$, and during such a time the electrons behave as if they were thermally isolated. The result is that, in feeding power into the metal, the electron temperature grows very steeply until the energy flux from electrons to phonons becomes equal to the absorbed power, i.e.

$$\alpha(T_e - T) \approx Q \ . \tag{15}$$

During a time of $t \sim \tau_{ph}$ the phonon temperature in the bulk metal lines up with the electron temperature. This is the reason why, in bulk metals, the hot electrons can be observed only for times $t < \tau_{ph}$, e.g. by using short, but powerful laser pulses for irradiation [161]. The first basic difference between a bulk metal and small metal particles placed on a well heat-conducting substrate is that the lattice of the particles remains cold even when the electrons in them are strongly heated. The electron and phonon temperatures are not lined up even under steady-state conditions. Of course, the metal islands can be thermally destroyed, but only at power fluxes that are orders of magnitude higher than those sustained by bulk metals.

Let us dwell on this point in more detail. We shall consider the times $t > \tau_{ph}$ when the electron gas has already been heated up and condition (15) is obeyed. This means that all the power received by the electrons is being transferred to the lattice, so the variation of the electron temperature with time is connected only with the heating of the lattice. Then Eq. (14) with consideration of condition (15) transforms to

$$\frac{\partial}{\partial t}(CT) = \mathrm{div}(K\nabla T) + Q \ . \tag{16}$$

Instead of solving this equation with a boundary condition corresponding to an island on the substrate surface, we shall further simplify the problem and consider a small metal sphere inside a dielectric. Furthermore, let us assume for a while that C and K are the same for the metal sphere and its dielectric surroundings. The value Q is non-zero only inside the sphere. Such a model was exploited earlier in a study of the optical durability of laser glasses [162]. The solution of (16) under such conditions reads

$$T(\boldsymbol{r},t) = \frac{\kappa}{\pi^{3/2}K}\int_0^t \mathrm{d}t' \int \mathrm{d}\boldsymbol{r}\frac{Q(\boldsymbol{r}',t')}{[4\kappa(t-t')]^{3/2}}\exp\left\{-\frac{(\boldsymbol{r}-\boldsymbol{r}')^2}{4\kappa(t-t')}\right\} . \tag{17}$$

Here and below the phonon temperature is reckoned from its equilibrium value (at $Q = 0$), V is the volume of the metal sphere and $\kappa = K/C$. It is assumed that a power flux Q constant in the whole

volume of the sphere is turned on at a moment $t = 0$, i.e.

$$Q(\boldsymbol{r},t) = \begin{cases} Q_0 = \text{const}, & r < a,\ t \geq 0\ , \\ 0, & r > a\ , \end{cases} \tag{18}$$

where a is the radius of the sphere. Under such an assumption the integration of (17) can be readily performed to give the result

$$T(\boldsymbol{r},t) = \begin{cases} \dfrac{Q_0}{4K}\left\{\dfrac{4a^3}{3r} + \eta^2\left[U_0\left(\dfrac{r+a}{\eta}\right) - U_0\left(\dfrac{r-a}{\eta}\right)\right]\right\}, & r > a\ , \\ \dfrac{Q_0}{4K}\left\{2a^2 - \dfrac{2}{3}r^2 + \eta^2\left[U_0\left(\dfrac{r+a}{\eta}\right) - U_0\left(\dfrac{r-a}{\eta}\right)\right]\right\}, & r < a\ . \end{cases} \tag{19}$$

The following notations are used here:

$$U_0(x) = \left\{x - \frac{2}{3}\left(x^2 - \frac{1}{2}\right)\frac{\eta}{r}\right\}\frac{\mathrm{e}^{-x^2}}{\sqrt{\pi}} + \left\{x^2 + \frac{1}{2} - \frac{2}{3}x^2\frac{\eta}{r}\right\}\Phi(x)\ , \tag{20}$$

$\eta = \sqrt{4\kappa t}$ and $\Phi(x)$ is the probability integral. It can be seen that for $\eta \gg a$ solution (19) gives a steady-state phonon temperature

$$T(\boldsymbol{r},t) \approx \frac{Q_0}{4K}\begin{cases} \dfrac{4}{3}\dfrac{a^3}{r}, & r > a\ , \\ 2a^2 - \frac{2}{3}r^2, & r < a\ . \end{cases} \tag{21}$$

The steady-state regime is reached in a time $t > a^2/4\kappa$. This stationary solution can be obtained directly from Eq. (16) without using a rather cumbersome equation (19). In particular, by solution of Eq. (16) inside and outside the sphere and by joining the temperatures and heat fluxes at the boundary ($r = a$), one can easily find the temperature distribution in the situation when the parameter K is different for the sphere and its surroundings. For example, in the case when

$$K = \begin{cases} K_1, & r < a\ , \\ K_2, & r > a\ , \end{cases} \tag{22}$$

one obtains instead of solution (21) the following expression for the temperature inside the sphere:

$$T(\boldsymbol{r}) = \frac{Q_0}{3}\left\{\frac{a^2 - r^2}{2K_1} + \frac{a^2}{K_2}\right\}, \quad r < a\ . \tag{23}$$

By the way, this formula shows that, if the thermal conductivity of the sphere is substantially higher than that of the matrix, the temperature within the sphere is nearly constant. Such a situation is always valid for the metal particles whose size is smaller than the mean free path of electrons in the bulk metal. In this case the temperature everywhere within the sphere is constant and equal to

$$T \simeq \frac{Q_0}{3}\frac{a^2}{K_2}\ . \tag{24}$$

It is seen that the smaller the particle and the higher the thermal conductivity of the matrix, the lower is the temperature of the particle and hence the higher is its endurance against the injection of power. Expression (24) has been obtained under the condition that the sphere absorbs a power $Q_0 V = \frac{4}{3}\pi a^3 Q_0$ which is conveyed to the matrix through the sphere surface with the area $S = 4\pi a^2$. For a small metal particle of an arbitrary shape which has a volume V and a contact area with a substrate S_c, one easily arrives at an approximate formula

$$T \approx \frac{Q_0 V}{4 S_c K_2} R \ . \tag{25}$$

Here R is a characteristic dimension of the particle.

It should be noted that the thermal endurance of small metal particles on a heat-conducting substrate can be substantially higher when the power Q is fed in a pulsed regime. Suppose the pulse duration is τ. During this time the heat from the particle spreads within the substrate over a distance $l_\tau \sim \sqrt{4K\tau/C}$. For typical heat-conducting insulators and $\tau \sim 10^{-6}$ s, one will have $l_\tau \sim 10^{-5}$–10^{-4} cm. Thus, if a metal particle is about 10^{-6} cm in size, the energy $Q_0 V \tau$ absorbed in it during the time of the pulse disperses over a space in the substrate whose volume exceeds the particle volume by many orders of magnitude. This circumstance can substantially enhance the thermal endurance of small metal particles.

Up to this point we discussed only one of the peculiarities of IMFs as compared with bulk metals. To clarify their other specific features, it is necessary to come back to Eqs. (13) and (14). We have seen that the expression for the lattice temperature has a rather intricate shape (19) even under the most simplified assumptions. However, the essence of the problem can be appreciated using a simple graphic model, without cumbersome calculations.

5.3. A model of heating of the electron gas in IMFs

Consider a narrow vessel that is inserted into a wide vessel (Fig. 5.1). Their cross-sections are proportional to the specific heat of electrons (C_e) and phonons (C), respectively. Recall that $C_e \ll C$. A liquid is poured into the narrow vessel, its flux being equal to Q. Both the vessels have longitudinal slits in them. The slit in the narrow vessel has a width proportional to α and mimics the intensity of the heat transfer from electrons to phonons. Analogously, the slit in the wide vessel simulates the intensity of heat exchange between the island lattice and the substrate. The height of the liquid column in the narrow vessel corresponds to T_e and that in the wide vessel to T. Such a model simulates all the essential features of the solution of equation system (13) and (14) with appropriate boundary conditions. It should be noted also that the gradient terms $\mathrm{div}(K_e \nabla T)$ and $\mathrm{div}(K \nabla T)$ can be neglected for a small particle whose dimension is smaller than the electron mean free path, because in this case the temperatures T_e and T inside the particle do not depend on coordinates. Thus, if the flux of the liquid Q is switched on in a moment $t = 0$, one will observe the transition to a quasi-steady state after a rather short time $\tau_e \sim C_e/\alpha$. In this state all the flux poured into the narrow vessel flows out through the slit in it into the wide vessel. It means that the balance condition (15) is satisfied. The stabilization of the liquid level in the wide vessel is attained due to outflow of the liquid through the rather wide slit which mimics the good heat contact between the island and the substrate. The height of this level corresponds to the lattice temperature, which

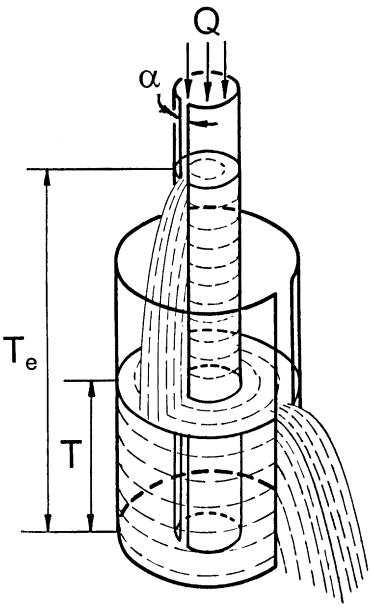

Fig. 5.1. A model of communicating vessels illustrating the electron–lattice energy transfer and nonequilibrium heating of the electron gas in a small particle on a substrate. See text for explanations.

obviously must be low enough to avoid the melting and evaporation of the island. As can be seen from this model and Eq. (15), the gap between the temperatures of electrons and phonons is wider the larger is the energy flux Q and the smaller is the electron–phonon coupling coefficient α:

$$(T_e - T) \approx Q/\alpha \ .$$

The high-energy-transmitting endurance of IMFs has already been discussed in Section 5.2. Let us now point out further two unique features of these films.

(a) The intensity of the electron–lattice energy exchange, denoted above as α, can be by a few orders of magnitude lower in a small metal island than in the bulk metal.

(b) Much higher energy fluxes can be injected into small metal islands without their destruction than into bulk metals.

These peculiarities will be considered at length in Sections 6 and 7. Here we shall give only some introductory explanations. Concerning point (a), it should be noted that the main energy losses of hot electrons in bulk metals are due to generation of acoustic phonons by Cherenkov's mechanism [163,164]. In a small metal particle whose dimensions are smaller than the mean free path of electrons in the volume, the character of electron scattering drastically changes. Electrons now execute mainly a quasi-periodic motion from one wall of the particle to another, and the Cherenkov mechanism of energy dissipation becomes inefficient under such conditions. The electron energy losses are caused in this case by the surface scattering and the coefficient α can be lower by orders of magnitude than in the bulk (see Section 6). As to point (b), the injection of high-energy fluxes into small metal islands can be implemented, e.g. through laser irradiation or through conduction current excitation. In the former case, large Q values are attained owing to

peculiarities of light absorption by small metal particles in the range of infra-red CO_2 laser generation. The underlying physics is detailed in Section 7. In the conduction current excitation, the high-energy fluxes are provided by formation of the conduction channels with a high current density (see Section 3). The islands with hot electrons arise just within these channels. We have dealt with this issue in Section 2.4.

To summarize, we list again the main physical factors that can ensure the appearance of hot electrons in IMFs in stationary or quasi-stationary conditions. These are the high thermal endurance of small metal particles on the heat-conducting substrate, the suppression of the electron–lattice energy exchange in such particles, and the possibility of pumping high energy fluxes into them.

5.4. Phenomena caused by hot electrons in IMFs

Here we shall discuss some important phenomena attributed to the generation of hot electrons in IMFs:

(a) deviations from Ohm's law, i.e. the occurrence of non-linear conduction current–voltage characteristics;
(b) electron emission from IMFs;
(c) photon emission from IMFs.

The explanation of effect (a) is fairly evident. As noted above, the conduction current through an IMF is effected by electrons tunneling from one island to another. The tunneling occurs mainly at energies close to the Fermi level. At low electric fields, the tunneling current between two adjacent islands is proportional to the offset of their Fermi levels, so Ohm's law is obeyed. At higher fields, the heating of electrons sets in and a group of electrons is generated with energies above the Fermi level. The contribution of the hot electrons depends on the electron temperature, which in its turn depends on the applied field. This results in a nonlinear current–voltage characteristics. Their shape was specified in more detail in Section 3.2 where the experimental findings were discussed.

As considered above, the electron emission from IMFs can be induced by the conduction current as well as by laser irradiation of the films. In both the cases the hot electrons are generated. A theoretical estimation given in Section 3 and experimental measurements show that the electron temperature in small metal islands can amount to $\sim 10^3$ K while the lattice remains virtually cold. Therefore, what is observed is interpreted as a Richardson emission of the hot (nonequilibrium) electrons with the current

$$I_e \propto e^{-\varphi/k_B T_e} . \tag{26}$$

Here φ is the work function of the island and k_B is the Boltzmann constant. As indicated in Section 3.3, under current excitation of the films the electron emission arises when the conduction current–voltage characteristics start to deviate from the linearity. This seems to be evident, since both the effects have the same origin: generation of hot electrons.

In the case of laser excitation, the emission current represents a kind of photoresponse of the film to the IR irradiation. However, there is no way to interpret this phenomenon as a one-photon or many-photon photoemission. The one-photon photoeffect is impossible because a CO_2 infra-red laser generates quanta whose energy (~ 0.12 eV) is lower by a factor of 30–40 than the work

function of the islands. On the other hand, the intensity of the laser beams used in the experiments was far too low to bring about a many-photon electron emission. Contrary to these mechanisms, we ascribe the effect to the absorption of the laser beam power by the whole ensemble of electrons of the island. The electrons are heated up in a time $\tau_e \sim 10^{-12}$ s, so again the Richardson emission of the hot electrons becomes possible.

The inference about the central role of the hot electrons in the peculiar properties of IMFs appears all the more credible when one considers the whole body of experimental data on the nonlinear conduction current–voltage characteristics, and the electron and light emission. Let us now address the mechanisms of the light emission.

5.5. *Mechanisms of light emission from IMFs*

Recall that the photons are emitted from the spots about 1 μm in size. The spots are visible to the naked eye which means that at least some of the emitted quanta have energies which are about 20 times as high as the energy of exciting quanta in the case of the infra-red laser irradiation. The possibility of generation of hot electrons in IMFs, the existence of numerous tunnel junctions in the films, the rough surface geometry and, in some cases, the presence of microscopic connecting bridges between the islands, all can be responsible for occurrence of a variety of light radiation mechnisms in IMFs. A list of possible one-electron and many-electron radiation mechanisms in IMFs can include bremsstrahlung of the hot electrons; radiation generated in the inelastic tunneling of electrons from one island to another; inverse photoeffect; transitions between discrete energy levels in the connecting bridges; radiative decay of collective electron excitations. For small particles, the plasma frequency is substantially dependent on the shape and relative position of the particles, the existence of bridges between them and other factors [165,166]. This diversity of mechanisms is the reason why the spectrum of the light radiation from IMFs can extend from infra-red frequencies to the frequencies of volume plasmons. The necessity to satisfy simultaneously the conservation laws for energy and momentum makes impossible both radiation and absorption of photons by free-moving electrons. However, such a possibility arises when an electron interacts with phonons or a surface. If the island dimension is larger than the mean free path of electrons, they are scattered mainly on phonons. In the opposite case the surface scattering is dominant. The scattering can be both elastic and inelastic, but photons can be radiated or absorbed in the latter case only. If the electron subsystem is nonequilibrium (i.e. hot electrons are present), the generation of photons prevails. Below we shall consider the radiative transitions in inelastic surface scattering and inelastic electron tunneling between adjacent islands [167].

The time-dependent Schroedinger equation for an electron moving inside the particle in the field of an electromagnetic wave reads

$$i\hbar\frac{\partial\psi}{\partial t} = \left\{\frac{1}{2m}\left(\hat{\boldsymbol{p}} - \frac{e}{c}\boldsymbol{A}\right)^2 + U(x)\right\}\psi \ . \tag{27}$$

Here $\boldsymbol{A}$ is the vector potential of the electromagnetic field inside the particle. In the case when one calculates the energy absorbed by the particle, this field should be determined from the external electromagnetic field. This point will be addressed in Section 7. Here we shall focus mainly on the radiation mechanisms.

A model surface potential barrier with a finite width will be considered later, but first we suppose that a one-dimensional barrier has a step-like shape

$$U(x) = \begin{cases} 0, & x \le 0 \ , \\ U, & x > 0 \ . \end{cases} \tag{28}$$

The time dependence of $\boldsymbol{A}(t)$ is assumed to be

$$\boldsymbol{A}(t) = \boldsymbol{A}^{(0)}\{e^{i\omega t} + e^{-i\omega t}\} \ , \tag{29}$$

where ω is the frequency and $\boldsymbol{A}^{(0)}$ a constant vector amplitude. Considering $\boldsymbol{A}$ as a weak perturbation, Eq. (27) can be linearized against $\boldsymbol{A}$ and its solution can be represented as follows:

$$\psi(\boldsymbol{r}, t) = \psi^{(0)}(\boldsymbol{r})e^{-(i\varepsilon/\hbar)t} + i\frac{2e}{\hbar}\sum_{+,-} \boldsymbol{A}^{(0)}\boldsymbol{\Phi}^{(\pm)}(\boldsymbol{r})e^{-(i/\hbar)(\varepsilon \pm \hbar\omega)t} \ . \tag{30}$$

Here ε is the electron energy, $\psi^{(0)}(\boldsymbol{r}, t)$ is the solution of Eq. (27) at $\boldsymbol{A} = 0$ and $\boldsymbol{\Phi}^{(\pm)}$ is a vector function to be determined. The equations necessary for finding $\Phi_x^{(\pm)}(\boldsymbol{r})$, $\Phi_y^{(\pm)}(\boldsymbol{r})$, $\Phi_z^{(\pm)}(\boldsymbol{r})$ can be obtained by substitution of solution (30) into a linearized equation (27) and by equating the coefficients standing at identical components of the vector $\boldsymbol{A}$. In particular, for the function $\Phi_x^{(\pm)}(\boldsymbol{r})$ one obtains

$$\left\{\Delta + \frac{2m}{\hbar^2}(\varepsilon \pm \hbar\omega - U(x))\right\}\Phi_x^{(\pm)}(\boldsymbol{r}) = \frac{\partial}{\partial x}\psi^{(0)}(\boldsymbol{r}) \ . \tag{31}$$

Assuming that $\boldsymbol{A}^{(0)}$ in (29) is a constant vector we have neglected the spatial dispersion. In this approximation the terms in (30) proportional to $\Phi_y^{(\pm)}(\boldsymbol{r})$ and $\Phi_z^{(\pm)}(\boldsymbol{r})$ do not contribute to the inelastic current. For this reason we shall not write down equations for them. The problem of the coordinate dependence of local fields within small metal particles will be analyzed in more detail in Section 7.

It is clear from Eq. (30) that the sign " + " in the function $\Phi_x^{(\pm)}(\boldsymbol{r})$ corresponds to absorption and the sign " − " to the radiation induced by an external field. We are interested in a spontaneous rather than induced radiation. Let us show how the probability of the spontaneous radiation can be found from the probability of induced radiation. To this end we shall write down the function $\psi^{(0)}(\boldsymbol{r})$ in its explicit form:

$$\psi^{(0)}(\boldsymbol{r}) = \psi^{(0)}(x)e^{i(k_y y + k_z z)} \ . \tag{32}$$

Here k_i are the components of the wave vector and the function $\psi^{(0)}(x)$ for the step-like barrier (28) has a standard form

$$\psi^{(0)}(x) = e^{ik_x x} + R_0 e^{-ik_x x} \quad \text{at } x \le 0 \ , \tag{33}$$

$$\psi^{(0)}(x) = \begin{cases} Fe^{i\kappa_0 x}, & \varepsilon_x \ge U, \ x > 0 \ , \\ F'e^{-\kappa_0 x}, & \varepsilon_x \le U, \ x > 0 \ . \end{cases} \tag{34}$$

In (34), ε_x is the component of energy corresponding to the motion of an electron normal to the barrier:

$$\varepsilon_x = (1/2m)(\hbar k_x)^2 \ . \tag{35}$$

We also use the notation

$$\kappa_0 = \{(2m/\hbar^2)|U - \varepsilon_x|\}^{1/2} . \tag{36}$$

The unknown coefficients R_0, F and F' are determined from the smooth joining of functions (33) and (34) at $x = 0$. It can be readily proved that the solution of Eq. (31) can be represented as

$$\Phi_x^{(\pm)}(\boldsymbol{r}) = \pm \frac{\hbar}{2m\omega} \frac{\partial}{\partial x} \psi^{(0)}(\boldsymbol{r}) + \varphi^{(\pm)}(x) e^{i(k_y y + k_z z)} , \tag{37}$$

where the function $\varphi^{(\pm)}(x)$ has the following form:

$$\varphi^{(\pm)}(x) = \begin{cases} de^{-iqx}, & x \le 0, \\ ge^{i\gamma x}, & x \ge 0,\ \varepsilon_x \pm \hbar\omega \ge U , \\ g' e^{-\gamma x}, & x \ge 0,\ \varepsilon_x \pm \hbar\omega \le U . \end{cases} \tag{38}$$

In (38) we have used the notations

$$q = \sqrt{\frac{2m}{\hbar^2}(\varepsilon_x \pm \hbar\omega)} , \tag{39}$$

$$\gamma = \sqrt{\frac{2m}{\hbar^2}|\varepsilon_x \pm \hbar\omega - U|} . \tag{40}$$

Since we are considering the radiation, it is natural to assume that $\varepsilon_x > \hbar\omega$. The unknown coefficients d, g, g' in Eq. (38) can be determined from the continuity condition for the function $\Phi_x^{(\pm)}(\boldsymbol{r})$ and its derivative at $x = 0$ [122]. In doing so we can find an explicit expression for the function $\Phi_x^{(\pm)}(\boldsymbol{r})$ and hence calculate the required probabilities of the inelastic transitions. Indeed, taking into account (37) and (38) and substituting function (30) into the expression for the current density

$$I_x = \frac{e\hbar}{i2m} \left\{ \psi^* \frac{\partial \psi}{\partial x} - \psi \frac{\partial \psi^*}{\partial x} \right\} , \tag{41}$$

one can calculate the elastic and inelastic (i.e. connected with $\varphi^{(\pm)}(x)$) component of the current density. Relating then the inelastic component to the incident flux ($I_x^{(0)} = \hbar k_x/m$), we obtain the probability of the inelastic transitions

$$D^{(\pm)}(\varepsilon_x, \omega) = \frac{I_x^{(n)}}{I_x^{(0)}} = \left(\frac{2e}{c\hbar} A_x^{(0)} \right)^2 \frac{q}{k_x} |d|^2 . \tag{42}$$

After the determination of d and its substitution into (42), we arrive at the result

$$D^{(\pm)}(\varepsilon_x, u) = \frac{2}{m\omega^2} \left(\frac{2eA_x^{(0)}}{c\hbar} \right)^2 \begin{cases} \sqrt{\varepsilon_x(\varepsilon_x \pm \hbar\omega)}, & \varepsilon_x < U,\ \varepsilon_x \pm \hbar\omega \le U , \\ \sqrt{\varepsilon_x(\varepsilon_x + \hbar\omega)}\Gamma(\varepsilon_x + \hbar\omega), & \varepsilon_x \le U,\ \varepsilon_x + \hbar\omega \ge U , \\ \sqrt{\varepsilon_x(\varepsilon_x - \hbar\omega)}\Gamma(\varepsilon_x), & \varepsilon_x \ge U,\ \varepsilon_x - \hbar\omega \le U , \\ \sqrt{\varepsilon_x(\varepsilon_x \pm \hbar\omega)}\Gamma(\varepsilon_x \pm \hbar\omega), & \varepsilon_x \ge U,\ \varepsilon_x \pm \hbar\omega \ge U . \end{cases} \tag{43}$$

The function $\Gamma(\varepsilon_x)$ has here the form

$$\Gamma(\varepsilon_x) = \frac{U}{(\sqrt{\varepsilon_x} + \sqrt{\varepsilon_x - U})^2} . \tag{44}$$

In (43), the case $\varepsilon_x \le U$, $\varepsilon_x \pm \hbar\omega \le U$ describes the usual bremsstrahlung for the " + " sign and the inverse effect for the " − " sign. The case $\varepsilon_x \le U$, $\varepsilon_x + \hbar\omega > U$ corresponds to the surface photoeffect and the case $\varepsilon_x \ge U$, $\varepsilon_x - \hbar\omega < U$ to the inverse surface photoeffect. Finally, the situation $\varepsilon_x \ge U$, $\varepsilon_x \pm \hbar\omega \ge U$ represents a usual inelastic scattering at the potential barrier.

Before addressing the problem of the spectral density of the radiation, let us briefly turn to the inelastic tunneling between the islands. Instead of Eq. (16), one has in this case

$$U(x) = \begin{cases} 0, & x \le 0 , \\ U, & 0 \le x < a_0 , \\ 0, & x > a_0 . \end{cases} \tag{45}$$

The solution procedure remains the same with the difference that, instead of Eqs. (33) and (34), one uses the functions corresponding to potential (45) and the functions $\varphi^{(\pm)}(x)$ from (38) must be replaced by

$$\varphi^{(\pm)}(x) = \begin{cases} d e^{-iqx}, & x \le 0 , \\ f_1 e^{\gamma x} + f_2 e^{-\gamma x}, & 0 \le x \le a_0 , \\ g e^{iqx}, & x \ge a_0 . \end{cases} \tag{46}$$

The details of the calculations can be found in Appendix A.

In addition, the procedure of joining the functions and their derivatives should be carried out not only at $x = 0$, but also at $x = a_0$. In this case the probability of the inelastic scattering with absorption (the sign " + ") and radiation (the sign " − ") of photons is given by

$$D^{(\pm)}(\varepsilon_x, \omega) = \left(\frac{2e}{c\hbar} A_x^{(0)}\right)^2 \frac{q}{k_x} |g|^2 . \tag{47}$$

Here

$$|g|^2 = 4\left(\frac{U}{\hbar\omega}\right)^2 \frac{k_x^2}{G(\kappa_0, k_x) G(\gamma, q)} \{\gamma^2 \kappa_0^2 (\mathrm{ch}\,\gamma a_0 - \mathrm{ch}\,\kappa_0 a_0)^2 + (\kappa_0 q \,\mathrm{sh}\,\gamma a_0 - \gamma k_x \,\mathrm{sh}\,\kappa_0 a_0)^2\} \tag{48}$$

and $\mathrm{sh}\,x$, $\mathrm{ch}\,x$ are respectively hyperbolic sine and cosine. We also have introduced the notation

$$G(\kappa_0 k_x) = (\kappa_0^2 - k_x^2)^2 sh^2 \kappa_0 a_0 + 4\kappa_0^2 k_x^2 ch^2 \kappa_0 a_0 . \tag{49}$$

The above method of calculation, within a unified approach, of all processes connected with the inelastic electron reflection from the barrier and the inelastic tunneling was first used to this end in [122].

The radiative transitions considered up to this point correspond to transitions induced by the external field. To obtain the probabilities of spontaneous transitions which we need, we are using the following artificial expedient [168]. Let us choose such a normalization of the vector potential of the electromagnetic field that the field quantization volume V_0 will contain in the average $N_{\rm ph}$ photons characterized by the energy $\hbar\omega$ and a given wave vector and polarization. Under such conditions one obtains

$$A^{(0)} = c\left(\frac{2\pi\hbar}{V_0}\frac{N_{\rm ph}}{\omega}\right)^{1/2} . \tag{50}$$

To calculate the probability of spontaneous transitions, it is necessary to substitute (50) into (42) (or (43)) and (47) and then to set $N_{\rm ph} = 1$. In this way we shall obtain the probabilities of spontaneous transitions into the field state with a given polarization, frequency ω and wave vector $\boldsymbol{q}_{\rm ph}$. To find the full probability of radiation in a unit frequency interval and a solid angle $\mathrm{d}\Omega$, the probabilities obtained above should be multiplied by the density of the final state of the field equal to

$$\mathrm{d}\rho(\omega) = \frac{V_0 q_{\rm ph}^2 \mathrm{d}q_{\rm ph}}{(2\pi\hbar)^3 \mathrm{d}\omega}\,\mathrm{d}\Omega = \frac{V_0}{(2\pi c)^3}\omega^2\,\mathrm{d}\Omega . \tag{51}$$

The total probability of spontaneous radiation in inelastic electron reflection from the barrier or the inelastic tunneling is given by

$$W_{\rm e} = [D^{(-)}(\varepsilon_x,\omega)]_{N_{\rm ph}=1}\cdot \mathrm{d}\rho(\omega) . \tag{52}$$

The spectral density of radiation of all electrons into a solid angle $\mathrm{d}\Omega$ from the surface area S equals

$$\begin{aligned}\mathrm{d}\mathscr{E}(\omega,\Omega) &= \frac{2\hbar\omega S}{(2\pi\hbar)^3}\int_{\varepsilon_x\geq\hbar\omega}^{\infty}\mathrm{d}p_x\, v_x W_{\rm e}(\varepsilon_x,\omega)\int_{-\infty}^{\infty}\int_{-\infty}^{\infty}\mathrm{d}p_y\,\mathrm{d}p_z f(\varepsilon)[1-f(\varepsilon-\hbar\omega)]\\ &= \frac{2m\theta_{\rm e}}{(2\pi\hbar)^2}S\omega[\exp(\hbar\omega/\theta_{\rm e})-1]^{-1}\cdot\int_{\varepsilon_x\geq\hbar\omega}^{\infty}\mathrm{d}\varepsilon_x W(\varepsilon_x,\omega)Z(\varepsilon_x\omega) .\end{aligned} \tag{53}$$

In this expression, $f(\varepsilon)$ is the Fermi function with an effective electron temperature $\theta_{\rm e} = k_{\rm B}T_{\rm e}$ and $Z(\varepsilon_x,\omega)$ is

$$Z(\varepsilon_x,\omega) = \ln\frac{1+\exp((\mu+\hbar\omega-\varepsilon_x)/\theta_{\rm e})}{1+\exp((\mu-\varepsilon_x)/\theta_{\rm e})} , \tag{54}$$

where μ is the Fermi energy. Having the explicit expressions for the probability of inelastic electron reflection from the barrier (43) and of the inelastic tunneling (47), it is easy to calculate, using formula (53), the spectral density of radiation in any specific case of barrier parameters, frequency range etc. Unfortunately, a simple analytical expression for the general case does not exist. It can be obtained only in various limiting cases. For instance, in the frequency interval

$$\theta_{\rm e} < \hbar\omega < \varphi,\mu , \tag{55}$$

the total spectral density of radiation in all directions is

$$\mathscr{E}(\omega) = S\frac{2e^2}{3(2c\hbar)^3}\hbar\omega \mathrm{e}^{-\hbar\omega/\theta_{\rm e}}\left\{\mu(\mu+\hbar\omega)-\frac{2}{3}(\hbar\omega)^2\right\} . \tag{56}$$

In the case specified by condition (55) the main contribution to the radiation stems from bremsstrahlung of hot electrons occurring in their collision with the surface barrier.

It is instructive to compare the above quantum mechanical treatment of the bremsstrahlung with its classical description. The total (to all directions) power of bremsstrahlung from a charge moving with an acceleration $\dot{v}$ is known to be

$$\frac{\mathrm{d}\mathscr{E}}{\mathrm{d}t} = \frac{2}{3}\frac{e^2}{c^3}\dot{v}^2 \ . \tag{57}$$

Hence the total energy radiated during the time of the acceleration is

$$\mathscr{E} = \int_{-\infty}^{\infty} \frac{\mathrm{d}\mathscr{E}}{\mathrm{d}t}\mathrm{d}t = \frac{2}{3\pi}\frac{e^2}{c^3}\int_0^{\infty} \mathrm{d}\omega \left[\int_{-\infty}^{\infty} \dot{v}\mathrm{e}^{-\mathrm{i}\omega t}\,\mathrm{d}t\right]^2 \ . \tag{58}$$

Since the change of the velocity of an electron in its collision with a step-like barrier occurs jumpwise, the value ωt in the exponent of formula (58) can be neglected, which gives a simple expression for the spectral density of radiation:

$$\mathscr{E}(\omega) = \frac{2}{3\pi}\frac{e^2}{c^3}|\Delta v|^2 \ . \tag{59}$$

Here Δv is the change in the velocity of an electron in its reflection from the barrier ($\Delta v = 2v_x$). Thus we arrive at the result

$$\mathscr{E}(\omega) = \frac{8}{3\pi}\frac{e^2}{c^3}v_x^2 = \frac{16}{3\pi}\frac{e^2}{mc^3}\varepsilon_x \ . \tag{60}$$

In the quantum mechanical treatment, expressions (52), (43) and (50) give for the contribution of an electron to the spectral density of the bremsstrahlung

$$\hbar\omega W_{\mathrm{e}} = (\cos\theta')^2\frac{2e^2}{\pi^2c^3}\frac{\sqrt{\varepsilon_x(\varepsilon_x - \hbar\omega)}\,\mathrm{d}\Omega}{m} \ . \tag{61}$$

Here θ' is the angle between the vector of the electric field in the radiated wave and the normal to the surface. The integration of (61) over all angles under the condition $\varepsilon_x \gg \hbar\omega$ gives the expression that is exactly coincident with (60).

In closing this section let us address briefly the radiation generated in the inelastic tunneling. In the case

$$\kappa_0 a_0 > 1 \ , \tag{62}$$

relations (47) and (52) predict that the probability of the tunneling accompanied by the radiation of a quantum $\hbar\omega$ equals

$$W_{\mathrm{e}} = \frac{4e^2\hbar}{\pi^2m^2c^3U}\sqrt{\varepsilon_x(\varepsilon_x - \hbar\omega)}\kappa_0^2\mathrm{e}^{-2a_0\kappa_0}\cos^2\theta'\,\mathrm{d}\Omega \ . \tag{63}$$

Hence, the spectral density of this radiation into a solid angle $d\Omega$ is

$$d\mathscr{E}(\omega,\Omega) \approx S\frac{2e^2\theta_e\omega}{\pi^4 m\hbar c^3 U}\cos^2\theta' d\Omega \int_{\hbar\omega}^{U} d\varepsilon_x \sqrt{\varepsilon_x(\varepsilon_x-\hbar\omega)}\, e^{(\mu-\varepsilon_x)/\theta_e}\cdot\kappa_0^2 e^{-2a_0\kappa_0} \ . \tag{64}$$

It should be kept in mind that the integrand in (64) is not quite accurate at both the lower and the upper limit of integration. The inaccuracy at the lower limit is due to the necessity of taking into account Pauli's exclusion principle for the states with $\varepsilon_x < \mu$. The inaccuracy at the upper limit is caused by the fact that condition (62) is not obeyed at $\varepsilon_x \to U$. However, these inaccuracies are partially compensated by other physical factors and for this reason cannot significantly influence the value of integral (64). Indeed, the inaccuracy of the approximation at the lower integration limit is partially counterbalanced by the very low tunneling probability (because of the inequality $a_0\kappa_0 \gg 1$). At the upper limit, there are very few electrons with high energies (for which one has $a_0\kappa_0 < 1$). Therefore, no substantial error will be made if one assumes $\hbar\omega < \mu$ at $(\varepsilon_x)_{\min} \approx \mu$ and determines $(\varepsilon_x)_{\max}$ from the condition $(\varepsilon_x)_{\max} \approx U - \hbar^2/2ma_0^2$. This procedure gives

$$\int_{\hbar\omega}^{U} d\varepsilon_x \sqrt{\varepsilon_x(\varepsilon_x-\hbar\omega)}\, e^{(\mu-\varepsilon_x)/\theta_e}\cdot\kappa_0^2 e^{-2a_0\kappa_0}$$

$$\approx \int_{\mu}^{U-\hbar^2/2ma_0^2} d\varepsilon_x \sqrt{\varepsilon_x(\varepsilon_x-\hbar\omega)}\, e^{(\mu-\varepsilon_x)/\theta_e}\cdot\kappa_0^2 e^{-2a_0\kappa_0} \ . \tag{65}$$

Using the theorem of the mean we can take outside the integral sign the value of the function $\sqrt{\varepsilon_x-\hbar\omega}$ at a point $\varepsilon_x = \varepsilon_0$. The remaining integral does not depend on the frequency. As follows from (64) and (65), the spectral density of the radiation generated in the inelastic tunneling can decrease very slowly with growing frequency. This may explain why many photons emitted from IMFs have energies which exceed the energy of excitation photons (in the case of IR laser irradiation) by a factor of ten and more. The radiation mechanisms connected with the decay of plasmon excitations in IMFs were discussed in Section 4.

5.6. *Summary of Section 5*

In this section, we formulated and discussed on a qualitative level three factors which ensure the generation of hot electrons in IMFs: the strong attenuation of the electron–lattice energy exchange in small metal particles; the high power density throughput of the small particles sitting on a substrate with a good thermal conductivity; the favorable conditions which exist for pumping high power densities into small metal particles. We have also presented a simple model which illustrates, using a hydrodynamic analogy, the interplay of these factors in the nonequilibrium heating of electrons in IMFs.

Then we substantiated in detail one of the three factors listed above, namely, the high throughput capacity of the small metal particles which enables them to pass high energy fluxes without destruction. We also considered the consequences of the nonequilibrium heating of electrons: the electron and photon emission from IMFs. In what follows we shall treat at length theoretically the remaining two factors: the electron–lattice energy exchange in small metal particles (Section 6) and the possibility of feeding high power densities into them using IR laser irradiation (Section 7).

6. Electron–lattice energy exchange in small metal particles

6.1. Introductory remarks

As noted in Sections 3 and 5, one of the reasons for the generation of hot electrons in IMFs is the sharp attenuation of the electron–lattice energy exchange in particles with dimensions smaller than the electron mean free path. Contrary to the situation in bulk metals where the motion of electrons is mostly rectilinear and is only occasionally interrupted by scattering acts, their motion in small particles is oscillation-like, because electrons "fly" ballistically from one wall to another changing very frequently the direction of the motion. We will show below that this change in the character of the motion can strongly suppress the intensity of the electron–lattice energy exchange. It should be recalled that the lower this value, the larger will be the difference between the electron and lattice temperatures at a given power absorbed by the electron subsystem.

Atomic vibrations in a small metal particle and interaction of electrons with them can be treated either classically or quantum-mechanically, the choice being the matter of convenience. In Section 6.2, we shall apply the former approach to describe the generation of acoustic phonons by a moving electron. The corresponding classical equation is derived from first principles in Section 6.6. The main losses of energy of hot electrons in a bulk metal are due to Cherenkov generation of acoustic waves by electrons whose velocity is much larger than the sound speed. This mechanism is highly efficient, but it vanishes in small particles where the motion of electrons becomes oscillation-like [126,169]. In the latter case, the energy losses are determined mainly by mechanisms of surface scattering of electrons. These processes can be treated more conveniently in the quantum-kinetical approach. The corresponding results are presented in Sections 6.3, 6.4 and 6.6.

6.2. Peculiarities of the electron–lattice energy transfer in island metal films

As noted above, the power gained from the field, static under the current heating or high-frequency under the laser irradiation, is transferred by electrons to lattice vibrations (phonons) and then drained to the substrate via heat conduction. In the framework of the classical approach [163,164] the electron energy losses are treated as the Cherenkov generation of acoustic waves by the moving electrons whose energies exceed the Fermi energy. Both classical and quantum kinetic approaches were shown [164] to yield the same expression for the electron energy losses. The classical approach suits us better because it offers a simpler description of the peculiarities of electron motion in metal islands with characteristic dimensions smaller than the mean free path.

The Cherenkov generation of acoustic waves is known to be the dominant mechanism of hot-electron energy losses in the bulk of metals. In what follows emphasis is given to the proof of the assertion that this dissipation mechanism may vanish in the metal island whose dimensions are smaller than some critical value.

The longitudinal acoustic vibrations generated by the moving electron (i.e. the longitudinal vibrations that are responsible for the losses under consideration) are known to be described by the equation [164]

$$(\partial^2 \boldsymbol{u}/\partial t^2) - s^2 \Delta \boldsymbol{u} = -(\Lambda/\rho)\nabla\delta(\boldsymbol{r} - \boldsymbol{r}(t)) \,. \tag{66}$$

Here $\boldsymbol{u}$ is the longitudinal component of the displacement vector, s is the sound velocity in the metal, ρ is the density, Λ is the electron–lattice interaction constant, $\boldsymbol{r}(t)$ is classical electron path (trajectory), and $\boldsymbol{r}$ and t are the coordinate and time. In an infinite medium $\boldsymbol{r}(t) = \boldsymbol{v}t$, where $\boldsymbol{v}$ is the electron velocity.

The Fourier expansion of the force proportional to $\nabla\delta(\boldsymbol{r} - \boldsymbol{v}t)$ in Eq. (66) shows that there are harmonics for all frequencies and, consequently, there exist relevant conditions for the resonant excitation of all lattice vibrations. A distinguishing feature of metal particles smaller than the electron mean free path, which is governed by the scattering by lattice vibrations, is that there occur harmonic oscillations with frequencies of the order of v/L, where L is the characteristic size of the metal particle. In this case, the driving force does not contain all harmonics and, as soon as electron oscillation frequency exceeds the limiting Debye frequency, resonant interaction between a moving electron and lattice vibrations becomes impossible and hence, the Cherenkov losses vanish.

A brief mathematical substantiation of the above arguments may be to the point. To take into account the peculiarities of a finite system, it is sufficient, as will be shown later, to study the periodical electron motion only in one direction, i.e., to assume that

$$\boldsymbol{r}(t) = \{\boldsymbol{r}_\perp = const, z = \phi(t)\} \ , \tag{67}$$

where $\phi(t)$ is a periodic function of time. The Fourier expansion of Eq. (66) is given by

$$\boldsymbol{u} \equiv \nabla\chi = \nabla \sum_{k_l = -\infty}^{\infty} \int \mathrm{d}\boldsymbol{k}_\perp \tilde{\chi}(\boldsymbol{k}_\perp, k_l) \mathrm{e}^{\mathrm{i}(\boldsymbol{k}_\perp \cdot \boldsymbol{r}_\perp + k_l z)} \ . \tag{68}$$

Substitution of (68) in (66) yields the following equation for $\tilde{\chi}$:

$$\frac{\partial^2 \tilde{\chi}}{\partial t^2} + \omega^2(\boldsymbol{k})\tilde{\chi} = -\frac{1}{8\pi^2}\frac{\Lambda}{\rho L}\mathrm{e}^{-\mathrm{i}k_l\phi(t)} \ , \tag{69}$$

where $\omega^2(\boldsymbol{k}) = s^2(k_\perp^2 + k_l^2)$.

The electron energy losses due to the generation of lattice vibrations are given by [164]

$$\frac{\mathrm{d}\varepsilon}{\mathrm{d}t} = \Lambda \int \frac{\partial \boldsymbol{u}}{\partial t} \nabla\delta(\boldsymbol{r} - \boldsymbol{r}(t)) \mathrm{d}^3 r = \Lambda \sum_{(k_l)} \int \mathrm{d}\boldsymbol{k}_\perp (k_\perp^2 + k_l^2) \frac{\partial \tilde{\chi}}{\partial t} \mathrm{e}^{-\mathrm{i}k_l\phi(t)} \ , \tag{70}$$

$$\frac{\partial}{\partial t} u_z \bigg|_{z = \pm L} = 0 \ . \tag{71}$$

Here $2L$ is the size of the system along the z-axis. The solution of Eq. (69) can be written as

$$\tilde{\chi} = -\frac{\Lambda}{8\pi^2 \rho L \omega(\boldsymbol{k})} \int_0^t \mathrm{d}t' \, \mathrm{e}^{-\mathrm{i}k_l\phi(t')} \sin[\omega(\boldsymbol{k})(t - t')] \ . \tag{72}$$

Substituting this solution into (70), we get

$$\frac{\mathrm{d}\varepsilon}{\mathrm{d}t} = -\frac{\Lambda^2}{8\pi^2 \rho' L} \int \mathrm{d}\boldsymbol{k}_\perp (k_\perp^2 + k_l^2) \int_0^t \mathrm{d}t' \cos[\omega(\boldsymbol{k})(t - t')] \mathrm{e}^{\mathrm{i}k_l[\phi(t) - \phi(t')]} \ . \tag{73}$$

Assuming now that the electron oscillating motion is described by $\phi(t)$ and taking it in the simplest form

$$\phi(t) = L\sin\left(\frac{v}{L}t\right), \tag{74}$$

we can easily estimate, within the context of (73), how the finite size of the system influences the electron–lattice energy exchange.

First of all, we shall show that for $L \to \infty$, (73) yields the known equation for hot-electron energy losses in an infinite medium [164]. Note that for $L \to \infty$, $t \to \infty$, we have

$$\int_0^t \mathrm{d}t' \cos\left[\omega(\boldsymbol{k})(t-t')\right]\cos\left[k_l(\phi(t)-\phi(t'))\right] = \frac{\pi}{2}\{\delta[k_l v + \omega(\boldsymbol{k})] + \delta[k_l v - \omega(\boldsymbol{k})]\}\ .$$

When deriving the latter equation, it is important to keep a proper order in proceeding to the limits (first $L \to \infty$, then $t \to \infty$). As a result, we obtain from (73) (for $L \to \infty$, $t \to \infty$):

$$\frac{\mathrm{d}\varepsilon}{\mathrm{d}t} = -\frac{\Lambda^2}{8\pi^2\rho L}\int \mathrm{d}\boldsymbol{k}\, k^2\omega(\boldsymbol{k})\delta[(kv)^2 - \omega^2(\boldsymbol{k})]\ . \tag{75}$$

The result, given in Ref. [164], follows from (75) immediately.

Now let us consider a finite system. We employ the following expansion:

$$\mathrm{e}^{-\mathrm{i}k_l\phi(t)} = \mathrm{e}^{-\mathrm{i}k_l L\sin(vt/L)} = \sum_{n=-\infty}^{\infty} J_n(k_l L)\mathrm{e}^{-\mathrm{i}nv/t}\ ,$$

where J_n is the Bessel function. This expansion makes in possible to reduce (73) to the form

$$\frac{\mathrm{d}\varepsilon}{\mathrm{d}t} = -\frac{\Lambda^2}{8\pi^2\rho L}\sum_{(k_l)}\int \mathrm{d}\boldsymbol{k}_\perp(k_\perp^2 + k_l^2)\sum_{(n)}\sum_{(+,-)}\frac{J_n(k_l L)}{n\,v/L \pm \omega(\boldsymbol{k})}$$
$$\times\left\{\sin\left[n\frac{v}{L}t - k_l\phi(t)\right] + \sin[\pm\omega(\boldsymbol{k})t + k_l\phi(t)]\right\}. \tag{76}$$

Hence, we see that $\mathrm{d}\varepsilon/\mathrm{d}t$ is a rapidly oscillating function for $t \to \infty$. If $v/L > \max\omega(\boldsymbol{k}) \equiv \omega_\mathrm{D}$ (ω_D is the Debye frequency), i.e. in the absence of resonances, then the mean value of this oscillating function tends to zero since the averaging procedure implies the operation $1/t\int_0^t \mathrm{d}t'\mathrm{d}\varepsilon/\mathrm{d}t'$ for $t \to \infty$.

Thus, we have shown that the electron motion under consideration is not accompanied by the energy losses associated with the Cherenkov generation of acoustic lattice vibrations, though the latter mechanism of energy dissipation is dominant in bulk metals.

In the case of an infinite metal, the expression for the total losses (due to all hot electrons) can be derived by multiplying (76) by the number of electrons with energies exceeding the Fermi energy (only such electrons can generate lattice vibrations). As a result, this expression can be reduced (see Ref. [164]) to the form $\alpha(T_\mathrm{e} - T)$ where

$$\alpha = \frac{\pi^2}{6}nv\frac{ms^2}{T} \tag{77}$$

(n is the electron concentration).

For small metal particles, whose characteristic size L satisfies the inequality

$$v_F/L > \omega_D \tag{78}$$

(where v_F is electron velocity on the Fermi surface), these bulk losses have been shown to vanish.

6.3. Surface vibrations of small particles

Since we will be discussing metal particles with dimensions on the order of or less than the mean free path, we can use the following model to calculate the surface energy exchange.

The electron gas is in a spherical potential well of radius R_0 (if thermal vibrations are ignored) and height V_0. This model was used in Ref. [170] to study optical absorption in island metal films.

As we have already mentioned, the reason for the energy exchange is an interaction of the electron with thermal vibrations of the surface. These vibrations can be classified somewhat crudely as either shape vibrations (so-called capillary vibrations), in the course of which the volume does not change, or surface vibrations, which are accompanied by a change in density (acoustic vibrations). A theory for the surface vibrations of a spherical particle is set forth in detail (for the case of vibrations of the surface of an atomic nucleus) in Ref. [171].

We begin our analysis with the capillary vibrations. We expand the radius of the vibrating surface in spherical harmonics $Y_{\lambda\mu}(\theta,\varphi)$:

$$R(\theta,\varphi) = R_0\left\{1 + \sum_{\lambda\mu} \alpha_{\lambda\mu} Y_{\lambda\mu}(\theta,\varphi)\right\}. \tag{79}$$

The Hamiltonian of the capillary vibrations can then be written in the following form, in accordance with Ref. [171]:

$$H = \frac{1}{2}\sum_{\lambda\mu} \{D_\lambda|\dot{\alpha}_{\lambda\mu}|^2 + C_\lambda|\alpha_{\lambda\mu}|^2\} \equiv \frac{1}{2}\sum_{\lambda\mu} \left\{\frac{|\pi_{\lambda\mu}|^2}{D_\lambda} + D_\lambda\omega_\lambda^2|\alpha_{\lambda\mu}|^2\right\}. \tag{80}$$

Here $\pi_{\lambda\mu} = D_\lambda\dot{\alpha}^*_{\lambda\mu}$ is a generalized momentum, and $\omega_\lambda = (C_\lambda D_\lambda)^{1/2}$ is the frequency of the capillary vibrations. The constants D_λ and C_λ depend on the island dimensions in different ways. According to Ref. [171], they are given by

$$D_\lambda = MnR_0^5/\lambda, \qquad C_\lambda = \sigma_s R_0^2(\lambda-1)(\lambda+2). \tag{81}$$

Here M is the mass of the atom, n is the density, and σ_s is the surface energy.

It can be seen from (81) that the frequency of the shape vibrations depends strongly on the radius of the metal island, R_0:

$$\omega_\lambda = \left(\frac{C_\lambda}{D_\lambda}\right)^{1/2} = \left\{\sigma_s\frac{(\lambda-1)\lambda(\lambda+2)}{MnR_0^3}\right\}^{1/2}. \tag{82}$$

For the discussion below we will take a quantum-mechanical approach in which $\pi_{\lambda\mu}$ and $\alpha_{\lambda\mu}$ are replaced by corresponding operators, which are related to the operators of creation ($b^+_{\lambda\mu}$) and

annihilation ($b_{\lambda\mu}$) of surface phonons by

$$\hat{\pi}_{\lambda\mu} = \mathrm{i}(D_\lambda \hbar\omega_\lambda/2)^{1/2}(b_{\lambda\mu} - b^+_{\lambda\mu}) \,, \tag{83}$$

$$\hat{\alpha}_{\lambda\mu} = \left(\frac{\hbar}{2D_\lambda\omega_\lambda}\right)^{1/2}(b_{\lambda\mu} + b^+_{\lambda\mu}) \,. \tag{84}$$

After this replacement, the Hamiltonian of the capillary vibrations takes the standard form:

$$\hat{H} = \sum_{\lambda\mu} \hbar\omega_\lambda\left(b^+_{\lambda\mu}b_{\lambda\mu} + \frac{1}{2}\right) . \tag{85}$$

To find the electron–phonon energy exchange, we need an explicit expression for the corresponding Hamiltonian. According to the model adopted above, the potential energy of an electron in a metal island is

$$W(r) = V_0\Delta(r - R(\theta,\varphi)) \,, \tag{86}$$

where

$$\Delta(x) = \begin{cases} 1, & x > 0 \,, \\ 0, & x < 0 \,. \end{cases} \tag{87}$$

Using expansion (79) for $R(\theta,\varphi)$, we find from (86)

$$W(r) \approx V_0\Delta(r - R_0) + \delta(r - R_0)V_0R_0\sum_{\lambda\mu}\alpha_{\lambda\mu}Y_{\lambda\mu}(\theta,\varphi) \,. \tag{88}$$

The second term in (88) describes the energy of the electron–phonon interaction associated with the surface vibrations. Writing this term in the second-quantization representation [using (84)], we find

$$\hat{H}_{\mathrm{int}} = V_0R_0\sum\left(\frac{\hbar}{2D_\lambda\omega_\lambda}\right)^{1/2}\langle\psi^*_{lnm}|\delta(r - R_0)Y^*_{\lambda\mu}(\theta,\varphi)|\psi_{l'n'm'}\rangle(b_{\lambda\mu} + b^+_{\lambda\mu})a^+_{lnm}a_{l'n'm'} \,. \tag{89}$$

The operators a^+_{lnm} and $a_{l':n'm'}$ in (89) create and annihilate an electron in the corresponding state. The meaning of the subscripts on these operators becomes clear when we recall that the electron wave function in a "spherical potential square well" is

$$\psi_{lnm}(r) = \frac{1}{C_{ln}}R_l(r)Y_{lm}(\theta,\varphi) \,. \tag{90}$$

Here C_{ln} is a normalization factor, and the radial wave function is

$$R_l(r) = \begin{cases} j_l(k'_{l:n}r), & \text{for } r < R_0 \,, \\ h^{(1)}_l(\mathrm{i}K_{l:n}r) & \text{for } r > R_0 \,. \end{cases} \tag{91}$$

The quantity $j_l(x)$ in (91) is the spherical Bessel function, and $h^{(1)}_l(x)$ is the spherical Hankel function. In addition,

$$k'_{ln} = \left(\frac{2m_{\mathrm{e}}}{\hbar^2}\varepsilon_{ln}\right)^{1/2}, \qquad K_{ln} = \left[\frac{2m_{\mathrm{e}}}{\hbar^2}(V_0 - \varepsilon_{ln})\right]^{1/2} . \tag{92}$$

Here m_{e} is the mass of an electron, and ε_{ln} is the energy of the electronic levels in a spherical square potential well. These conditions are found from the condition for the joining of the electron

wave function and its derivative at the point $r = R_0$. In view of the rapid decay of the electron wave function inside the barrier, we write k'_{ln} in the following form, as in Ref. [170]:

$$k'_{ln} = k_{ln} + \Delta k_{ln} \ , \tag{93}$$

where k_{ln} are the roots of the equation

$$j_l(k_{ln}R_0) = 0 \ . \tag{94}$$

Eq. (94) corresponds to the case of an infinitely deep potential well. Assuming that Δk_{ln} is small in comparison with k_{ln} (this point is easily checked), we find the following result from the condition for the joining of the wave function and its derivative at the point R_0:

$$\Delta k_{ln} = \ - k_{ln}/R_0 K_{ln} \ . \tag{95}$$

Here we have used the asymptotic expression

$$R_{ln}(r) \approx \frac{1}{\mathrm{i}Kr}\exp\left\{ - Kr - \frac{\mathrm{i}\pi}{2}(l+1)\right\}, \quad r > R_0 \ . \tag{96}$$

Since we will be interested below in the electron levels near (and above) the Fermi energy, we can use the method of Ref. [170], finding approximate solutions of (94) through the use of the asymptotic representation of the spherical Bessel function:

$$k_{ln} = \frac{\pi}{2R_0}(2n + l) \ . \tag{97}$$

Now, in accordance with (93), (95), and (97), we have an explicit expression for k'_{ln}. Consequently, the electron wave functions in (90) and (91) have been determined completely. Using them, we can put the Hamiltonian for the electron–photon interaction, (89), in the form

$$H_{\mathrm{int}} = V_0 \sum \left\{ \frac{2\hbar}{D_\lambda \omega_\lambda} \ \frac{\varepsilon_{l:n}\varepsilon_{l':n'}}{(V_0 - \varepsilon_{ln})(V_0 - \varepsilon_{l'n'})} \right\}^{1/2} \int_0^{2\pi} \mathrm{d}\varphi \int_0^{\pi} \mathrm{d}\theta \sin\theta \, Y_{ln} \cdot (\theta, \varphi)$$
$$\times \, Y_{l'n'}(\theta, \varphi)(b_{\lambda\mu} + b^+_{\lambda\mu}) a^+_{lnm} a_{l'n'm'} \ . \tag{98}$$

6.4. Surface electron–phonon energy exchange

Now that we have explicit expressions for the electron and photon spectra and also for the Hamiltonian of the electron–photon interaction, we can move to the problem of determining the electron–photon exchange. This exchange can be taken into account systematically by a kinetic-equation approach. For brevity, we will be using the notation

$$v = \{l, n, m\}, \qquad q = \{\lambda, \mu\} \ . \tag{99}$$

The change per unit time in the distribution of electrons among states caused by the scattering of electrons by phonons is then given by

$$\frac{\partial f_{vv}}{\partial t} \equiv I f_{vv} = \sum_{v'q} W_{vv'q} \{ [(N_q + 1) f_{vv}(1 - f_{v'v'}) - N_q f_{v'v'}(1 - f_{vv})] \delta[\varepsilon_{v'} - \varepsilon_v + \hbar\omega_q]$$
$$+ [N_q f_{vv}(1 - f_{v'v'}) - (N_q + 1) f_{v'v'}(1 - f_{vv})] \delta[\varepsilon_{v'} - \varepsilon_v - \hbar\omega_q] \} \ . \tag{100}$$

Here $f_{vv} = \langle a_v^+ a_v \rangle$ is the electron distribution function, and $N_q = \langle b_q^+ b_q \rangle$ the phonon distribution function. As usual, the angle brackets mean an average over the statistical operator. Furthermore, in our case we have $\varepsilon_v = \varepsilon_{ln}$, $\omega_q = \omega_\lambda$, i.e., the spectrum is degenerate. It is simple matter to derive an explicit expression for the transition probabilities, by first writing the interaction Hamiltonian (98) in the compact form

$$\hat{H}_{\text{int}} = \sum_{v,v',q} C_{v,v',q}[b_q + b_q^+]a_v^+ a_{v'} \ . \tag{101}$$

Then

$$W_{v,v',q} = \frac{2\pi}{\hbar}|C_{v,v',q}|^2 \ . \tag{102}$$

The energy transferred from the electrons to the phonons per unit time is

$$\frac{\partial \mathscr{E}}{\partial t} = \frac{\partial}{\partial t}\sum \varepsilon_v f_{vv} = \sum \varepsilon_v I f_{vv} \ . \tag{103}$$

We note that the electron distribution in a metal island, f_{vv}, depends on only the electron energy: $F_{vv} = f(\varepsilon_v)$.

Treating the phonon system as a heat reservoir (with respect to the electron subsystem), we take the phonon distribution function N_q to be Planckian with a temperature T. Expanding collision integral (100) in a series in the small quantity $\hbar\omega_q$ (i.e., actually expanding in the ratio of the phonon energy to the Fermi energy), we find the following result for expression (103):

$$\frac{\partial \mathscr{E}}{\partial t} \approx \sum_{v,v',q} W_{v,v',q} N_q (\hbar\omega_q)^2 \left\{ \frac{f(\varepsilon_v)[1 - f(\varepsilon_{v'})]}{k_B T} \right\} \delta(\varepsilon_{v'} - \varepsilon_v) \ . \tag{104}$$

We can now write an explicit expression for the electron distribution function. Because of the intense electron–electron interaction, the power acquired by the electron subsystem from the external source becomes distributed among many electrons rapidly. As a result, a Fermi distribution with some effective electron temperature T_e, is established:

$$f(\varepsilon_v) = \left\{ \exp\left[\frac{\varepsilon_v - \varepsilon_F}{k_B T_e} \right] + 1 \right\}^{-1} , \tag{105}$$

where ε_F is the Fermi energy. Substituting (105) into (104), we find

$$\frac{\partial \mathscr{E}}{\partial t} = \left(\frac{T_e}{T} - 1 \right) \sum_{v,v',q} W_{v,v',q} N_q (\hbar\omega_q)^2 (\varepsilon_{v'} - \varepsilon_v) \delta(\varepsilon_v - \varepsilon_F) \ . \tag{106}$$

To pursue the calculations we need to use the explicit expression for $W_{v,v',q}$ which follows from (102) and from a comparison of (98) and (101):

$$W_{v,v',q} = \frac{4\pi}{(V_o - \varepsilon_{ln})(V_o - \varepsilon_{l'n'})} \left\{ \int_0^{2\pi} d\varphi \int_0^{\pi} d\theta \sin\theta Y_{ln}(\theta,\varphi) Y_{l'n'}(\theta,\varphi) Y_{\lambda\mu}(\theta,\varphi) \right\}^2 \ . \tag{107}$$

Substituting (107) into (106) we find that an explicit dependence of the integrand on the indices characterizing the electron states remains only in the spherical harmonic, because of the presence of the function $\delta(\varepsilon_v - \varepsilon_F) \equiv \delta(\varepsilon_{ln} - \varepsilon_F)$ in the integral. We can thus sum over the electron indices (96). In doing so, we make use of the orthogonality of the spherical harmonics:

$$\sum_{l=0}^{\infty} \sum_{m=-l}^{l} Y_{lm}(\theta, \varphi) Y_{lm}(\theta', \varphi') = \frac{\delta(\varphi - \varphi')\delta(\theta - \theta')}{\sin\theta} \ . \tag{108}$$

In our case the summation over l is bounded by the condition $\varepsilon_{ln} < \varepsilon_F$. This circumstance does not introduce any significant error, however, since the maximum value of l is large, $l_{max} \sim 10^2$. This estimate of l_{max} follows from the relation

$$\varepsilon_F = \left(\frac{\hbar\pi l_{max}}{2R_0}\right)^2 \frac{1}{2m_e} \ . \tag{109}$$

As a result of these calculations, we find from (106)

$$\frac{\partial \mathscr{E}}{\partial t} \approx \left(\frac{T_e}{T} - 1\right)\frac{R_0^4}{2\pi^2}\left(\frac{m_e \varepsilon_F}{\hbar}\right)^2\left(\frac{V_0}{\varphi_0}\right)^2 \sum_{\lambda\mu} \frac{\omega_\lambda N_\lambda}{D_\lambda} \ . \tag{110}$$

Here $\varphi_0 = V_0 - \varepsilon_F$ is the work function of the metal, and $N_\lambda = N(\omega_\lambda)$ is the Planckian distribution function of the capillary vibrations.

We are left with the task of evaluating the phonon sum in (110):

$$\sum_{\lambda=2}^{\lambda_{max}} \sum_{=-\lambda}^{\lambda} \frac{\omega_\lambda N(\omega_\lambda)}{D_\lambda} \approx \frac{k_B T}{\hbar} \sum_{\lambda=2}^{\lambda_{max}} \frac{2\lambda + 1}{D_\lambda} \ . \tag{111}$$

In (111) we have recognized that the energy corresponding to the Debye frequency of the capillary vibrations is considerably smaller than $k_B T$ (at room temperature). It follows from (82) in this case that

$$\omega_D = \omega_{\lambda\,max} \approx \left(\frac{\sigma_s}{MnR_o^3}\right)^{1/2} \lambda_{max}^{1/2} \ . \tag{112}$$

As a result of these calculations we find

$$\frac{\partial \mathscr{E}}{\partial t} \approx \left(\frac{4\pi R_0^3}{3}\right) k_B (T_e - T) \frac{3}{16\pi} \frac{v_F}{R_0} n \frac{m_e \omega_D^2}{\sigma_s}\left(\frac{V_0}{\varphi_0}\right)^2 \ . \tag{113}$$

In the literature, the power transferred from the electrons to the phonons is customarily written in the form

$$\frac{\partial \mathscr{E}}{\partial t} = \left(\frac{4\pi R_0^3}{3}\right) \alpha (T_e - T) \ . \tag{114}$$

Here we have assumed that the particle is a sphere in our case. The constant α, which is a measure of the rate of the electron-phonon energy exchange, is given in our case by

$$\alpha = \frac{3}{16\pi} k_B \frac{v_F}{R_0} n \frac{m_e \omega_D^2}{\sigma_s}\left(\frac{V_0}{\varphi_o}\right)^2 \ . \tag{115}$$

Let us evalute this quantity for a gold particle (a sphere) with the following parameter values: $n = 6\times10^{22}\,\mathrm{cm}^{-3}$, $v_F = 10^8\,\mathrm{cm/s}$, $R_0 = 10^{-6}\,\mathrm{cm}$, $\sigma_s = 10^3\,\mathrm{erg/cm}^2$, $\omega_D = 3\times10^{12}\,\mathrm{s}^{-1}$ [165], and $(V_0/\varphi_0)^2 = 5$. We find $\alpha = 2\times10^{15}\,\mathrm{erg/(cm^3\,s\,deg)}$.

The value found for α is two orders of magnitude lower than the corresponding value in bulk metals. An experiment carried out to determine α in small particles has confirmed this estimate [172]. A reduction in the intensity of electron–phonon interaction in small particles has also been found experimentally in another recent work [173]. In this work, a somewhat different system has been studied than in our case (a dielectric core surrounded by an ultrathin Au shell).

As we mentioned earlier, in addition to the shape vibrations (the capillary vibrations) of the particles there are surface vibrations which do involve a change in density (acoustic vibrations). The dispersion relation for these phonons is

$$\omega_{n\lambda} = k_{n\lambda}s\ , \tag{116}$$

where s is the sound velocity, and the wave vector $k_{n\lambda}$ is determined by the roots of the equation

$$j_\lambda(k_{n\lambda}R_0) = 0\ . \tag{117}$$

The interaction of the electrons with these vibrations can be dealt with by an approach like that taken above. As a result we find the following expression for the value of α determined by the surface acoustic vibrations:

$$\alpha \approx \frac{1}{16\pi}k_s\frac{nv_F}{R_0^2}\frac{m_e}{\rho}\left(\frac{\omega_D'}{s}\right)^2\left(\frac{V_0}{\varphi_0}\right)^2\ . \tag{118}$$

Here ω_D' is the Debye frequency of the acoustic vibrations, and ρ is the density of the material.

An estimate of α from (52) for the same gold particles as discussed above yields a value an order of magnitude smaller than the result in (49). Consequently, the interaction with capillary waves is predominant for these particles. We would simply like to point out that the idea of classifying the vibrations as either capillary or acoustic is valid only if ω_D and ω_D' are substantially different. This condition is satisfied in the case under consideration here.

6.5. Derivation of the equation describing the sound generation by hot electrons

The Hamiltonian of the interaction of an electron, residing in point $\boldsymbol{r}$, with atoms of the lattice can be written as

$$H_{\mathrm{int}} = \sum_{\boldsymbol{n}}\{V(\boldsymbol{r}-\boldsymbol{R}_{\boldsymbol{n}}-\boldsymbol{u}(\boldsymbol{n})) - V(\boldsymbol{r}-\boldsymbol{R}_{\boldsymbol{n}})\} \approx -\sum_{\boldsymbol{n}}\boldsymbol{u}(\boldsymbol{n})\frac{\partial}{\partial\boldsymbol{r}}V(\boldsymbol{r}-\boldsymbol{R}_{\boldsymbol{n}})\ . \tag{119}$$

Here V is an atomic potential, $\boldsymbol{R}_{\boldsymbol{n}}$ is the radius vector of the nth lattice point and $\boldsymbol{u}(\boldsymbol{n})$ is a small displacement of the nth atom from its equilibrium position due to lattice vibrations. For a simple cubic lattice we have

$$\boldsymbol{R}_{(\boldsymbol{n})} = \sum_{i=1}^{3} n_i\boldsymbol{a}_i^{(0)}\ , \tag{120}$$

where $\boldsymbol{a}_i^{(0)}$ is the translation vector. The potential energy of the lattice vibrations can be expressed in a standard way in terms of small displacements of the atoms from their equilibrium positions:

$$P = \frac{1}{2}\sum_{\boldsymbol{n},\boldsymbol{n}'} \hat{A}(\boldsymbol{n}-\boldsymbol{n}')\boldsymbol{u}(\boldsymbol{n})\boldsymbol{u}(\boldsymbol{n}') \,, \tag{121}$$

where $\hat{A}(n)$ is a force matrix. Taking into account the kinetic energy of atoms with a mass M

$$K = \frac{1}{2}M\sum_{\boldsymbol{n}} \dot{\boldsymbol{u}}^2(\boldsymbol{n}) \tag{122}$$

and the energy of their interaction with an electron, one obtains an equation for lattice vibrations:

$$M\ddot{\boldsymbol{u}}(\boldsymbol{n}) + \sum_{\boldsymbol{n}'} \hat{A}(\boldsymbol{n}-\boldsymbol{n}')\boldsymbol{u}(\boldsymbol{n}') = -\frac{\partial}{\partial \boldsymbol{u}(\boldsymbol{n})}H_{\mathrm{int}} = \frac{\partial}{\partial \boldsymbol{r}}V(\boldsymbol{r}-\boldsymbol{R}_n) \,. \tag{123}$$

In most cases the electron–lattice interaction can be treated in a continuum approximation where the discrete vector is considered as a continuous one. Bearing in mind the short-range character of interatomic interactions we can also use the expansion

$$\boldsymbol{u}(\boldsymbol{n}') \simeq \boldsymbol{u}(\boldsymbol{n}) + \left(\boldsymbol{l}\frac{\partial}{\partial \boldsymbol{n}}\right)\boldsymbol{u}(\boldsymbol{n}) + \frac{1}{2}\left(\boldsymbol{l}\frac{\partial}{\partial \boldsymbol{n}}\right)^2\boldsymbol{u}(\boldsymbol{n}) + \cdots \,. \tag{124}$$

Here $\boldsymbol{l} \equiv \boldsymbol{n}' - \boldsymbol{n}$. Besides, let us take into account that

$$\sum_{\boldsymbol{l}} \hat{A}(\boldsymbol{l}) = 0, \quad \sum_{\boldsymbol{l}} \hat{A}(\boldsymbol{l})\boldsymbol{l} = \boldsymbol{0} \,. \tag{125}$$

The former of these conditions considers that the elastic energy of the lattice does not change if the crystal is displaced as a whole while the latter one allows for the symmetry $\boldsymbol{A}(\boldsymbol{l}) = \boldsymbol{A}(-\boldsymbol{l})$. The substitution of (124) into (123) with conditions (125) gives

$$M\ddot{u}_i(\boldsymbol{n}) + \frac{1}{2}\sum_{\boldsymbol{l}} A_{ij}(\boldsymbol{l})l_\alpha l_\beta \frac{\partial^2}{\partial n_\alpha \partial n_\beta}u_j(\boldsymbol{n}) = \frac{\partial}{\partial x_i}V(\boldsymbol{r}-\boldsymbol{R}_n) \,. \tag{126}$$

Taking into account Eq. (120), expression (126) can be written for the simple cubic lattice as

$$M\ddot{u}_i + \left(\frac{1}{2}\sum_{\boldsymbol{l}} A_{ij}(\boldsymbol{l})R_\alpha(\boldsymbol{l})R_\beta(\boldsymbol{l})\right)\frac{\partial^2}{\partial R_\alpha \partial R_\beta}u_j = \frac{\partial}{\partial x_i}V(\boldsymbol{r}-\boldsymbol{R}) \,. \tag{127}$$

We have thus obtained an equation known from the theory of elasticity of continuous media which has a general form

$$\rho\ddot{u}_i - \lambda_{iklm}\nabla_k\nabla_l u_m = g_i \,. \tag{128}$$

Here ρ is the density of the medium and g_i is a component of the external force. In the approximation of the isotropic continuum, an elastic medium is characterized by two elastic constants: modulus of dilatation (K_0) and shear modulus (μ_0). For such a medium, instead of (127) or (128), one obtains

$$\frac{\partial^2}{\partial t^2}\boldsymbol{u} - \frac{1}{\rho}\left\{\left(K_0 + \frac{\mu_0}{3}\right)\boldsymbol{\nabla}_R(\boldsymbol{\nabla}_R\boldsymbol{u}) + \mu_0\nabla_R^2\boldsymbol{u}\right\} = \frac{1}{\mu}\boldsymbol{\nabla}_r V(\boldsymbol{r}-\boldsymbol{R}) \,. \tag{129}$$

The full displacement vector $\boldsymbol{u}$ can be represented as the sum of its longitudinal and transverse components:

$$\boldsymbol{u} = \boldsymbol{u}_{\parallel} + \boldsymbol{u}_{\perp}; \quad \nabla \times \boldsymbol{u}_{\parallel} = 0; \quad \nabla \boldsymbol{u}_{\perp} = 0 \ . \tag{130}$$

Combining (129) and (130), we have

$$\frac{\partial^2}{\partial t^2}\boldsymbol{u}_{\parallel} - s^2 \nabla_R^2 \boldsymbol{u}_{\parallel} = \frac{1}{\mu}\nabla_r V(\boldsymbol{r} - \boldsymbol{R}) \ . \tag{131}$$

Here $s^2 = (K_0 + \mu_0/3)/\rho$ is the square of the longitudinal speed of sound. The expression for $\boldsymbol{u}_{\perp}$ will not be given here because its right side does not contain the force which could generate such displacements.

Now it remains to carry out the last step in obtaining the equation that has been used in [164] to treat the electron–lattice energy exchange in bulk metals. Let us again take into account that the atomic potential is short-range in character. This allows the following approximation in the description of the long waves in lattice vibrations:

$$\frac{1}{\mu}V(\boldsymbol{r} - \boldsymbol{R}) \approx \frac{\Lambda \Omega_0}{\mu}\delta(\boldsymbol{r} - \boldsymbol{R}) = \frac{\Lambda}{\rho}\delta(\boldsymbol{r} - \boldsymbol{R}) \ , \tag{132}$$

where Ω_0 is the unit cell volume and Λ is a constant having the dimensions of energy. To clarify the physical meaning of Λ, turn again to Eq. (119):

$$H_{\text{int}} = -\sum_{\boldsymbol{n}} \boldsymbol{u}(\boldsymbol{n}) \frac{\partial}{\partial \boldsymbol{r}} V(\boldsymbol{r} - \boldsymbol{R}_{\boldsymbol{n}}) \approx -\frac{1}{\Omega}\frac{\partial}{\partial \boldsymbol{r}} \int \mathrm{d}^3 R \, \boldsymbol{u}(\boldsymbol{R}) V(\boldsymbol{r} - \boldsymbol{R})$$

$$\approx \Lambda \frac{\partial}{\partial \boldsymbol{r}} \int \mathrm{d}^3 R \, \boldsymbol{u}(\boldsymbol{R}) \delta(\boldsymbol{r} - \boldsymbol{R}) = -\Lambda \operatorname{div} \boldsymbol{u}(\boldsymbol{r}) \ . \tag{133}$$

It is seen that under the assumptions used, H_{int} is reduced to the known Bardeen and Shockley deformation potential. Hence the constant Λ represents the constant in this potential.

In (131) and (132), $\boldsymbol{r}$ is a radius vector which determines the electron position. If the electron moves along a trajectory, one should write $\boldsymbol{r}(t)$ instead of $\boldsymbol{r}$. The vector $\boldsymbol{r}(t)$ determines the coordinates of the electron in a moment t. Besides, in Eq. (119) the notation $\boldsymbol{r}$ is used instead of $\boldsymbol{R}$. In other words, Eq. (119) follows from Eq. (131) under the change of notations $\boldsymbol{r} \to \boldsymbol{r}(t)$ and $\boldsymbol{R} \to \boldsymbol{r}$.

6.6. Concluding remarks about electron–lattice energy exchange

The results presented above demonstrate that the main mechanism of electron-lattice energy exchange operating in bulk metals does not function in small metal particles. In the latter case, hot electrons lose their energy in surface collisions. The first crude estimations of the surface energy exchange in small metal particles were made in [70]. The fraction of the energy transferred by an electron in its collision with a surface atom was taken to be proportional to the ratio of masses of the electron and atom. In [174], this part was assumed to be proportional to the ratio of the

electron mass to the total mass of surface atoms within a circle with a diameter λ_e, where λ_e is the electron wavelength. The number of these atoms equals $(\pi/4)\lambda_e^2 n_s$ (n_s is the concentration of the surface atoms). Since $n_s \approx n^{2/3}$ and $\lambda_e = 2\pi\hbar/m_e v_F \simeq 2/n^{1/3}$, the result agrees with the result [70] to within a factor of the order of unity. Such an estimate has been used in Section 3. However, this approximation can be justified only for electrons with the energy considerably higher than the Fermi energy. Electrons having low energies interact with the surface as a whole rather than with individual atoms. A theory of such an interaction has been considered above. The theory gives an analytical expression for the constant of the surface electron–lattice energy exchange. The value of this constant appears lower by two orders of magnitude than the analogous constant in the volume. This estimate has been corroborated experimentally [172]. Therefore, the suppression of the electron–lattice energy exchange in small metal particles does occur and this effect must favour the generation of hot electrons.

7. Optical absorption by small metal particles

7.1. Introductory remarks

In this section we shall concentrate on the peculiarities of optical absorption by small metal particles and their ensembles. The particle dimensions are assumed to be smaller than the wave length of the electromagnetic field. On the other hand, the dimensions may be either a smaller or larger than the electron mean free path. Depending on this inequality, either a surface or volume absorption mechanism is dominant. If the particles are small in the sense just specified, the most characteristic feature is the extremely high sensitivity of their optical absorbance in the IR range to the particle shape and to wave polarization. We shall see that under equal conditions, the power absorbed by particles which have the same volume but distinct shapes can differ by orders of magnitude. The same is true for absorption of the electromagnetic waves with different polarizations. These peculiarities play the decisive role in our model that explains electron and photon emission from IMFs exposed to a powerful IR laser irradiation (see Sections 3 and 5). These emissions depend exponentially on the electron temperature which, in turn, is determined by the power being absorbed. This is the reason why strongly nonuniform emission currents are usually observed from an IMF which, on the average, is uniform. In other words, the emission is determined not by the average, but rather by an extremal absorption of individual islands comprising the film.

It should be noted that optical absorption by small metal particles has been investigated for long, and many relevant results have been published in monographs (see e.g. [165,175,176]). However, a number of important regularities of absorption as a function of particle shape and wave polarization have been elucidated only quite recently [177,178]. To better understand the difficulties emerging in the development of the all-embracing theory of optical absorption by small metal particles, let us remind the absorption mechanisms. A substantial role in the absorption by small particles is played both by the electric and magnetic components of the incident electromagnetic wave. The electric component induces a local potential field inside the metal particle, and this brings about the so-called electric absorption. The magnetic component of the incident wave induces inside the particle an eddy electric field and eddy (Foucault's) currents. The corresponding

absorption is named the magnetic absorption. Depending on the size and shape of the particles, either electric or magnetic absorption can prevail. Therefore, a well-founded theory must involve simultaneous evaluation of both electric and magnetic components of absorption for particles whose dimensions can be either smaller or larger than the electron mean free path.

For the particles smaller than the electron mean free path, the particle shape affects not only the values of the local fields, but also the character of optical conductivity, which characterizes the response of the system to these fields. The optical conductivity of asymmetric particles is a tensor with components dependent on particle shape.

Thus, the construction of a coherent theory of total absorption by small particles requires the calculation of local potential and eddy fields corresponding to specific particle shapes, as well as currents induced by these fields. However, the implementation of this program encounters formidable difficulties. In particular, one fails in calculating the magnetic absorption for the nonspherical particles shaped as a finite cylinder or a parallelepiped for which one can carry out an exact evaluation of the electric absorption. Considerable attention has also been given to ellipsoidal particles (see e.g. [165]), but only the particles with dimensions larger than the electron mean free path have been considered and the tensor of optical conductivity for them has not been calculated. The above-mentioned and many other works have been concerned with the resonance (plasmon) absorption and with the effect of the interaction between the small particles on the absorption.

In recent years, a method has been developed which allows, for the first time, a unified approach to calculation of electric and magnetic absorption by ellipsoidal particles whose dimensions can be both smaller and larger than the electron mean free path [177,178]. The present section describes this method and some results derived by it. Since the theory of electric absorption by metal particles shaped as a sphere [170], cylinder [179] or parallelepiped [180] and having dimensions smaller than the electron mean free path was based on a quantum mechanical approach, this method will also be reviewed in Section 7.7. Section 7.8 is devoted to discussion of the resonance (plasmon) optical absorption in IMFs.

Let us briefly dwell on the practical importance of this problem. Obviously, the pronounced dependence of the optical absorption by small particles on their shape, wave polarization and other parameters can be exploited to tailor the reflectance and absorbance of surfaces by deposition of coatings which contain appropriate metal particles. In space, small particles can be dangerous for satellites, but a laser beam can be used to destroy the particles if one knows how to tune the beam to their maximum absorbance. Ensembles of small particles deposited onto surfaces or embedded into matrices can exhibit a specific opto-acoustic effect [181], generate second harmonics [182] and manifest other nonlinear effects. In recent years, a considerable attention has also been focused on dusty gaseous plasmas containing clusters and small particles, including metal ones (see e.g. [183,184]). Evidently, the radiative and absorbing ability of such plasmas can substantially be determined by the properties of the small particles.

7.2. Statement of the problem

Consider a metal particle exposed to an electromagnetic wave

$$\begin{pmatrix} \boldsymbol{E} \\ \boldsymbol{H} \end{pmatrix} = \begin{pmatrix} \boldsymbol{E}^{(0)} \\ \boldsymbol{H}^{(0)} \end{pmatrix} \exp\{\mathrm{i}(\boldsymbol{k}\cdot\boldsymbol{r}) - \omega t\}\ , \tag{134}$$

where $\boldsymbol{E}$ and $\boldsymbol{H}$ are the electric and magnetic vectors of the wave, ω and $\boldsymbol{k}$ are its frequency and wave vector, and $\boldsymbol{r}$ and t denote the spatial coordinates and time, respectively. The wavelength $\lambda = 2\pi/k$ is assumed to be considerably larger than the size of the particle, so the metal particle resides actually in spatially uniform, but time-varying, electric and magnetic fields. The external electric field $\boldsymbol{E}^{(0)}\mathrm{e}^{-\mathrm{i}\omega t}$ induces a local potential electric field $\boldsymbol{E}_{\mathrm{loc}}$ inside the particle, which in turn gives rise to electric current with the density $\boldsymbol{j}_{\mathrm{e}}$. The magnetic field $\boldsymbol{H}^{(0)}\mathrm{e}^{-\mathrm{i}\omega t}$ induces in the particle a vortex (eddy) electric field $\boldsymbol{E}_{\mathrm{ed}}$, which gives rise to an eddy electric current with the density $\boldsymbol{j}_{\mathrm{m}}$.

As a result, the total dissipation of the wave energy, i.e. absorption by the particle, is

$$W = W_{\mathrm{e}} + W_{\mathrm{m}} = \frac{1}{2}\mathrm{Re}\int_V \mathrm{d}\boldsymbol{r}\,(j_{\mathrm{e}}\cdot\boldsymbol{E}^{*}_{\mathrm{loc}} + \boldsymbol{j}_{\mathrm{m}}\cdot\boldsymbol{E}^{*}_{\mathrm{ed}})\,, \tag{135}$$

where V is the particle volume.

The first term in Eq. (135) corresponds to electric absorption and the second to magnetic absorption. To calculate the total absorption, it is necessary to find the potential electric field $\boldsymbol{E}_{\mathrm{loc}}$, the eddy electric field $\boldsymbol{E}_{\mathrm{ed}}$, and the corresponding current densities $\boldsymbol{j}_{\mathrm{e}}$ and $\boldsymbol{j}_{\mathrm{m}}$. For spherical particles that are either larger or smaller than the electron mean free path, the formulas determining simultaneous electric and magnetic absorptions were obtained earlier (see, e.g., [185]). The total energy absorbed by a spherical particle is

$$W = \frac{9}{8\pi}V\omega\varepsilon''\left[\frac{1}{(2+\varepsilon')+\varepsilon''} + \frac{\omega^2R^2}{90c^2}\right]|\boldsymbol{E}^{(0)}|^2\,, \tag{136}$$

where ε' and ε'' are, respectively, the real and imaginary parts of the dielectric constant, R is the particle radius, and c is the speed of light. The first term in Eq. (136) describes electric absorption and the second term magnetic absorption.

For the particle larger than the mean free path, the bulk scattering is dominant and the dielectric constant of the metal has its standard form

$$\varepsilon_0 = \varepsilon' + \mathrm{i}\varepsilon'' = 1 - \frac{\omega_{\mathrm{p}}^2}{\omega^2+\nu^2} + \mathrm{i}\frac{\nu}{\omega}\,\frac{\omega_{\mathrm{p}}^2}{\omega^2+\nu^2}\,, \tag{137}$$

ω_{p} being the plasma frequency and ν the collision rate.

Eqs. (136) and (137) can be used to estimate the relative contributions of electric and magnetic absorption to the total absorption. For instance, for a gold particle one has $\omega_{\mathrm{p}} \approx 5\times10^{15}\,\mathrm{s}^{-1}$ and $\nu \approx 10^{13}\,\mathrm{s}^{-1}$. Assume that $R = 3\times10^{-6}\,\mathrm{cm}$ and that ω is the frequency of a CO_2 laser, i.e., $\omega \approx 2\times10^{14}\,\mathrm{s}^{-1}$. Then Eq. (136) yields $\varepsilon' \approx -600$ and $\varepsilon'' \approx 30$, and the magnetic-to-electric absorption ratio is

$$\frac{W_{\mathrm{m}}}{W_{\mathrm{e}}} = \frac{1}{90}\left(\frac{\omega R}{c}\right)^2|\varepsilon_0|^2 \approx 2\,. \tag{138}$$

Thus, for the given set of parameters magnetic absorption is twice as large as electric. Obviously, for different parameters of the particle and a different frequency range electric absorption can be either larger or smaller than magnetic absorption. Hence, when studying the shape dependence of

optical absorption by a small metal particle, we must take into account both electric and magnetic absorption. To our knowledge, the total absorbed power for asymmetric particles smaller than the mean free path was first calculated in [177,178]. The only quantity studied earlier had been the light-induced conductivity $\sigma(\omega)$, defined by

$$\boldsymbol{j}_{\mathrm{e}} = \sigma \boldsymbol{E}_{\mathrm{loc}} \ , \tag{139}$$

for spherical [170] and cylindrical [179] particles, and for particles shaped like parallelepipeds [180]. All these works use a quantum mechanical approach, and the shape of the particles is chosen in such a way that the Schoedinger equation can be solved analytically for the potential well corresponding to such a symmetry.

For particles larger than the mean free path, the light-induced conductivity is known ($\sigma = \omega\varepsilon''/4\pi$), and the calculation of the effect of particle shape on absorption reduces to finding $\boldsymbol{E}_{\mathrm{loc}}$ and $\boldsymbol{E}_{\mathrm{ed}}$. The local electric field in the case of an ellipsoidal particle is independent of the coordinates and can easily be expressed in terms of the components of the depolarization tensor. This feature has been used to consider the dependence of electric absorption on the particle shape in the case where bulk scattering is dominant (see, e.g., Ref. [165] and references therein).

For perfect conductivity $\varepsilon'' \gg |\varepsilon'|$, magnetic absorption by ellipsoidal metallic particles larger than the electron mean free path was calculated by Levin and Muratov [186].

In most theoretical works treating optical absorption by island metal films, attention is focused on the effect of the interaction between the metallic particles on $\boldsymbol{E}_{\mathrm{loc}}$ and hence on electric absorption (see, e.g., Ref. [187] and references therein). In some cases, this interaction can indeed lead to a significant change in the absorbed power [188]. However, the effect of particle shape on electric and magnetic absorption, and the polarization dependence of the electric-to-magnetic absorption ratio have not been studied. Meanwhile, these factors can change the absorbed power in the IR region not just severalfold, but by several orders of magnitude.

7.3. Local fields

In what follows we shall examine ellipsoidal metal particles. Such an assumption has several advantages. First, by considering ellipsoids of different oblateness and elongation, one can simulate the majority of real particle shapes (from "pancake" to needle-like). Second, the potential ($\boldsymbol{E}_{\mathrm{loc}}$) and eddy ($\boldsymbol{E}_{\mathrm{ed}}$) local fields for such particles can easily be calculated.

For ellipsoidal particles, the potential local electric field $\boldsymbol{E}_{\mathrm{loc}}$ induced by a uniform external electric field $\boldsymbol{E}^{(0)}$ is known to be coordinate-independent [185]. The field $\boldsymbol{E}_{\mathrm{loc}}$ can be linearly expressed in terms of $\boldsymbol{E}^{(0)}$ by employing the depolarization tensor. In terms of the principal axes of the depolarization tensor, which coincide with the principal axes of the ellipsoid, one has

$$(E_{\mathrm{loc}})_j = E_j^{(0)} - 4\pi L_j P_j = E_j^{(0)} - L_j(\varepsilon - 1)(E_{\mathrm{loc}})_j \ , \tag{140}$$

Here L_j are the principal values of the components of the depolarization tensor, and $\boldsymbol{P}$ is the polarization vector.

As we shall see below, the light-induced conductivity becomes a tensor for asymmetric particles smaller than the mean free path, so Eq. (140) needs to be modified.

This will be done somewhat later. It should also be noted that in the case of a particle ensemble, the polarization vector in a given particle is induced not only by the external field, but also by the

dipoles induced by this field in other particles [126,189]. Here we neglect such effects, but they can easily be incorporated into the picture [188]. Calculating $(E_{\rm loc})_j$ from (140), we get

$$|(E_{\rm loc})_j|^2 = \frac{(E_j^{(0)})^2}{[1 + L_j(\varepsilon' - 1)]^2 + (L_j\varepsilon'')^2} \ . \tag{141}$$

When the light-induced conductivity of the small particles becomes a tensor (we consider this case later), we must substitute $4\pi\sigma_{ll}/\omega$ for ε'' in Eq. (141) (σ_{jj} is the jth diagonal component of the light-induced conductivity tensor).

Let us now find the eddy local field $\boldsymbol{E}_{\rm ed}$ which obeys Maxwell's equations

$$\begin{aligned} &\nabla \times \boldsymbol{E}_{\rm ed} = -\mathrm{i}\frac{\omega}{c}\boldsymbol{H}^{(0)} \ , \\ &\nabla \times \boldsymbol{E}_{\rm ed} = 0 \ , \end{aligned} \tag{142}$$

augmented by the boundary condition

$$\boldsymbol{E}_{\rm ed} \cdot \boldsymbol{n}_{\rm s}|_S = 0 \ , \tag{143}$$

where $\boldsymbol{n}_{\rm s}$ is a unit vector normal to the surface S.

Here the following remark is in order. On the right-hand side of the first equation in (142), we take the external (spatially uniform) magnetic field $\boldsymbol{H}^{(0)}$ for the magnetic field inside the particle. Such an approximation is justified if the depth δ_H of the skin layer is much larger than the characteristic particle size R:

$$\delta_H \equiv (\omega/c\,\mathrm{Im}\sqrt{\varepsilon})^{-1} \gg R \ .$$

For an ellipsoidal particle, R is the semimajor axis of the ellipsoid. Below we assume that the inequality is fulfilled. This constitutes the most interesting case since the contribution of eddy currents to absorption is then at its maximum. Keeping in mind that $H^{(0)}$ is constant, we can write the solution of the system of Eqs. (142) as

$$(E_{\rm ed})_j = \sum_{k=1}^{3} \alpha_{jk} x_k, \quad (x_1 = x,\ x_2 = y,\ x_3 = z) \tag{144}$$

and uniquely determine the set of constants α_{ij} from the system (142) and the boundary condition (143). The result is

$$(E_{\rm ed})_x = \frac{\mathrm{i}\omega}{c}\left(\frac{zH_y^{(0)}}{R_z^2 + R_x^2} - \frac{yH_z^{(0)}}{R_x^2 + R_y^2}\right)R_x^2 \ . \tag{145}$$

The other components of $E_{\rm ed}$ can be obtained via cyclic permutations. In Eq. (145), R_x, R_y, and R_z are the semi-axes of the ellipsoid.

Knowing $\boldsymbol{E}_{\rm loc}$ and $\boldsymbol{E}_{\rm ed}$ for particles whose characteristic size is larger than the electron mean free path, it is easy to derive from Eq. (135) a formula for the absorbed power. Note that in this case the currents are related to the field through relationships of type (139).

If for the sake of simplicity we consider an ellipsoid of revolution (with the z-axis chosen as the axis of revolution), then combining (135), (141), (145), and (139) we get

$$W = V\frac{\omega\varepsilon'}{8\pi}\left\{\sum\frac{(E_j^{(0)})^2}{[1 + L_j(\varepsilon' - 1)]^2 + (L_j\varepsilon'')^2} + \frac{\omega^2 R_\perp^2}{10c^2}(H_\parallel^{(0)})^2 + \frac{\omega^2}{5c^2}\,\frac{R_\perp^2 R_\parallel^2}{R_\perp^2 + R_\parallel^2}(H_\perp^{(0)})^2\right\}, \tag{146}$$

where $H_{\|}^{(0)} = H_z^{(0)}$, $H_{\perp}^{(0)} = \sqrt{(H_x^{(0)})^2 + (H_y^{(0)})^2}$,

$$R_x = R_y = R_{\perp}, \quad R_z = R_{\|} \ .$$

Eq. (146) generalizes formula (136) to the case of ellipsoidal particles. Note that in (146) $E^{(0)} = H^{(0)}$, and we do not express $H^{(0)}$ in terms of $E^{(0)}$ (as we did in (136)), so that the dependence of the absorbed power on wave polarization can be more graphic. The principal values of the components of the depolarization tensor for particles which are ellipsoids of revolution read

$$L_x = L_y = \tfrac{1}{2}(1 - L_z) \ ,$$

$$L_z = \begin{cases} \dfrac{1 - e_p^2}{2e_p^3}\left[\ln\dfrac{1 + e_p}{1 - e_p} - 2e_p\right], & R_{\|} > R_{\perp} \ , \\ \dfrac{1 + e_p^2}{e_p^3}[e_p - \arctan\, e_p], & R_{\|} < R_{\perp} \ , \end{cases} \tag{147}$$

where $e_p^2 = |1 - R_{\perp}^2/R_{\|}^2|$.

Fig. 7.1 shows L_z as a function of the ellipsoid semi-axis ratio $R_{\perp}/R_{\|}$. The components L_j of the depolarization tensor can vary between zero and unity. The denominator in (141) is seen to contain L_j^2 as a cofactor of $(\varepsilon' - 1)^2$. As follows from the above estimates, one has $\varepsilon'^2 \approx 4 \times 10^4$ in the frequency range of a CO_2 laser. Consequently, $|\boldsymbol{E}_{\rm loc}|^2$can strongly depend on particle shape. Fig. 7.2 depicts the dependence of $|\boldsymbol{E}_{\rm loc}|^2/|\boldsymbol{E}^{(0)}|^2$ on the semi-axis ratio $R_{\perp}/R_{\|}$ for the case where $E^{(0)}$ is directed along the axis of revolution. It is seen that the ratio of the square of the local field to the square of the external field can vary by several orders of magnitude. According to (146), this means that electric absorption by metallic particles can vary by several orders of magnitude, depending on particle shape and wave polarization.

This fact entails important consequences. As we noted earlier (see Sections 3 and 5), the electron gas of the metal particles heats up when an island metal film is illuminated by laser light. This leads

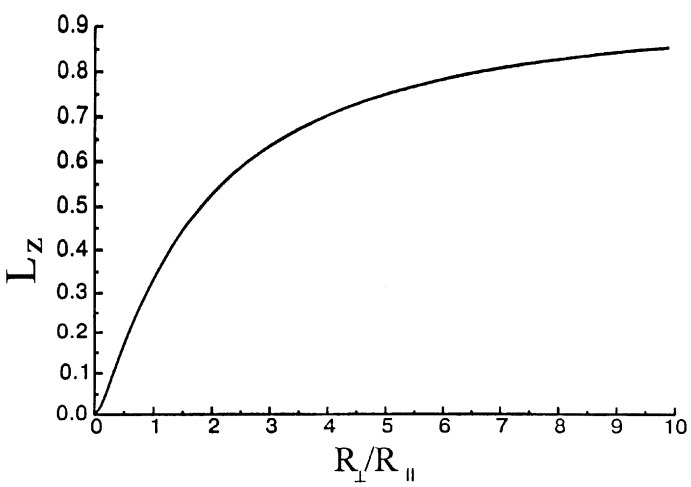

Fig. 7.1. Dependence of the factor of depolarization along the ellipsoid's axis of revolution on the ellipsoid's semiaxis ratio.

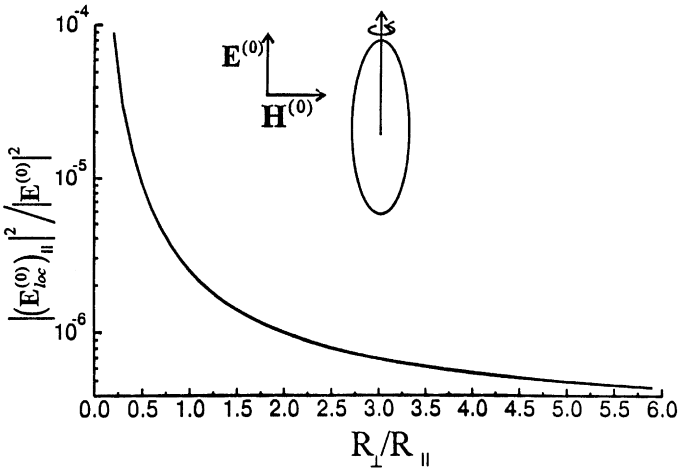

Fig. 7.2. Dependence of the ratio of the square of the local electric field inside the particle to the square of the wave's electric field on the ellipsoid's semiaxis ratio for the chosen wave polarization.

to electron and photon emission. In particular, electron emission is here actually thermionic and, according to Richardson's law, is proportional to $\exp\{-\varphi/kT_e\}$, where φ is the work function and T_e is the electron temperature. The electron temperature T_e is determined by the energy absorbed by a particle, which in turn is strongly dependent on particle shape and wave polarization. In this situation, introducing average (effective) absorption cross sections makes no sense. It is just the particles absorbing the most light that are the emitters of electrons. In other words, these phenomena are determined primarily by particles with maximum absorption and not by particles with some average ("effective") absorption, which constitute the majority in an island film.

7.4. Electron distribution function

In Section 7.3 we determined the local fields and derived a general expression for the power absorbed by an ellipsoidal metal particle in the case of bulk scattering (i.e., for particles larger than the mean free path). Here we address the case of particles smaller than the mean free path. The more general method we now develop can also be applied to particles larger than the mean free path.

To determine the absorbed power, it is necessary to derive expressions for the high-frequency currents induced in the particle by the known local potential and eddy electric fields. By definition, the current density is

$$\boldsymbol{j} = \frac{2e}{(2\pi\hbar)^3}\int \boldsymbol{v} f \,\mathrm{d}^3(m\boldsymbol{v}) = \frac{2m^3 e}{(2\pi\hbar)^3}\int \boldsymbol{v} f(\boldsymbol{v})\,\mathrm{d}^3 v\ , \tag{148}$$

where $f(\boldsymbol{v})$ is the electron velocity distribution function, and e and m are electron charge and mass. In the presence of local fields, the distribution function can be represented as a sum of two terms,

$$f(\boldsymbol{v}) = f_0(\varepsilon) + f_1(\boldsymbol{v})\ ,$$

where $f_0(\varepsilon)$ is the Fermi distribution function, depending only on energy $\varepsilon = mv^2/2$, and $f_1(\boldsymbol{v})$ is a correction generated by the local fields. $f_1(\boldsymbol{v})$ can be found by solving the appropriate kinetic equation. In the linear approximation, the kinetic equation in the electromagnetic field assumes the form

$$(\nu - \mathrm{i}\omega)f_1 + \boldsymbol{v}\cdot\frac{\partial f_1}{\partial r} + e\boldsymbol{F}\cdot\boldsymbol{v}\frac{\partial f_0}{\partial \varepsilon} = 0 \ . \tag{149}$$

Here we have taken into account that $f_1 \propto \mathrm{e}^{\mathrm{i}\omega t}$; ν is the bulk collision rate and

$$\boldsymbol{F} = \boldsymbol{E}_{\mathrm{loc}}^{(0)} + \boldsymbol{E}_{\mathrm{ed}}^{(0)} \ . \tag{150}$$

Eq. (149) must be augmented by boundary conditions for f_1. We assume, as is often done, the electron scattering at the boundary to be diffuse, i.e.,

$$f_1(\boldsymbol{r},\boldsymbol{v})|_S = 0 \quad \text{for } v_n < 0 \ , \tag{151}$$

where v_n is the velocity component normal to the surface S.

Based upon these assumptions, Lesskin et al. [190] studied the magnetic scattering by a spherical metal particle. To solve Eq. (149) with the boundary conditions (151), we employ the method of characteristic curves, which demonstrated its effectiveness in Ref. [190]. However, for ellipsoidal particles the method used in Ref. [190] needs to be modified. The essence of this modification is as follows.

We transform to a deformed system of coordinates in which the original ellipsoid particle,

$$\sum_{i=1}^{3}\frac{x_i^2}{R_i^2} = 1 \tag{152}$$

becomes a sphere of radius R. In other words, we assume that

$$x_i = x_i'/\gamma_i, \quad \gamma_i = R/R_i, \quad R = (R_1R_2R_3)^{1/3}, \quad \gamma_1\gamma_2\gamma_3 = 1 \ . \tag{153}$$

Under such a deformation the shape of the particle changes, but its volume is conserved. This means that the electron number density remains unchanged, and so does the normalization of the function f.

In the new system of coordinates, Eq. (149) and the boundary conditions (151) acquire the form

$$(\nu - \mathrm{i}\omega)f_1 + \boldsymbol{v}'\cdot\frac{\partial f_1}{\partial \boldsymbol{r}'} + e\boldsymbol{F}(r')\cdot\boldsymbol{v}\frac{\partial f_0}{\partial \varepsilon} = 0 \ , \tag{154}$$

$$f_1(\boldsymbol{r}',\boldsymbol{v}')|_{r'=R} = 0 \quad \textit{for } \boldsymbol{r}'\cdot\boldsymbol{v}' < 0 \ . \tag{155}$$

In (154) and (155) we also introduced the "deformed" velocity components

$$v_i' = \gamma_i v_i \ . \tag{156}$$

Eq. (154) for the characteristic curves has the form

$$\mathrm{d}x_i'/v_i' = -\mathrm{d}f_1/\tilde{\nu}f_1 = \mathrm{d}t', \quad \tilde{\nu} \equiv \nu - \mathrm{i}\omega \ , \tag{157}$$

which implies that

$$\boldsymbol{r}' = \boldsymbol{v}'t' + \boldsymbol{R} \ , \tag{158}$$

where $\boldsymbol{R}$ is the radius vector whose tip is at the given point of the sphere from which the trajectory begins. Here the parameter t' can formally be considered as the "time" of motion of the electron along the trajectory.

If we transfer $v't'$ in (158) to the left-hand side and square the resulting equation, the solution of this new (scalar) equation can be written as

$$t' = \frac{1}{v'^2}[\boldsymbol{r}' \cdot \boldsymbol{v}' + \sqrt{(R^2 - r'^2)v'^2 + (\boldsymbol{r}' \cdot \boldsymbol{v}')^2}] \ . \tag{159}$$

The characteristic curve (159) depends only on the absolute value of R and not on the orientation of $\boldsymbol{R}$. Such independence of the characteristic curve from the position of a point on the surface was achieved by transforming to the coordinates (153).

From (159) we also see that $t' = 0$ at $r' = R$. Bearing this in mind, we can use (157) to find an f_1 that satisfies Eq. (154) and the boundary condition (155):

$$f_1 = -\frac{\partial f_0}{\partial \varepsilon} \int_0^t \mathrm{d}\tau \exp\{-\tilde{\nu}(t' - \tau)\} e\boldsymbol{v} \cdot \boldsymbol{F}(\boldsymbol{r}' - \boldsymbol{v}'(t' - \tau)) \ . \tag{160}$$

Taking into account the coordinate dependence of $\boldsymbol{F}$ (see (150) and (145)), from (160) we obtain

$$f_1 = -e\frac{\partial f_0}{\partial \varepsilon} \left\{ \boldsymbol{v} \cdot \boldsymbol{E}_{\mathrm{loc}}^{(0)} + \sum_{i,j=1}^{3} \alpha_{ij} v_i \left[\frac{x_j'}{\gamma_j} + v_j \frac{\partial}{\partial \tilde{\nu}} \right] \right\} \frac{1 - \exp\{-\tilde{\nu}t'\}}{\tilde{\nu}} \ . \tag{161}$$

If initially the particle is spherical, then $\alpha_{ij} = -\alpha_{ji}$ and the last term in (161) vanishes.

7.5. Electric absorption

Combining (161), (148), and (135), we obtain the following expression for the electric absorption:

$$W_{\mathrm{e}} = \frac{e^2 m^3}{(2\pi\hbar)^3} \mathrm{Re} \left[\frac{1}{\tilde{\nu}} \int |\boldsymbol{v} \cdot \boldsymbol{E}_{\mathrm{loc}}^{(0)}|^2 \delta(\varepsilon - \mu)(1 - \exp\{-\tilde{\nu}t'\}) \, \mathrm{d}^3 r' \, \mathrm{d}^3 v \right] , \tag{162}$$

where μ is the Fermi energy, and where we considered the fact that

$$\partial f_{\mathrm{o}} / \partial \varepsilon = -\delta(\varepsilon - \mu) \ .$$

Allowing for the form of t' (according to (159)), it is convenient to integrate (162) with respect to $\boldsymbol{r}'$ by directing the z'-axis along the vector $\boldsymbol{v}'$ and introducing two new variables,

$$\zeta = \frac{r'}{R}, \quad \eta = \frac{v'}{R} t' \ . \tag{163}$$

The result reads

$$\int(1-\exp\{\tilde{\nu}t'\})\,\mathrm{d}^3r' = 2\pi\int_0^R \mathrm{d}r'\,r'^2\int_0^\pi \mathrm{d}\theta\sin\theta(1-\exp\{-\tilde{\nu}t'\})$$
$$= 2\pi R^3\int_0^1 \mathrm{d}\zeta\,\zeta^2\int_{1-\zeta}^{1+\zeta}\mathrm{d}\eta\,\frac{\eta^2-\zeta^2+1}{2\eta^2\zeta}\left(1-\exp\left\{-\frac{\tilde{\nu}R\eta}{v'}\right\}\right)$$
$$= \pi R^3\int_0^2\frac{\mathrm{d}\eta}{\eta^2}\left(1-\exp\left\{-\frac{\tilde{\nu}R\eta}{v'}\right\}\right)\int_{|\eta-1|}^1 \mathrm{d}\zeta\,\zeta(\eta^2-\zeta^2+1)\,.$$

Further calculation of the integral is easy, and as a result from (162) we obtain

$$W_\mathrm{e} = \frac{\pi e^2m^3R^3}{(2\pi\hbar)^3}\mathrm{Re}\left[\frac{1}{\tilde{\nu}}\int \mathrm{d}^3v\,|\boldsymbol{v}\cdot\boldsymbol{E}^{(0)}_\mathrm{loc}|^2\delta(\varepsilon-\mu)\psi(q)\right], \tag{164}$$

where we have introduced

$$\psi(q) = \frac{4}{3}-\frac{2}{q}+\frac{4}{q^3}-\frac{4}{q^2}\left(1+\frac{1}{q}\right)\exp\{-q\}\,,$$
$$q \equiv q_1 - \mathrm{i}q_2 = \frac{2\nu}{v'}R - \mathrm{i}\frac{2\omega}{v'}R\,. \tag{165}$$

Eq. (164) gives the general form of the electric absorption by an ellipsoidal metal particle for an arbitrary bulk-to-surface scattering ratio.

The above case of bulk scattering (the Drude case) follows from (164) when $q \gg 1$. Then, according to (165), $\psi(q) = 4/3$, and from Eq. (164) we obtain for the electric absorption

$$W_\mathrm{e} \approx V\frac{e^2n}{m}\,\frac{\nu}{\nu^2+\omega^2}\,\frac{|\boldsymbol{E}^{(0)}_\mathrm{loc}|^2}{2} \equiv V\sigma(\omega)\,\frac{|\boldsymbol{E}^{(0)}_\mathrm{loc}|^2}{2}\,, \tag{166}$$

where n is the electron concentration, which can be expressed in terms of the Fermi velocity v_F or the Fermi energy μ:

$$n = \frac{8\pi}{3}\,\frac{(mv_\mathrm{F})^3}{(2\pi\hbar)^3}, \quad v_\mathrm{F} = \sqrt{\frac{2\mu}{m}}\,. \tag{167}$$

Obviously, Eq. (166) corresponds to the first term in (146).

We now analyze the situation when the particle is smaller than the mean free path, and hence surface scattering is dominant. This corresponds to

$$q_1 = (2\nu/v')R \ll 1\,. \tag{168}$$

As for $q_2 \equiv 2\omega R/v'$, when surface scattering is dominant, this parameter can be either larger or smaller than unity. It is of interest then to study the two limits

$$q_2 = (2\omega/v')R \gg 1\,, \tag{169}$$
$$q_2 \ll 1\,. \tag{170}$$

The case (169) corresponds to high-frequency surface scattering, and (170) to low-frequency surface scattering.

If we ignore bulk scattering ($q_1 \to 0$) and assume that q_2 is arbitrary, then (165) yields

$$\mathrm{Re}\left[\frac{1}{\tilde{v}}\psi(q)\right] \approx \frac{1}{\omega}\left[\frac{2}{q_2} - \frac{4}{q_2^2}\sin q_2 + \frac{4}{q^3}(1-\cos q_2)\right]. \tag{171}$$

This expression is present in (164). We see that terms which are oscillating functions of particle size have emerged. Such oscillation effects in spherical particles were studied by Austin and Wilkinson [191] for electric absorption, and by Lesskin et al. [190] for magnetic absorption. These effects, which are moderate by themselves, are even less important for asymmetric particles. The reason is that the "deformed" velocity v', which enters into the expression for q_2, is angle-dependent. In view of this, the integration over angles smooths out the oscillation effects. Furthermore, Eq. (171) implies that these oscillations can be essential only when $q_2 = 2R\omega/v' \approx 1$, i.e., when the electron transit time from wall to wall, $2R/v'$, coincides with the period of the electromagnetic wave. In the limiting cases given by (170), these effects are negligible.

Let us turn to the high-frequency case (169). For $q_2 \gg 1$ and $q_1 \ll 1$ we have

$$\mathrm{Re}\left[\frac{1}{\tilde{v}\psi(q)}\right] \approx \frac{2}{\omega q_2},$$

which in accordance with (164) gives

$$W_e \approx \frac{\pi e^2 m^3 R^2}{(2\pi\hbar)^3\omega^2}\int \mathrm{d}^3v\, v'|\boldsymbol{v}\cdot\boldsymbol{E}^{(0)}_{\mathrm{loc}}|^2\delta(\varepsilon-\mu). \tag{172}$$

To study the dependence of absorption on particle shape, it is sufficient to consider an ellipsoid of revolution. In this case

$$v' = R\sqrt{\frac{v_\perp^2}{R_\perp^2} + \frac{v_\parallel^2}{R_\parallel^2}}, \tag{173}$$

where $v_\perp$ and $v_\parallel$ are the electron velocity components perpendicular and parallel to the axis of revolution. With allowance for (173), the integral in (172) can easily be calculated:

$$W_e = V\frac{ne^2}{m\omega^2}\frac{v_F}{R_\perp}\frac{9}{16}[\varphi_\perp|E^{(0)}_{\perp,\mathrm{loc}}|^2 + \varphi_\parallel|E^{(0)}_{\parallel,\mathrm{loc}}|^2]. \tag{174}$$

Here $\varphi_\perp$ and $\varphi_\parallel$ are functions of the ellipsoid eccentricity (we note once more that $e_p^2 = |1 - R_\perp^2/R_\parallel^2|$):

$$\varphi_\perp = \frac{1}{2}\begin{cases} \frac{1}{2}\left(1+\frac{1}{2e_p^2}\right)\sqrt{1-e_p^2} + \frac{1}{e_p}\left(1-\frac{1}{4e_p^2}\right)\arcsin e_p, & R_\perp < R_\parallel, \\ \frac{1}{2}\left(1-\frac{1}{2e_p^2}\right)\sqrt{1+e_p^2} + \frac{1}{e_p}\left(1+\frac{1}{4e_p^2}\right)\ln(\sqrt{1+e_p^2}+e_p), & R_\perp > R_\parallel, \end{cases} \tag{175}$$

$$\varphi_{\parallel} = \begin{cases} \dfrac{1}{2}\left(1 - \dfrac{1}{2e_p^2}\right)\sqrt{1-e_p^2} + \dfrac{1}{4e_p^3}\arcsin e_p, \; R_{\perp} < R_{\parallel} \; , \\ \dfrac{1}{2}\left(1 + \dfrac{1}{2e_p^2}\right)\sqrt{1+e_p^2} - \dfrac{1}{4e_p^3}\ln(\sqrt{1+e_p^2} + e_p) \; , \\ \\ R_{\perp} > R_{\parallel} \; . \end{cases} \tag{176}$$

Having the general expression (174) for the electric absorption of an ellipsoidal metal particle in the case of high-frequency scattering, we can easily obtain the components of the light-induced conductivity tensor. To this end, we write the expression for electric absorption in terms of the principal values σ_{jj} of the conductivity tensor,

$$W_{\mathrm{e}} = V\frac{1}{2}\sum_{j=1}^{3} \sigma_{jj}|E_{j,\mathrm{loc}}^{(0)}|^2 \; , \tag{177}$$

and compare it with (174). As a result we have

$$\begin{aligned} \sigma_{xx} = \sigma_{yy} \equiv \sigma_{\perp} &= \frac{ne^2}{m\omega^2}\,\frac{v_{\mathrm{F}}}{R_{\perp}}\,\frac{9}{8}\varphi_{\perp} \; , \\ \sigma_{zz} = \sigma_{\parallel} &= \frac{ne^2}{m\omega^2}\,\frac{v_{\mathrm{F}}}{R_{\perp}}\,\frac{9}{8}\varphi_{\parallel} \; . \end{aligned} \tag{178}$$

The case of a spherical particle follows from (174)–(177) as $e_p \to 0$.
Allowing for (175) and (179), we find that

$$\sigma_{\perp} = \sigma_{\parallel} = \frac{ne^2}{m\omega^2}\,\frac{3}{4}\,\frac{v_{\mathrm{F}}}{R} \; . \tag{179}$$

Comparing (178) and (179), we can see that the light-induced conductivity of metallic particles smaller than the mean free path is a scalar quantity only if the particles are symmetric.

In the general case of asymmetric particles, the light-induced conductivity becomes a tensor whose components depend on particle shape. Fig. 7.3 illustrates the dependence of $\sigma_{\perp}/\sigma_{\parallel}$ on the ellipsoid semiaxis ratio $R_{\perp}/R_{\parallel}$. Eq. (178) was used to plot the curves. We see that the components of the light-induced conductivity tensor differ considerably, depending on the degree of particle asymmetry.

Comparing (179) with the expression for the conductivity that follows from (166) for $\omega \gg v$, we can see that in the case of a spherical particle, the expression for the electrical conductivity dominated by surface scattering can be obtained from a similar expression for the Drude case by formally substituting $3v_{\mathrm{F}}/4R$ for v. This method is widely used, but in the case of asymmetric particles this procedure leads to incorrect results. The appearance in (174) of the factor $v_{\mathrm{F}}/R_{\perp}$, which has the formal meaning of "transit frequency", is due to the fact that the particle volume V can be expressed as a separate factor. But when surface scattering dominates, the absorbed power is proportional to the surface area of the particle. This can easily be seen by using (174)–(176) to derive simple analytic expressions for highly elongated and highly flattened

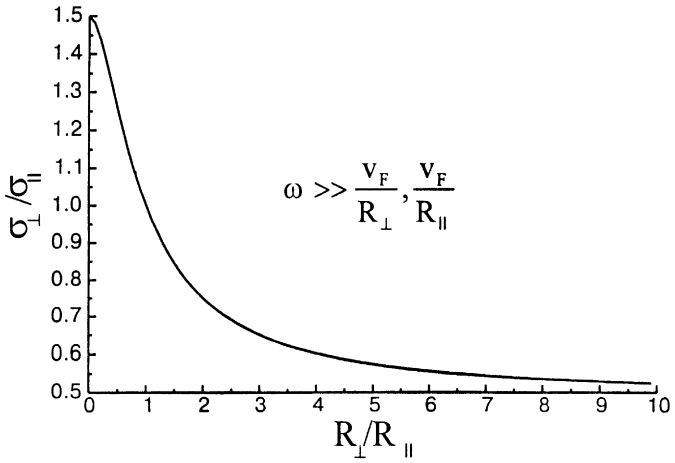

Fig. 7.3. Dependence of the ratio of conductivity normal to the ellipsoid's axis of revolution ($\sigma_\perp$) to conductivity parallel to this axis ($\sigma_\parallel$) on the ellipsoid's semiaxis ratio in the case $\omega \ll v_F/R_\perp, v_F/R_\parallel$.

ellipsoids:

$$W_e \approx \frac{9\pi}{128} V \frac{ne^2}{m\omega^2} \frac{v_F}{R_\perp} \left(\frac{3}{2} |(E_{loc}^{(0)})_\perp|^2 + |(E_{loc}^{(0)})_\parallel|^2 \right), \quad \boldsymbol{R}_\perp \ll \boldsymbol{R}_\parallel , \tag{180}$$

$$W_e \approx \frac{9}{32} V \frac{ne^2}{m\omega^2} \frac{v_F}{R_\parallel} \left(\frac{1}{2} |(E_{loc}^{(0)})_\perp|^2 + |(E_{loc}^{(0)})_\parallel|^2 \right), \quad \boldsymbol{R}_\perp \gg \boldsymbol{R}_\parallel . \tag{181}$$

The factors $V/R_\perp \approx R_\parallel R_\perp$ in (180) and $V/R_\parallel \approx R_\perp^2$ in (181) are simply the surface areas of the corresponding ellipsoids in the specified limits.

The fact that absorption by small spherical particles is proportional to their surface area was reported earlier in [170,174].

Let us now examine the case (170) of low-frequency surface scattering, i.e.,

$$q_1 \ll q_2 \ll 1 . \tag{182}$$

Here the frequency of the electromagnetic wave is much higher than the bulk collision rate, but is much lower than the frequency of transit from wall to wall. If condition (182) is satisfied, we have $\psi(q) \approx q/2$, and from (164) we obtain

$$W_e \approx \frac{\pi e^2 m^3 R^4}{(2\pi\hbar)^3} \int \frac{d^3 v}{v'} |\boldsymbol{v} \cdot \boldsymbol{E}_{loc}^{(0)}|^2 \delta(\varepsilon - \mu) . \tag{183}$$

After evaluating the integral in (183) we can transform the result to (177), where instead of (178) we will have

$$\sigma_\perp = \frac{9}{8}\frac{ne^2}{m}\frac{R_\perp}{v_F}\begin{cases} -\dfrac{1}{2e_p^2}\sqrt{1+e_p^2}+\dfrac{1}{e_p}\left(1+\dfrac{1}{2e_p^2}\right)\ln(\sqrt{1+e_p^2}+e_p)\,, \\ R_\perp > R_\parallel\ , \\ \dfrac{1}{2e_p^2}\sqrt{1-e_p^2}+\dfrac{1}{e_p}\left(1-\dfrac{1}{2e_p^2}\right)\arcsin e_p\ , \\ R_\perp < R_\parallel\ , \end{cases} \tag{184}$$

$$\sigma_\parallel = \frac{ne^2}{m}\frac{R_\perp}{v_F}\begin{cases} \dfrac{1}{e_p^2}\sqrt{1+e_p^2}-\dfrac{1}{e_p^3}\ln(\sqrt{1+e_p^2}+e_p)\ , \\ R_\perp > R_\parallel\ , \\ -\dfrac{1}{e_p^2}\sqrt{1-e_p^2}+\dfrac{1}{e_p^2}\arcsin e_p, \quad R_\perp < R_\parallel\ . \end{cases} \tag{185}$$

Formula (183) for the absorbed power assumes a simple analytic form for the limits of highly flattened and highly elongated ellipsoids:

$$W_e \approx \frac{9}{16}V\frac{ne^2}{m}\frac{R_\parallel}{v_F}\left\{\left[\ln\left(2\frac{R_\perp}{R_\parallel}\right)-\frac{1}{2}\right]|E^{(0)}_{\perp,\mathrm{loc}}|^2+|E^{(0)}_{\parallel,\mathrm{loc}}|^2\right\}, \quad R_\perp \gg R_\parallel\ , \tag{186}$$

$$W_e \approx V\frac{ne^2}{m}\frac{R_\perp}{v_F}\left(\frac{1}{2}|E^{(0)}_{\perp,\mathrm{loc}}|^2+|E^{(0)}_{\parallel,\mathrm{loc}}|^2\right), \quad R_\perp \ll R_\parallel\ . \tag{187}$$

In addition, at $R_\perp = R_\parallel$, Eq. (183) yields the well-known result for a spherical particle:

$$W_e \approx \frac{3}{8}V\frac{ne^2}{m}\frac{R}{v_F}|E^{(0)}_{\mathrm{loc}}|^2\ . \tag{188}$$

Fig. 7.4 depicts the dependence of $\sigma_\perp/\sigma_\parallel$ on the ellipsoid's semiaxis ratio $R_\perp/R_\parallel$ constructed from Eqs. (184) and (185). Comparing Figs. 7.3 and 7.4, we see that the effect of particle asymmetry on the ratio of the components of the conductivity tensor differs not only quantitatively, but also qualitatively in the high- and low-frequency cases (provided that surface scattering is dominant).

7.6. Magnetic absorption

Magnetic absorption is given by the second term in (135). Combining (144), (148) and (161), we obtain an expression for it:

$$W_m = \frac{e^2m^3}{(2\pi\hbar)^3}\mathrm{Re}\int \mathrm{d}^3r'\,\mathrm{d}^3v\;\delta(\varepsilon-\mu)\sum_{(1)}^{(3)}\frac{\alpha^*_{lk}\alpha_{ij}}{\gamma_l\gamma_k\gamma_i\gamma_j}v'_lx'_kv'_ix'_j\frac{1-\exp\{-\tilde{\nu}t'\}}{\tilde{\nu}}\ , \tag{189}$$

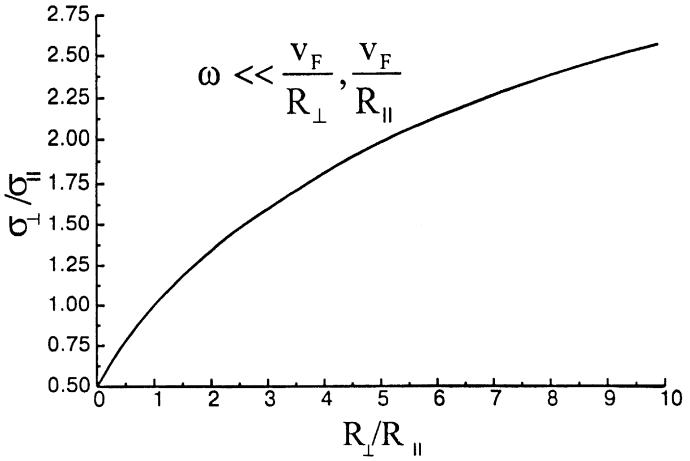

Fig. 7.4. Dependence of the ratio of conductivity normal to the ellipsoid's axis of revolution ($\sigma_\perp$) to conductivity parallel to this axis ($\sigma_\parallel$) on the ellipsoid's semiaxis ratio in the case $\omega \ll v_F/R_\perp, v_F/R_\parallel$.

where the summation is performed over all indices from 1 to 3. To calculate the integral with respect to r', we direct the z'-axis along the vector $\boldsymbol{r}'$. Then, according to (159), t' is independent of the angle φ' (in the plane perpendicular to v'). Hence in (189) we can first integrate with respect to φ'. It can be shown that

$$\int_0^{2\pi} \mathrm{d}\varphi' x'_j x'_k = 2\pi r'^2 \left[\frac{v'_j v'_k}{v'^2} + \frac{\sin^2\theta'}{2}\left(\delta_{jk} - 3\frac{v'_j v'_k}{v'^2} \right) \right], \tag{190}$$

where θ' is the angle between $\boldsymbol{r}'$ and $\boldsymbol{v}'$.

After (190) is inserted into (189), the calculation becomes similar to one used in calculating expression (162) for the electric absorption. As a result, Eq. (189) becomes

$$W_\mathrm{m} = \frac{\pi e^2 m^3 R^5}{2(2\pi\hbar)^3} \mathrm{Re}\left\{ \frac{1}{\tilde{v}} \int \mathrm{d}^3 v\, \delta(\varepsilon - \mu) \left[\sum_{(1)}^{(3)} \frac{|\alpha_{ij}|^2}{\gamma_i^2 \gamma_j^2} v_i'^2 \psi_1(q) + 2 \sum_{(1)}^{(3)} \frac{|\alpha_{ij} + \alpha_{ji}|^2}{\gamma_i^2 \gamma_j^2} \frac{v_i'^2 v_j'^2}{v'^2} \psi_2(q) \right] \right\}, \tag{191}$$

where

$$\begin{aligned} \psi_1 &= \frac{8}{15} - \frac{1}{q} + \frac{4}{q^3} - \frac{24}{q^5} - 8\left(\frac{1}{q^3} + \frac{3}{q^4} + \frac{3}{q^5} \right) \exp\{-q\}\,, \\ \psi_2 &= \frac{2}{5} - \frac{1}{q} + \frac{8}{3q^2} - \frac{6}{q^3} + \frac{32}{q^5} - 2\left(\frac{1}{q^2} + \frac{5}{q^3} + \frac{16}{q^4} + \frac{16}{q^5} \right) \exp\{-q\} - \frac{3}{4}\psi_1(q)\,. \end{aligned} \tag{192}$$

Eq. (191) determines the magnetic absorption by a particle in general form for an arbitrary ratio of the bulk and surface contributions. For spherical particles, the last term on the right-hand side of Eq. (191) vanishes, since in this case $\alpha_{ij} = -\alpha_{li}$.

Information about the scattering mechanism is contained in the quantities $q = 2R\tilde{\nu}/v'$ and $\tilde{\nu} \equiv \nu - \mathrm{i}\omega$. From (191) we can obtain simple analytic expressions in the limits of pure bulk

scattering and pure surface scattering. In the first case ($|q| \gg 1$), we arrive at the known expression for magnetic absorption determined by the second and third terms on the right-hand side of Eq. (146). When surface scattering is dominant, the high-frequency case is the most interesting, since the eddy field E_{ed} is proportional to the frequency, with the result that the relative role of magnetic absorption grows with frequency. We therefore assume that $q_1 \ll 1$ and $q_2 \gg 1$. Then from (191) it follows that

$$W_m \approx \frac{\pi e^2 m^3 R^4}{4(2\pi\hbar)^3\omega^2}\int d^3v\,\delta(\varepsilon-\mu)\left(\sum_{(1)}^{(3)}\frac{|\alpha_{ij}|^2}{\gamma_i^2}v_i^2v' + \frac{1}{2}\sum_{(1)}^{(3)}|\alpha_{ij}+\alpha_{ji}|^2\frac{v_i^2v_j^2}{v'}\right). \tag{193}$$

Again, in the case of an ellipsoid of revolution, the integrals in (193) can easily be evaluated and we obtain

$$W_m \cong \frac{9}{128}V\frac{e^2nv_F}{mc^2}R_\perp\left[\varphi_\perp(H_\parallel^{(0)})^2 + \frac{R_\parallel^4}{(R_\perp^2+R_\parallel^2)^2}\Phi(H_\parallel^{(0)})^2\right]. \tag{194}$$

Here, in addition to the function $\varphi_\perp$ defined in (175), we have introduced a new function Φ:

$$\Phi = \begin{cases} \left(2-\dfrac{1}{4e_p^2}-e_p^2\right)\sqrt{1-e_p^2}+\dfrac{1}{2e_p}\left(1+\dfrac{1}{2e_p^2}\right)\arcsin e_p, & R_\perp < R_\parallel\ , \\ \left(2+\dfrac{1}{4e_p^2}+e_p^2\right)\sqrt{1+e_p^2}+\dfrac{1}{2e_p}\left(1-\dfrac{1}{2e_p^2}\right)\ln(\sqrt{1+e_p^2}+e_p), & R_\perp > R_\parallel\ . \end{cases} \tag{195}$$

For spherical particles (i.e., as $e_p \to 0$), the result obtained by Lesskin et al. [190] follows from (194):

$$W_m \approx \frac{3}{64}V\frac{e^2nv_F}{mc^2}R(H^{(0)})^2\ . \tag{196}$$

Eq. (194) acquires a simple analytic form for the limits of highly elongated and highly flattened ellipsoids:

$$W_m \approx \frac{9}{128}\frac{3\pi}{8}V\frac{e^2nv_F}{mc^2}R_\perp\left[\frac{1}{2}(H_\parallel^{(0)})^2+(H_\perp^{(0)})^2\right], \quad R_\perp \ll R_\parallel\ , \tag{197}$$

$$W_m \approx \frac{9}{128}V\frac{e^2nv_F}{mc^2}R_\parallel\left[\left(\frac{R_\perp}{2R_\parallel}\right)^2(H_\parallel^{(0)})^2+(H_\perp^{(0)})^2\right], \quad R_\perp \gg R_\parallel\ . \tag{198}$$

From (197) it follows that in the case of a highly elongated ellipsoid, the magnetic absorption is twice as high when the magnetic field is perpendicular to the axis of revolution than when it is parallel to it. The situation is similar for bulk scattering.

Earlier we estimated the relative contribution of the electric and magnetic terms of spherical particles to absorption (see Eq. (138)). Now, having the expressions for the electric (Eq. (174)) and

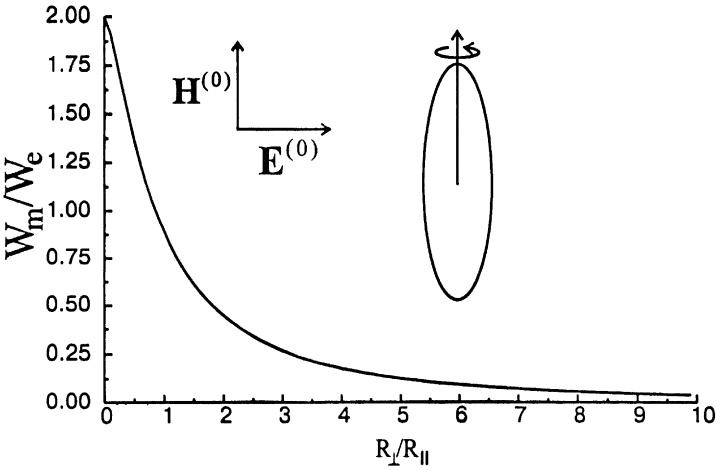

Fig. 7.5. Dependence of the magnetic-to-electric absorption ratio on the ellipsoids semiaxis ratio for the case when $H^{(0)}$ is parallel to major semiaxis.

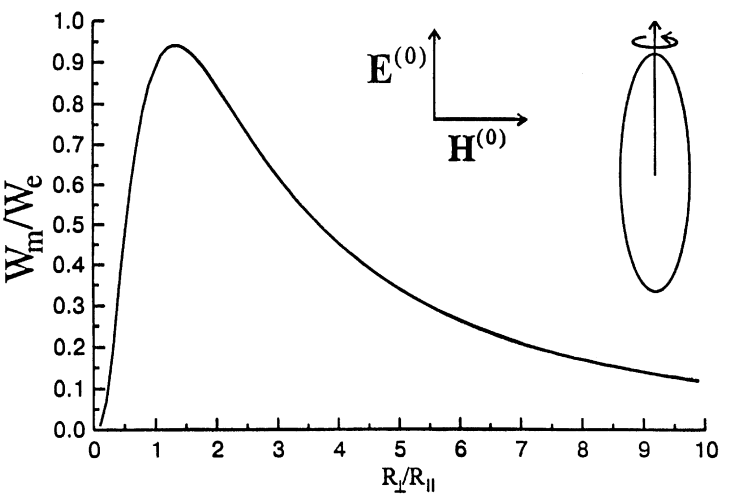

Fig. 7.6. Dependence of the magnetic-to-electric absorption ratio on the ellipsoids semiaxis ratio for the case when $E^{(0)}$ is parallel to major semiaxis.

magnetic (Eq. (194)) absorption by asymmetric particles, we can return to that problem. For an asymmetric particle, the ratio of the electric and magnetic contributions to absorption (at fixed frequency) is strongly dependent on the degree of particle asymmetry and wave polarization. Figs. 7.5 and 7.6 show the dependence of W_m/W_e on the ellipsoid semi-axial ratio for two different polarizations. It can be seen that these curves differ strongly not only quantitatively but also qualitatively.

Optical absorption in small metal particles and their arrays has also been investigated in a recent work [192]. A substantial dependence of the absorption on the size and shape of the particles has been found.

7.7. Quantum kinetic approach

As mentioned above, the majority of studies concerning the dependence of the optical conductivity on the shapes of metal particles have been performed in terms of quantum mechanics. This approach is necessary only for very small (1 nm) particles, when quantization of the electron spectrum must be taken into account. In all other cases, the quantum kinetic approach is only convenient when the solutions of the Schrodinger equation with the relevant potential wells are known.

Here we shall consider this approach briefly. It provides an opportunity to treat the absorption by small metal particles from a new point of view and to analyze the compatibility of the two treatments. Thus, we start from the equation for the statistical operator $\hat{\rho}$:

$$i\hbar\,\partial\hat{\rho}/\partial t = [\hat{H}\hat{\rho}] \ . \tag{199}$$

The Hamiltonian $\hat{H}$ for an electron in the electromagnetic wave field described by the vector potential $\boldsymbol{A}$ is given by the standard expression

$$\hat{H} = \frac{1}{2m}\left(\hat{p} - \frac{e}{c}\boldsymbol{A}\right)^2 + U(\boldsymbol{r}) \equiv \hat{H}_0 + \hat{H}_1 \ , \tag{200}$$

where

$$\hat{H}_0 = \frac{\hat{p}^2}{2m} + U(\boldsymbol{r}), \quad \hat{H}_1 \cong -\frac{e}{2mc}(\hat{\boldsymbol{p}}\boldsymbol{A} + \boldsymbol{A}\hat{\boldsymbol{p}}) \ . \tag{201}$$

Here $\hat{H}_1$ is written in the linear approximation with respect to $\boldsymbol{A}$; $U(\boldsymbol{r})$ is the electron potential energy; $\hat{p}$ is the momentum operator.

If one considers only electric absorption, i.e., disregards the eddy currents, then the electric field within the metal particle may be treated with sufficient accuracy as spatially homogeneous (for wavelengths much greater than particle dimensions). The vector potential may be written as

$$\boldsymbol{A} = \boldsymbol{A}^{(0)}\mathrm{e}^{-i\omega t + \eta t} \ , \tag{202}$$

where η is the adiabatic parameter.

Operator $\hat{\rho}$ may be written as a sum of two terms

$$\hat{\rho} = \hat{\rho}_0 + \hat{\rho}_1 \ , \tag{203}$$

where $\hat{\rho}_0$ is the statistical operator of the system without electromagnetic wave, $\hat{\rho}_1$ is the correction to $\boldsymbol{A}$ linear with respect to $\hat{\rho}_0$.

We linearize Eq. (199) with respect to $\boldsymbol{A}$, rewrite it on the proper basis of $\hat{H}_0$ and thus obtain

$$(i\eta + \omega)\langle\alpha|\hat{\rho}_1|\beta\rangle = \langle\alpha|\hat{H}_1\hat{\rho}_0|\beta\rangle - \langle\alpha|\hat{\rho}_0\hat{H}_1|\beta\rangle + \langle\alpha|\hat{H}_0\hat{\rho}_1|\beta\rangle - \langle\alpha|\hat{\rho}_1\hat{H}_0|\beta\rangle \ . \tag{204}$$

On this basis we have

$$\hat{\rho}_0|\beta\rangle = f_\alpha|\beta\rangle, \quad \langle\alpha|\hat{H}_1\hat{\rho}_0|\beta\rangle = \langle\alpha|\hat{H}_1|\beta\rangle f_\beta \ ,$$

where f_α is the occupation function of the αth state, i.e.

$$f_\alpha = 2f(\varepsilon_\alpha) \equiv 2\{\exp[(\varepsilon_\alpha - \mu)/kT] + 1\}^{-1} \ . \tag{205}$$

In Eq. (205), f is the Fermi function, T is the temperature. We have taken into account that each state with energy ε_α can be occupied by two electrons with opposite spins.

Eq. (204) yields

$$\langle\alpha|\hat{\rho}_1|\beta\rangle = \frac{(f_\alpha - f_\beta)\langle\alpha|\hat{H}_1|\beta\rangle}{\varepsilon_\alpha - \varepsilon_\beta - \hbar\omega - \mathrm{i}\eta} = -\frac{e}{mc}\frac{f_\alpha - f_\beta}{\varepsilon_\alpha - \varepsilon_\beta - \hbar\omega - \mathrm{i}\eta}\boldsymbol{A}\langle\alpha|\hat{\boldsymbol{p}}|\beta\rangle \ . \tag{206}$$

The current density operator may be written as

$$\hat{J} = \frac{e}{V}\boldsymbol{v} = \frac{e}{V}\{\hat{\boldsymbol{r}}, \hat{\boldsymbol{H}}\} = \frac{e}{V}\left(\frac{\hat{\boldsymbol{p}}}{m} - \frac{e}{m}\boldsymbol{A}\right) \equiv \hat{J}_0 + \hat{J}_1 \ , \tag{207}$$

and the statistical average of the current density is given by

$$\begin{aligned}\boldsymbol{J} &= Sp(\hat{\rho}\hat{J}) \approx Sp\{\hat{\rho}_0\hat{J}_1 + \hat{\rho}_1\hat{J}_0\} \\ &= -\frac{e^2}{mc}n\boldsymbol{A} - \frac{e^2}{m^2cV}\sum_{a,b}\frac{f_\alpha - f_\beta}{\varepsilon_\alpha - \varepsilon_\beta - \hbar\omega - \mathrm{i}\eta}\langle\alpha|\boldsymbol{A}\hat{\boldsymbol{p}}|\beta\rangle\langle\beta|\hat{\boldsymbol{p}}|\alpha\rangle \ .\end{aligned} \tag{208}$$

The last equality was derived making use of Eq. (206) and the normalization relation for f_α, i.e.,

$$\sum f_\alpha = Vn \ . \tag{209}$$

We employ the relation between the wave electric field $\boldsymbol{E}_{\mathrm{loc}}$ and the vector potential $\boldsymbol{A}$ ($\boldsymbol{E}_{\mathrm{loc}} = \mathrm{i}(\omega/c)\boldsymbol{A}$) and write the general expression for the current density operator components, i.e.

$$J_k = \sum_{l'}\sigma_{kl'}E_{l',\,\mathrm{loc}} \ . \tag{210}$$

Then Eq. (208) yields the expression for the complex tensor

$$\sigma_{kl}(\omega) = \mathrm{i}\left(\frac{e^2n}{m\omega}\delta_{kl} + \frac{e^2}{Vm^2\omega}\sum_{\alpha,\beta}\frac{(f_\alpha - f_\beta)\langle\alpha|\hat{p}_k|\beta\rangle\langle\beta|\hat{p}_l|\alpha\rangle}{\varepsilon_\alpha - \varepsilon_\beta - \hbar\omega - \mathrm{i}\eta}\right) . \tag{211}$$

The relation between the complex conductivity tensor and the complex dielectric permittivity tensor is given by

$$\sigma_{kl}(\omega) = \delta_{kl} + \mathrm{i}(4\pi/\omega)\varepsilon_{kl}(\omega) \ . \tag{212}$$

Making use of the relation

$$\frac{1}{\varepsilon_\alpha - \varepsilon_\beta - \hbar\omega \mp \mathrm{i}\eta} = P\left(\frac{1}{\varepsilon_\alpha - \varepsilon_\beta - \hbar\omega}\right) \pm \mathrm{i}\pi\delta(\varepsilon_\alpha - \varepsilon_\beta - \hbar\omega)$$

(for $\eta \to 0$), we find from Eqs. (135), (210), and (211) that the electric absorption is described by

$$W_e = -\frac{\pi e^2}{2m^2\omega}\sum_{\alpha,\beta}(f_\alpha - f_\beta)|\langle\alpha|\hat{\boldsymbol{p}}\boldsymbol{E}_{\rm loc}|\beta\rangle|^2\delta(\varepsilon_\alpha - \varepsilon_\beta - \hbar\omega)$$

$$\equiv \frac{V}{2}\sum_{k=1}^{3}(\mathrm{Re}\ \sigma_{kk})|E^{(0)}_{k,\rm loc}|^2 \ . \tag{213}$$

The last relation is written in the coordinate system associated with the principal axes of the conductivity tensor. It may be applied to calculate the principal values of this tensor (real values of the complex conductivity tensor). To do this, we have to calculate the matrix elements $\langle\alpha|\hat{\boldsymbol{p}}\boldsymbol{E}_{\rm loc}|\beta\rangle$ on the proper basis of the Hamiltonian $\hat{H}_0$, i.e., to specify the model.

We shall consider the simplest model of a parallelepiped particle that was proposed in Ref. [180].

The wave functions and energy spectrum of an electron in a parallelepiped potential well with sides a_1, a_2, a_3 are given by the simple expressions

$$\alpha|\rangle = \psi_{n_1 n_2 n_3} = \sqrt{\frac{8}{n_1 n_2 n_3}}\sin\left(\frac{\pi n_1}{a_1}x\right)\sin\left(\frac{\pi n_2}{a_2}y\right)\sin\left(\frac{\pi n_3}{a_3}z\right), \tag{214}$$

$$\varepsilon_\alpha = \frac{\hbar^2\pi^2}{2m}\sum_{j=1}^{3}\frac{n_j^2}{a_j^2} \ . \tag{215}$$

The matrix elements of interest are readily calculated in terms of the wave functions (214).

If the state $\langle\alpha|$ is described by the set of quantum numbers $\{n_j\}$, and the state $|\beta\rangle$ by the set $\{n'_j\}$, then we find that

$$|\langle\alpha|\hat{p}_k|\beta\rangle|^2 = \frac{8\hbar^2}{a_k^2}\frac{n_k^2 n_k'^{\,2}}{(n_k^2 - n_k'^{\,2})^2}\{1 - (-1)^{n_k + n'_k}\}\delta_{n_j:n'_j}, \quad j \neq k \ . \tag{216}$$

Eq. (216) was derived within the context of the identity

$$\{(-1)^{n_k + n'_k} - 1\}^2 = 2\{1 - (-1)^{n_k + n'_k}\} \ .$$

Inasmuch as Eqs. (216) and (213) contain, respectively, the unit tensor $\delta_{n_j n'_j}$ and the δ-function, we find that

$$\varepsilon_\alpha - \varepsilon_\beta = \frac{\hbar^2\pi^2}{2ma_k^2}(n_k^2 - n_k'^{\,2}) = \hbar\omega \ . \tag{217}$$

Substituting Eq. (216) into Eq. (213) and making use of Eq. (217), we obtain

$$W_e = \frac{2\pi^5 e^2\hbar^4}{m^4\omega^3}\left\{\frac{|E^{(0)}_{x,\rm loc}|^2}{a_1^6}\sum_{n_1,\,n'_1} n_1^2 n_1'^{\,2}[1 - (-1)^{n_1 + n'_1}]\right.$$

$$\left.[f(\varepsilon_\beta) - f(\varepsilon_\beta + \hbar\omega)]\delta(\varepsilon_\alpha - \varepsilon_\beta - \hbar\omega) + \cdots\right\}. \tag{218}$$

Formula (218) gives only the absorption component proportional to $|E^{(0)}_{x,\rm loc}|^2$. The other components may be obtained by obvious interchanges of subscripts.

If the electron spectrum quantization is unessential, then we may employ the relation $p_k = \hbar(\pi n_k/a_k)$ and replace the sum entering (218) by an integral over the quasi-continuous

momentum. Thus, we obtain

$$W_e = \frac{Ve^2 2\sqrt{2m}}{\hbar^4(\pi m\omega)^3}\sum_{k=1}^{3}\frac{|E^{(0)}_{k,\mathrm{loc}}|^2}{a_k}\frac{1}{8}\int \mathrm{d}p\, p_k^2\sqrt{\frac{p_k^2}{2m}+\hbar\omega}[f(\varepsilon)-f(\varepsilon+\hbar\omega)]$$

$$\cong V\frac{e^2 n}{m\omega^2}\frac{3}{4}\sum_{k=1}^{3}\frac{v_F}{a_k}|E^{(0)}_{k,\mathrm{loc}}|^2\ . \tag{219}$$

The factor 1/8 before the integral, has appeared because integration over the region $p_k \geq 0$ was extended to all values of the vector $\boldsymbol{p}$. Moreover, when deriving Eq. (219) from Eq. (218), we replaced the periodic function $\{1-(-1)^n\}$ of the index n by its average value which is equal to one.

The case of essential quantization of the electron spectrum, as well as other details of the parallelepiped model, are considered in Ref. [180].

Let us now compare the approaches and solutions of this model with the results of other models. First, the optical conductivity in this model is also a tensor quantity (see Eq. (219)). Second, as follows from Eq. (166), the replacement of the frequency ν by the frequency tensor $(\frac{3}{2}v_F/a_1, \frac{3}{2}v_F/a_2, \frac{3}{2}v_F/a_3)$ in the high-frequency Drude case ($\omega \gg \nu$) formally results in expression (219). It appears to contradict the reasoning given when deriving formulas (180) and (181). However, no contradiction occurs: for the parallelepiped shape, $V/a_k = S_k$ is just the area of the surface perpendicular to kth component of the field $\boldsymbol{E}^{(0)}_{\mathrm{loc}}$. Therefore, the electric absorption that is described by Eq. (219) is proportional to the parallelepiped surface area.

The idea that for $\nu < v_F/R$ only electron–surface collisions are responsible for the electric absorption is confirmed by comparison of our results with the conclusions of Ref. [126] (see also Section 5). In works [122,126], a method was proposed which makes it possible to study inelastic reflection of electrons from the potential barrier and electron inelastic tunneling through the barrier. The electrons can either absorb or emit light quanta. The unified approach allows the consideration of the bremsstrahlung and inverse process, direct and inverse photoeffect, etc. In particular, the cross-section of the inelastic reflection from a potential wall perpendicular to the x-axis is given by [126]

$$D^{(\pm)}(\varepsilon_x) = \frac{2e^2|E^{(0)}_{x,\mathrm{loc}}|^2}{m\hbar^2\omega^4}\sqrt{\varepsilon_x(\varepsilon_x \pm \hbar\omega)}, \quad \varepsilon_x \equiv \frac{mv_x^2}{2}\ , \tag{220}$$

where signs $(+)$ and $(-)$, respectively, correspond to the absorption and emission of a quantum. (To avoid misunderstanding, we note that the authors of [126] employ a real vector potential, whereas the treatment in this section involves a complex vector potential.)

Making use of Eq. (220) we may write the energy absorbed by an electron gas scattered on a surface of area S_x:

$$W_x = \frac{2\hbar\omega S_x}{(2\pi\hbar)^3}\int_{p_x\geq 0}^{\infty}\mathrm{d}p_x\, v_x D^{(+)}(\varepsilon_x)\int_{-\infty}^{\infty}\mathrm{d}p_y\int_{-\infty}^{\infty}\mathrm{d}p_z f(\varepsilon)[1-f(\varepsilon+\hbar\omega)]$$

$$-\frac{2\hbar\omega S_x}{(2\pi\hbar)^3}\int_{\substack{\varepsilon_x\geq\hbar\omega\\ p_x>0}}\mathrm{d}p_x\, v_x D^{(-)}(\varepsilon_x)\int_{-\infty}^{\infty}\mathrm{d}p_y\int_{-\infty}^{\infty}\mathrm{d}p_z f(\varepsilon)[1-f(\varepsilon-\hbar\omega)]\ . \tag{221}$$

In the second term of Eq. (221) we introduce a shift $\varepsilon_x \to \varepsilon_x - \hbar\omega$ and take into account that $\mathrm{d}p_x v_x = \mathrm{d}\varepsilon_x$, $f(\varepsilon) f(\varepsilon - \hbar\omega) \to f(\varepsilon + \hbar\omega) f(\varepsilon)$; $D^{(-)}(\varepsilon + \hbar\omega) = D^{(+)}(\varepsilon_x)$.

Then the two terms of Eq. (221) may be combined and reduced to the form

$$W_x = \frac{\hbar\omega S_x}{(2\pi\hbar)^3} \int \mathrm{d}p_x \, v_x D^{(+)}(\varepsilon_x)[f(\varepsilon) - f(\varepsilon + \hbar\omega)] \, . \tag{222}$$

This expression, with the accuracy of the factor 1/2, reproduces formula (222) for $k = 1$. But since the parallelepiped has two surfaces S_x (the front and the back walls), the coincidence of the results obtained by means of the two approaches is obvious.

Inasmuch as only one surface was taken into account in Eq. (222), this formula could not contain the collision frequency of the type v_F/a_1. This is another argument that supports the above interpretation of Eqs. (180) and (181).

It is also instructive to compare the transversal conductivity of a strongly elongated ellipsoid ($R_\parallel > R_\perp$), calculated in this section, and of a cylindrical sample, calculated in [179]. According to (180) and (177), one has for the ellipsoid

$$\sigma_\perp \approx \frac{27\pi}{128} V \frac{ne^2}{m\omega^2} \frac{v_F}{R_\perp} = \frac{9}{32\pi} \frac{e^2}{R_\perp \hbar^3} \left(\frac{\mu}{\omega}\right)^2 . \tag{223}$$

For the cylindrical sample at $\mu \gg \hbar\omega$, calculations [179] give

$$\sigma_\perp \simeq \frac{3e^2}{\pi^3 R_\perp \hbar^3} \left(\frac{\mu}{\omega}\right)^2 . \tag{224}$$

It is seen that expressions (223) and (224) coincide to within a factor of $3\pi^2/32 \approx 1$, as should be expected in this limiting case ($R_\parallel \gg R_\perp$). It is recalled that formula (223) was obtained by a classical approach whereas formula (224) was derived quantum-mechanically (the discrete spectrum was replaced by continuous one only in the last stage of calculations).

7.8. Resonance plasma absorption of light in IMFs

Up to now, we have concentrated on the optical absorption by small metal particles in the IR range (i.e. far from the plasmon resonances), since our main goal was to explain the unusual phenomena observed while IMFs are exposed to a CO_2 laser beam. We recall such effects as electron emission (occurring in spite of the fact that the metal work function exceeds the energy of CO_2 laser quanta by a factor of ≈ 40) and light emission, which is distributed rather nonuniformly over the film and contains much more energetic quanta in its spectrum than those in the incident laser beam. To complement the physical picture of optical absorption in IMFs, we shall now briefly discuss some peculiarities of resonance absorption in small metal particles and their ensembles.

Some specifications are to be introduced at the beginning of this treatment. In Section 7.3, we have calculated the local electric field in the interior of a single metal particle placed within a medium with a dielectric constant $\varepsilon_m = 1$. The square of the modulus of this field is given by (141). In a more general case when $\varepsilon_m \neq 1$, formula (141) turns to

$$|(E_{Loc})_j|^2 = \frac{(E_j^{(0)})^2}{|\varepsilon_m + L_j(\varepsilon' - 1)|^2 + (L_j\varepsilon'')^2} \, . \tag{225}$$

This expression must be substituted for the first summand in (146), which characterizes the electric absorption. In the case when the particle dimension is smaller than the electron mean free path, it is also necessary to make the change

$$\varepsilon'' \to (4\pi/\omega)\sigma_{jj}(\omega) \ , \tag{226}$$

where $\sigma_{jj}(\omega)$ are the components of the optical conductivity tensor.

The plasma frequency is determined from the resonance condition

$$\varepsilon_{\mathrm{m}} + L_j(\varepsilon' - 1) = 0 \ . \tag{227}$$

The value ε' is given by formula (137), so condition (227) results in the following expression for the plasma frequencies:

$$\omega_{\mathrm{p}}^{(j)} = \frac{\omega_{\mathrm{p}}}{[1 - \varepsilon_{\mathrm{m}}(1 - 1/L_j)]^{1/2}} \ . \tag{228}$$

This expression shows that an ellipsoidal metal particle is characterized by three plasma frequencies corresponding to charge oscillations along three principal axes of the ellipsoid. As noted above, the electric absorption is given by the first summand in (146), which in the case $\varepsilon_{\mathrm{m}} \neq 1$ and with the account of (226) and (227) assumes the shape

$$\begin{aligned} W_{\mathrm{e}} &= V\frac{\omega\varepsilon''}{8\pi}\sum_{j=1}^{3}\frac{(E_j^{(0)})^2}{|\varepsilon_{\mathrm{m}} + L_j(\varepsilon' - 1)|^2 + (L_j\varepsilon'')^2} \\ &= V\frac{\omega\varepsilon''}{8\pi}\sum_{j=1}^{3}\frac{(E_j^{(0)})^2(\omega\omega_{\mathrm{p}}^{(j)})^4/\omega_{\mathrm{p}}^4 L_j^2}{(\omega^2 - \omega_{\mathrm{p}}^{(j)^2})^2 + \varepsilon''^{\,2}(\omega\omega_{\mathrm{p}}^{(j)})^4/\omega_{\mathrm{p}}^4} \ . \end{aligned} \tag{229}$$

It is seen that the electric absorption has maxima at the plasma frequencies (228). For particles smaller than the electron mean free path, the change (226) additionally modifies the shape of the plasma absorption peaks.

As one passes over from a single metal particle to an ensemble of such particles (e.g. an IMF), the absorption acquires some new important features. The localized electron density oscillations in separate particles possess oscillating dipole moments, which interact with each other and arrange themselves into collective modes. The simplest way of taking into account the interaction of the particles is to change the external field $\boldsymbol{E}^{(0)}$ in (140) by the sum of this field with the fields of all dipoles induced by it in the rest of the particles. The summation of the dipole fields can be easily carried out in various model geometries, e.g. for a system of identical ellipsoidal particles located in the points of a square lattice [189,193,194]. It has been shown that in such a case the Coulomb interaction can be formally considered through the change of the depolarization factor L_j in formulas (225) and (227)–(229) by an effective factor

$$L_j \to L_j - (V/4\pi)\beta_j \ . \tag{230}$$

The value β_j has been calculated in [189,193,194] and many other works (see also Appendix B). As can be seen from (228) and (219), the change (230) leads to a renormalization of the plasma frequencies and peak intensities.

It should be noted that a huge literature is devoted to plasma resonance absorption in dispersed systems (see e.g. [165,175,176,195] and references therein). We have briefly dwelt on this mechanism only to stress that a strong optical absorption by small metal particles is possible not only in the IR range considered in detail above, but in the visible range as well. Correspondingly, the nonequilibrium heating of electrons and phenomena accompanying it are also possible in this case. It should also be recalled that radiative decay of plasmons excited in the inelastic tunneling of electrons or by hot electrons seems to be one of the mechanisms responsible for the light emission from IMFs (Section 4).

7.9. Conclusions about optical absorption of small particles

In this section we have given expressions for electric and magnetic absorption by nonspherical particles smaller than the electron mean free path [178]. We have found that for small asymmetric particles, their electric and magnetic absorption can vary by several orders of magnitude under particle shape variations with the volume remaining constant. Such drastic variations in absorption can also occur under variations of wave polarization. Simple analytic formulas have been derived for highly elongated and highly flattened particle shapes.

We have also established that for nonspherical metal particles smaller than the electron mean free path, the light-induced conductivity is a tensor, in contrast to the Drude case. The components of the conductivity tensor have been found for particles in the form of an ellipsoid of revolution. We have studied the dependence of these components on the degree of particle asymmetry.

It should be emphasized that most theoretical investigations of the optical properties of island metal films were devoted to the mutual effect of the particles on local fields and electric absorption. In recent years the reflection of IR radiation from a layer of small metallic particles has also been studied (see, e.g., Ref. [196]). Allowance for the mutual effect of particles can indeed strongly influence the values of the local fields. Estimates have shown [188] that in favorable cases, allowance for this mutual effect can alter the local field inside a given particle severalfold. However, our results presented in this section show that allowing for particle shape together with considering the electric and magnetic absorption, can change the total absorption by several orders of magnitude. These factors, therefore, must be taken into account from the outset. These features of absorption are even more important in such phenomena as electron and phonon emission from island metal films illuminated by laser light. (The fact that absorption by small spherical particles is proportional to their surface area was reported earlier by Manykin et al. [174].) It is in such phenomena that the extreme cross sections of absorption by an ensemble of metal islands play a much more important role than the average (effective) cross sections.

8. Examples of applications of island metal films

Various phenomena and properties specific to IMFs have long been attracting many investigators who tried to develop new cathodes and sensors using these films. As usual in practical applications, high stability, reproducibility and economical efficiency of performance are the most important operational features to be attained in devices based on IMFs. The technological experience accumulated to date shows that these stringent requirements can be satisfied.

8.1. IMF cathodes

The phenomenon of electron emission induced by passing current through IMFs has been utilized to develop "cold" cathodes for vacuum microelectronic devices, which combine advantages of vacuum electronics (such as high thermal and radiation stability) and solid-state electronics with its as yet inexhausted potentialities of miniaturization. A considerable effort, especially in the Saratov plant of receiver-amplifier electron tubes, has been undertaken in the development of gold IMF cathodes activated by barium oxide [74,197]. A technology has been elaborated allowing the fabrication of such cathodes with an efficiency of 2–5 mA/W and the emission to conduction current ratio γ up to 5%. The emission current from a cathode cell sized $0.5\,\text{cm} \times 20\,\mu\text{m}$ at the working voltage 10–15 V amounted to tens of μA and was stable in the continuous operation mode for about 1000 h [74]. Such cathodes were exploited in indicating displays. A still higher efficiency has been achieved with IMF cathodes based on refractory metals [79,198,199]. For example, a Mo thin film cathode emitter sized $15\,\mu\text{m} \times 3\,\text{mm}$ produced a stable current up to 100 μA at $\gamma = 10$–15% [198]. However, a disadvantage of this cathode is a comparatively high working voltage of 50–80 V. It should be noted that IMF cathodes can be fed both by direct and alternating current.

A few types of triode cells using IMF cathodes have been proposed [200,201]. Quite good results have been obtained with comparatively simple cells depicted in Fig. 8.1a and b. A controlling electrode ("gate") and an anode were evaporated on a dielectric interlayer previously deposited on the contacts of the cathode. To reduce the leakage currents between the electrodes, the interlayer can be shaped by etching as shown in Fig. 8.1a. The anode current–voltage characteristic exhibits first a fast growth of the current with increasing voltage and then a leveling-off at the electric fields comparable to the average field within the film (Fig. 3.3). An effective control of the current can be achieved when the operating point is chosen in the steep section of the anode current–voltage curve.

8.2. A gold IMF microcathode

As noted above (Sections 2 and 3), electrons are not emitted uniformly from the whole island film, but rather come out from the emission centers having size $\leq 1\,\mu\text{m}$ and scattered over the film. This may complicate the focusing of electron beams obtained from the cathodes representing long and narrow films. A more expedient choice in this case is a point-like IMF microcathode [202]. An example of such a cathode fabricated on a pyroceram substrate with Mo contacts is shown in Fig. 8.2. The gap between the contacts was $20 \times 300\,\mu\text{m}^2$, and an Au film was evaporated into the gap as a strip only 20–30 μm wide. The work function of the film was reduced by a BaO overlayer. This cathode gave a stable electron emission at the level of 0.1 μA for a few thousand hours under technical vacuum. The half-width of the electron energy distribution was about 0.5 eV.

8.3. Electron emission from island films of LaB_6

Lanthanum hexaboride is a high-melting compound with metallic conductivity widely used as an effective electron emitter. LaB_6 films were evaporated in vacuum using the laser ablation technique. The substrates were glass plates with previously deposited Pt contacts. The gap between

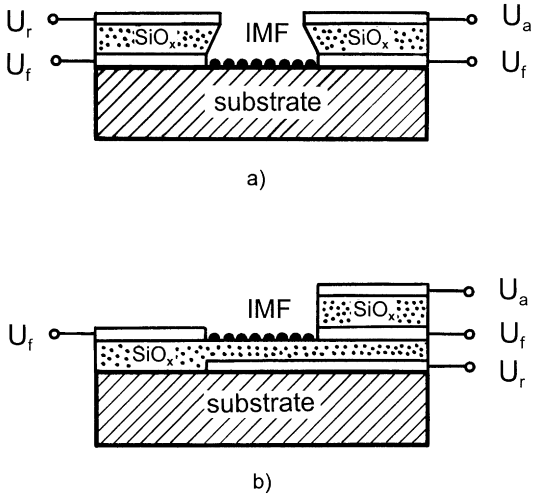

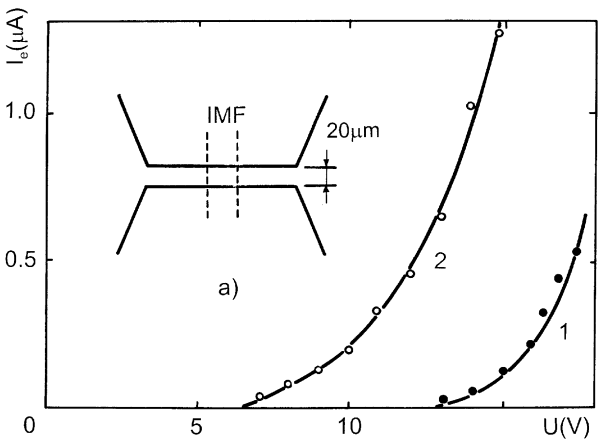

Fig. 8.1. Schematic of two triode cells with IMF cathodes. U_f is the voltage apllied to the film, U_a the anode voltage and U_r the regulating voltage.

Fig. 8.2. Electron emission current as a function of applied voltage for an Au film (1) and the same film covered with BaO (2). Inset (a) shows a typical configuration of the contacts and film in an IMF microcathode.

the contacts was 10 μm. The films had an island structure which rearranged in the course of electroforming and after this procedure their conduction current–voltage curves assumed a strongly pronounced nonlinear character [203], as in the case of island metal films. Simultaneously, electron emission set in. The examination of the LaB_6 film cathodes in an emission microscope showed that two distinct working regimes are possible, depending on the cathode structure. In one case the emission stems from small spots, as from IMFs. In another case it is more uniform. The reason for this is so far not clear. It is interesting that after a prolonged period of operation, the emission from the region near the negative contact considerably increases, probably due to electromigration of lanthanum toward this contact. On the whole, the LaB_6 film cathodes show a good stability. Their efficiency is an order of magnitude higher than that of clean Au IMF cathodes, but is considerably worse than the efficiency of the Au cathodes coated with BaO [74].

8.4. IMF cathodes with large emitting area

The emitting area of most cold cathodes (such as tip and MIM emitters, cathodes based on *p–n*-junctions, etc.) ranges from small fractions of μm^2 to mm^2. In order to increase the area, it is possible either to extend the emitter itself (e.g. by fabricating a larger MIM sandwich structure) or to create emitter arrays [204–206]. Each of these ways involves some specific difficulties, especially with regard to providing a sufficient uniformity of emission.

The problem of fabricating large-area IMF emitters is resolved rather easily. Recall that usually the IMF emitters represent a structure that consists of two contacts separated by a gap $\approx$ 10–20 μm wide and $\approx$ 5–10 mm long where an island film is formed. The emitting centers are

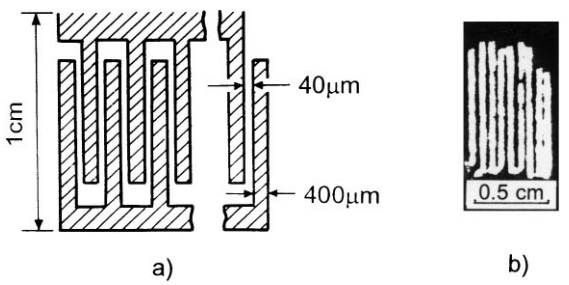

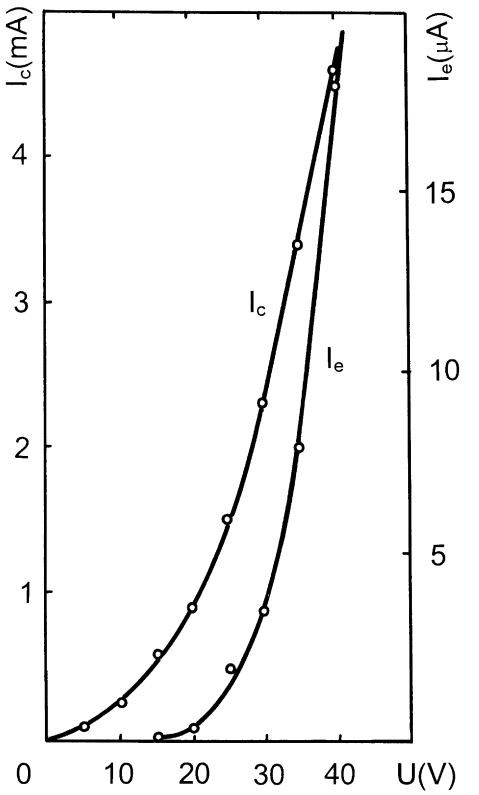

Fig. 8.3. A schematic of contact electrodes of an IMF cathode (a) and a cathodoluminescent image of emission distribution in this cathode (b).

Fig. 8.4. The current–voltage curves of conduction current I_c and emission current I_e for the cathode shown in Fig. 8.3.

located within a rather narrow ($\leq 1\,\mu m$) region which occupies only a small part of the gap. For this reason a mere widening of the gap cannot increase the emitting area.

There are two ways of creating large-area IMF emitters. The first of them is the fabrication of a long zig-zag-shaped cathode between two comb-like electrodes inserted into each other (Fig. 8.3a). The second possibility is to place a large number of microcathodes on one substrate, i.e. to make a cathode matrix.

In the former case one actually has a long IMF emitter which is put into a zig-zag form to make it compact and "two-dimensional". To this end, one first deposits the comb-like electrodes on a substrate and then the island film. After that the film is electroformed by applying a voltage about 15–20 V. The distribution of the emission centers can be judged from the luminescence of the cathode during its operation, because the centers of electron and light emission are known to coincide (see Section 2). The luminescence first appears in a few points of the cathode and then, as the voltage is increased up to 15–20 V, propagates along the entire length of the gap between the electrodes. An image of the emitting area of such a cathode obtained on a cathodoluminescent screen is given in Fig. 8.3b. Fig. 8.4 shows the conduction and emission current–voltage curves of

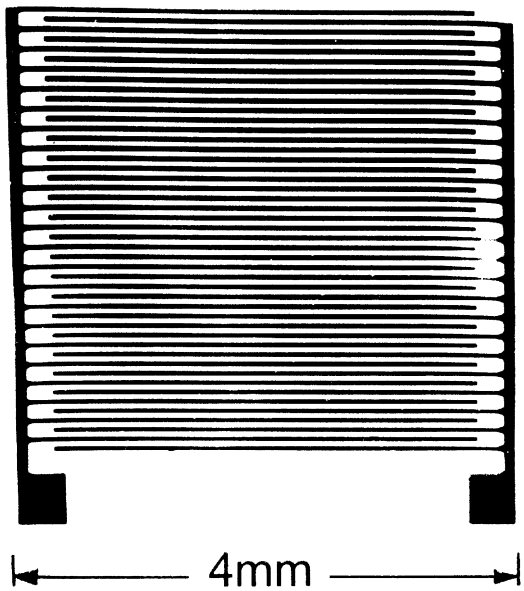

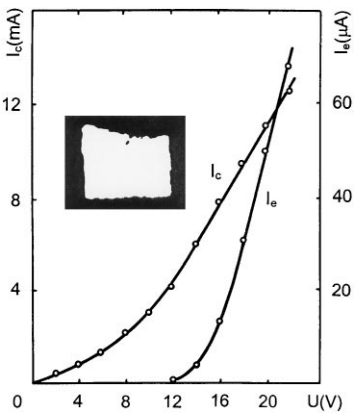

Fig. 8.5. An example of comb-like contact electrodes, prepared by photolithography, for large-area IMF cathodes. The gap between the "teeth" equals 12 μm.

Fig. 8.6. The current–voltage curves of conduction current I_c and emission current I_e for the large-area cathode with contact electrodes shown in Fig. 8.5. Inset: a cathodoluminescent image of emission distribution in this cathode.

a large-area IMF cathode in which the zigzag gap was prepared by scratching (using a needle) of a gold film evaporated on a glass substrate.

Such cathodes can easily be fabricated in various shapes, which is convenient e.g. for purposes of pictorial indication. The emitting regions in an electroformed IMF do not change their positions as the cathode is exposed to the atmosphere.

The characteristics presented above related to the large-area IMF cathodes prepared on transparent glass substrates, which are convenient for parallel observation of electron and light emission. However, the emitting strips in these cathodes were arranged at comparatively large distances apart ($\sim$ 0.1–0.3 mm). A more dense zigzag emitting structures were obtained on ceramic (pyroceram) substrates with Mo comb-like contacts fabricated by photolithography (Fig. 8.5) [207]. In this case the width of the gap was equal to 12 μm. The current–voltage curves of such cathodes are given in Fig. 8.6 and an example of the cathodoluminescent image of the emitting surface is reproduced in the inset.

Let us now consider some realizations of matrix IMF emitters. They consist of many elementary cathodes working in parallel. In an example illustrated in Fig. 8.7a and b each elementary cathode represents an island film filling a circular gap (50–60 μm wide) between two concentric electrodes [208]. The conduction and emission current–voltage characteristics of matrix IMF cathodes are similar to those of the zigzag cathodes (Fig. 8.4). Typically, the emission centers take up to 10–25% of the cathode geometrical surface. Fig. 8.7c shows the emission image of a matrix cathode having

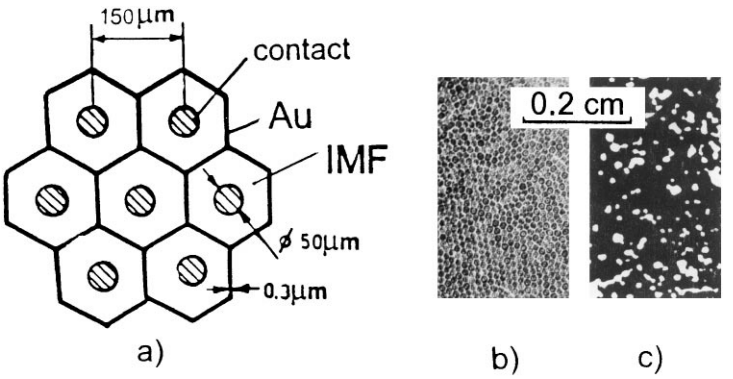

Fig. 8.7. (a) A schematic of a fragment of the matrix IMF cathode. (b) A micrograph of a section of such a cathode. (c) A cathodoluminescent image of emission distribution in this cathode.

a total diameter of about 25 mm. The total emission current extracted from this cathode amounted to 500–100 μA at the efficiency $\gamma = 0.6$–0.7%.

8.5. SnO_2 island film cathodes

A number of works have been devoted to the investigation of electron emission from SnO_2 island films [209–211]. In [209], SnO_2 films were deposited onto a polished quartz substrate using pyrolytic dissociation of SnO_4 at 450°C. The conductivity of the films was controlled through the addition of Sb and NH_4F. The geometry of the films is sketched in Fig. 8.8. To obtain electron emission, a procedure of electroforming (passing a current through the film) was necessary. Later experiments with such films showed that in the course of the electroforming the narrow part of the film was strongly heated and partially destroyed so that it finally acquired an island structure [211]. An important advantage of the SnO_2 films is the possibility of carrying out their electroforming in air. Typical dependences of the conduction and emission currents on the voltage applied to the film are depicted in Fig. 8.8. For the conduction current, this dependence can vary from close-to-linear to close-to-exponential, whereas for the emission current it is always close to exponential. The ratio of the emission current to the conduction current, i.e. the cathode efficiency γ, varies in the range from 1 to 50%. Thermionic emission from the film seems improbable, since the emission current is independent of the duration of the pulses applied to the film in the range from 1 to 1000 μs. The authors [210,211] supposed that the main physical mechanism in such cathodes may be field emission from the SnO_2 islands, although they did not exclude also that some contribution can stem from hot electrons in the islands. The cathodes were shown to give stable currents densities in the range from 1 to 10 A/cm^2 for hundreds of hours and to retain their emission characteristics after exposure to air.

Quite recently, island cathodes based on small particles of metal oxides have been utilized in flat information displays.

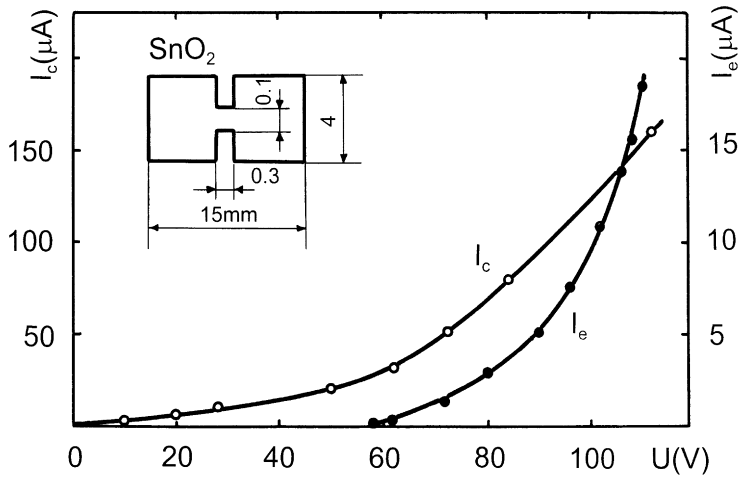

Fig. 8.8. The current–voltage curves of conduction current I_c and emission current I_e for a SnO_2 island cathode. Inset: geometry of the cathode [211].

8.6. Island film cathodes for flat information displays

Considerable attention has been focused in recent years on the development of flat cathodoluminescent displays. They possess high ergonomic characteristics in comparison with liquid crystal and other types of displays and are expected to take the place of bulky traditional kinescopes in many applications. Up to now, the main hopes have been pinned on arrays of field emitters of various configurations as the most promising cathodes for such displays (see e.g. [205,206]). However, quite recent publications of Japanese workers from Canon Research Center have presented a flat (9.6 mm thick) cathodoluminescent display using a cathode which they name "the surface conduction emitter" [13,212,213]. The emitter was fabricated of fine PdO particles, and its micrographs show that the size of the particles is about 5–10 nm, so it actually is an island film emitter (Fig. 8.9). To fabricate such emitters, an ink-jet printing process is carried out in air. A movable ink-jet head generates very small droplets of a PdO "ink" which are programmably placed onto a glass plate. An elementary emitter is ~ 10 nm thick and ~ 100 μm in size (Fig. 8.9). To activate the electron emission from as-deposited films, they are subjected to a forming procedure in which the voltage applied to the film is increased until the conduction current is almost broken irreversibly [212]. The authors suppose that this occurs due to partial melting of the PdO film. The result is a lowering of the driving voltage which must be applied to the cathode to obtain the electron emission. The ratio of the emission current to the conduction current is typically $\approx 0.2\%$ at the driving voltage 15 V and anode voltage 1 kV. In the range of the driving voltages from ≈ 13 to 17 V, the dependences of both emission and conduction current for one of the cathodes were found to be approximately linear when plotted in the Fowler–Nordheim coordinates. However, as noted in Section 3, such an observation cannot be considered as a sufficient proof of the field emission mechanism for these cathodes. Actually, the authors [213] consider a model in which electrons tunnel from one particle to another and then, after multiple elastic reflections from its surface, travel to the anode. However, the broad electron energy

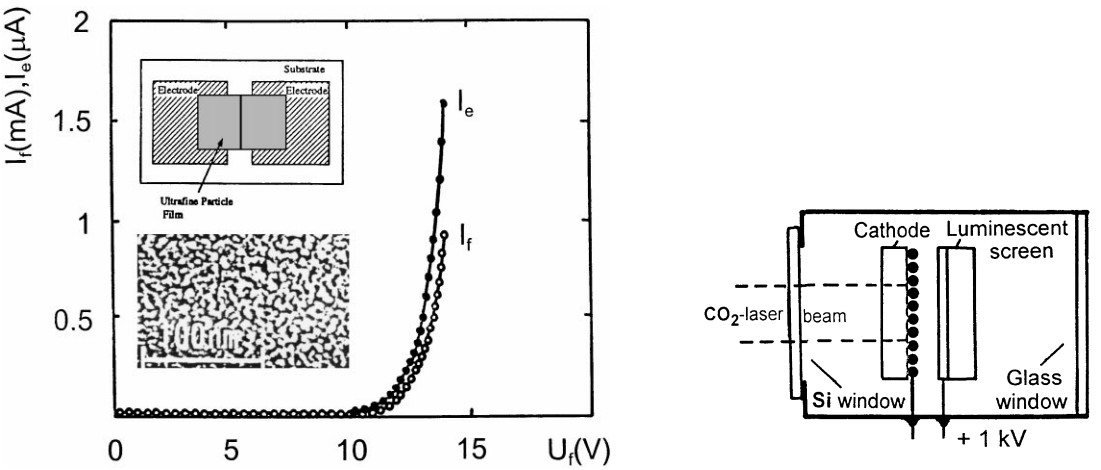

Fig. 8.9. The conduction current I_f and emission current I_e as functions of the voltage applied to the film consisting of ultrafine PdO particles. Insets: (a) schematic structure of the cathode, (b) an SEM image of the PdO film fired after ink-jet printing [13,212].

Fig. 8.10. A schematic of electron-optical image converter with an IMF cathode for recording and visualizing IR laser radiation.

distribution (with a width of $\approx 2\,eV$) recorded in the work can hardly be explained in the framework of this mechanism. In our opinion, the experimental results [213] are better compatible with the model of hot electrons discussed in this review. Contrary to [213], the model of hot electrons assumes that electrons after tunneling are not elastically reflected from the adjacent particle, but enter it and share their excess energy with other electrons heating them up.

The glass plate serving as a substrate for fabrication of a cathode matrix is previously coated with two systems of parallel metal wires ("column lines" and "row lines"), which are isolated from each other, perpendicular to each other and allow switching on of all the elementary emitters in turn. In this way an image can be displayed on the cathodoluminescent screen placed in vacuum parallel to the cathode matrix. The whole technology has been claimed to be quite simple, reproducible and economical. The authors [13] have succeeded to fabricate with this cathode a 10-in flat display which, in their words, "shows full color images as good as CRTs".

The coming years will probably show if the island film cathodes can rival other types of electron emitters in the new generation of flat information displays.

8.7. IMF cathodes for IR electron-optical converters

Island thin films have been used to develop a cathode for visualization and measurement of the spatial power distribution of pulse infrared laser radiation [9,214]. The cathode represents a gold IMF coating a dielectric substrate which is transparent to IR radiation (Fig. 8.10). The film consists of two subsystems of islands: the larger ones (0.1–0.5 μm) ensure an effective absorption of IR radiation (see Section 7) while the nanosized islands provide the conductivity in the cathode.

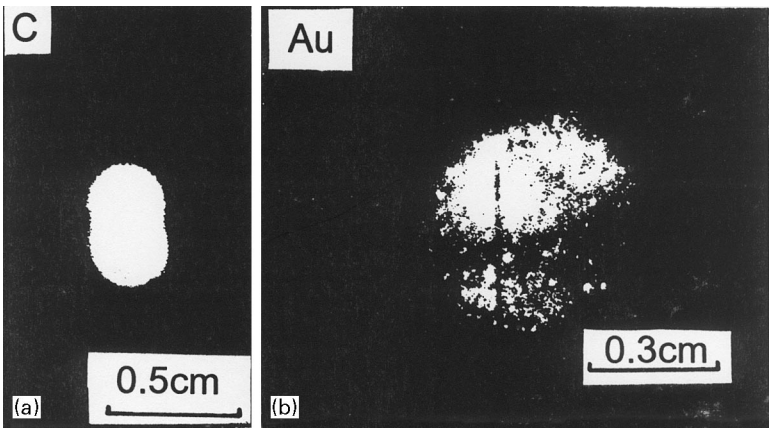

Fig. 8.11. Laser beam intensity distributions visualized by a carbon IMF (a) and a gold IMF (b). The dark strip in (b) corresponds to a cathode section where gold islands were absent. The laser power density was $P = 5 \times 10^5$ W/cm^2.

The known emitters used for the visualization of IR radiation represent matrices consisting of individual IR-sensitive elements [215]. In our case, each island is a functional analogue of the individual element of the matrix. In the island, there occurs a conversion of the energy of incident IR radiation into the energy of an electron gas, which results in electron emission. The spatial power distribution in the laser beam is mirrored in the distribution of the electron emission current density over the IMF cathode. Such an Au cathode prepared on a Si substrate has been tested with a pulsed CO_2 laser ($\lambda = 10.6\,\mu$m, $\tau = 1\,\mu$s). The density of the emission current amounted to 10^4–10^5 A/cm^2 at the laser power density 5×10^4 W/cm^2. The cathode reproduces the shape of nanosecond laser pulses [3].

Fig. 8.10 shows an electron-optical converter for visualization of IR radiation with the aid of an Au IMF emitter deposited on a Si plate. The IR beam from a CO_2 laser is introduced into the vacuum device through a Si window and is incident on the back side of the cathode. On passing the Si plate, it excites the electron gas in the islands and induces the electron emission. The emitted electrons are accelerated with a voltage of ~ 1 kV toward the cathodoluminescent screen to produce a visible image. Examples of such images are given in Fig. 8.11. It has been found that Au IMF emitters allow the visualization and characterization of IR laser beams at power densities of 5×10^4 to 10^6 W/cm^2. Utilizing a microchannel plate, it is possible to detect lower power densities and record photographically single IR radiation pulses. The spatial resolution of the IMF electron-optical converter is limited by the structure of the island film. The films prepared from refractory metals have been shown to sustain high power densities and provide a good reproducibility even after reception of $\sim 10^4$ powerful laser pulses.

8.8. Tensometric sensors

The high sensitivity of the resistance of IMFs to deformation of the substrate has been known since the 1960s [216,217]. Later on, a strong effect of the deformation of substrate on electron and photon emission characteristics was also found [75,154]. It is generally agreed that the high stress

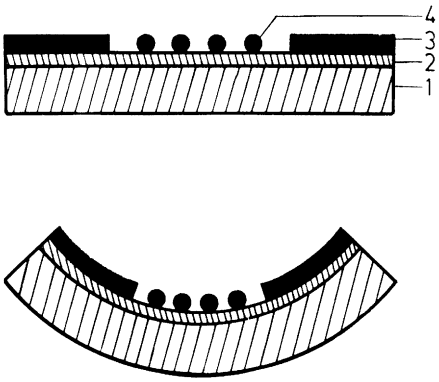

Fig. 8.12. Schematic of an IMF tensometric sensor. 1, a steel substrate, 2, an insulating sublayer, 3, contact electrodes and 4, an IMF.

sensitivity of IMFs is due to the tunnel mechanism of their conductivity. Thus the choice of appropriate film structure is very important to fabricate tensometric sensors with good performance.

The coefficient of tensosensitivity γ^*, or piezoresistance coefficient, is defined as

$$\gamma^* = (\Delta R/R)/(\Delta l/l) ,$$

where $\Delta R/R$ is the relative change of resistance and $\Delta l/l$ is the strain of the substrate. In the Ohmic region of the conduction current–voltage characteristic (up to the mean fields in the film of $\sim 10^4$–10^5 V/cm), γ^* is practically independent on the applied voltage. γ^* is very sensitive to the film structure and passes through a maximum at the mass thickness of 3–4 nm which in the case of gold IMFs corresponds to islands with an average size ~ 10 nm and the interisland spacings of ~ 2–3 nm [218].

An example of the design of an IMF tensometer is depicted in Fig. 8.12. The substrate was made of a 40 μm steel foil having a small residual strain and coated with a layer of polyurethane lacquer a few μm thick. Two contact electrodes with a 20 μm gap between them were deposited onto the lacquer coating and then an island film was evaporated in vacuum. To speed up the stabilization of the film structure, it is recommended to evaporate the IMF onto a heated substrate. Then the sample was exposed to air and coated with a protective dielectric film.

The conduction current–voltage curves of such sensors have a shape typical of the island films. The working point was chosen at 1–2 V which corresponded to the Ohmic segment of the curve. The resistance was 1–1.5 M for sensors with the best sensitivity ($\gamma^* = 80$–100 for Au films and $\gamma^* = 10$–30 for Ta, Cr, Mo and Pt films). The values of γ^* remain practically stable in time, but the resistance of the sensors increased by 15–20% over a few years.

Similar sensors shaped as membranes were fabricated on a 10 μm Lavsan substrate. They provided a reliable measurement of an excess pressure of a few millimeters of water column. Over 5 years, their resistance increased by not more than 20%.

To obtain the IMF tensometers with a higher sensitivity, one can use the effect of substrate deformation on the electron emission current [75] and light emission [154]. Such sensors were prepared on thin mica sheets, and γ^* values of 250–300 were attained.

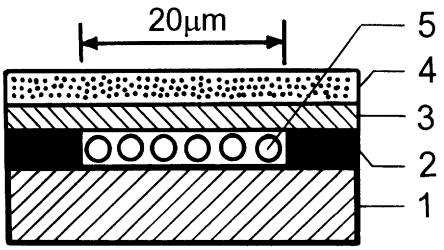

Fig. 8.13. Schematic of an IMF-based microsource of light. 1, a substrate, 2, contact electrodes, 3, a BaO film (12 nm thick), 4, a protecting SiO_x coating, 5, an IMF.

8.9. A microsource of light

The light emission from IMFs (see Section 4) has been utilized to fabricate a miniature source of light [219–221] (Fig. 8.13). The width of the contact electrodes on a dielectric substrate was taken 100 μm and the width of the gap between them 10 μm. An island film (of Au, Ag, Pt, Cu, Cr, Mo, or Bi) with a mass thickness of 6–8 nm was evaporated into the gap. Its electroforming was carried out in vacuum to obtain electron and light emission centers. Then all the centers save one were burnt by applying voltage pulses with an amplitude which is about twice as high as the working voltage. Then, to lower the working voltage, a thin layer of BaO was evaporated on the film and finally the whole structure was covered by a transparent protective SiO_2 coating. Such a point-like light source is quick-response, economical, save and can be exploited in air. The size of the luminous area is about 0.5 μm and its radiation power is $\sim 10^{-10}$ W within the spectral range 500–780 nm.

8.10. Hot electrons beyond IMFs

At this point it seems appropriate to discuss possible manifestations of hot electrons in other low-dimensional and dispersed systems.

First of all, it should be recalled that in many semiconductors, such as Ge, Si, InSb and others, the electron–phonon interaction is weak enough to ensure favorable conditions for intense generation of hot electrons in bulk materials. There is an abundant literature on this topic (see e.g. [109,110]). Taking into account the size effect in the electron–phonon interaction considered above, it can be anticipated that the conditions for nonequilibrium heating of electrons in small semiconductor particles should be even more favorable. Hot electrons are known to play an important part in semiconductor nanostructures [222].

The situation in metals is basically different and, as noted above, hot electrons can be generated under stationary conditions only in metal nanoparticles. In making the comparison of metals and semiconductors, it should be remembered that the concentration of free electrons in metals is by many orders of magnitude higher than in semiconductors. Correspondingly, various effects which can be stimulated by hot electrons should be much more intense in the case of metals.

Since the physical regularities underlying the heating of electrons in small particles seem to be rather general, effects similar to those observed in IMFs can be expected in other dispersed systems fed with energy. As an example in this context, let us mention recent works on "hot-electron

femtochemistry at surfaces" (see e.g. [223–228]). This term was coined for chemical reactions stimulated at surfaces by hot electrons that are generated in the substrate with the aid of powerful femtosecond laser pulses. Alternatively, it was proposed to obtain hot electrons for this purpose in metal–insulator–metal structures [228]. In the latter case one has a possibility to tune the energy of hot electrons to the energy of short-lived negative ion state of adsorbed species which is an important intermediate stage in the chemical reaction. Obviously, hot electrons generated in small particles can manifest themselves in similar chemical reactions which occur on dispersed surfaces such as e.g. supported catalysts. This is an example which demonstrates that exploitation of hot electrons may appear useful in the targeted development of various nanomaterials.

9. Conclusions

The whole body of currently available evidence on electron and photon emission phenomena in IMFs seems to be consistent with the model which predicts a strong nonequilibrium heating of the electron gas in nanoparticles. The size of such particles is smaller than the mean free path of electrons in the volume, so the scattering of electrons occurs mainly at the particle surface and the channel of electron energy losses due to generation of volume phonons is essentially cut off. The result is a strong reduction in the electron-lattice energy transfer, which provides a favorable possibility for generation of hot electrons when a sufficient power is fed into the particle. This can easily be realized by passing a current through the island film or by its laser irradiation. In the former case, the energy is delivered to the emission centers through narrow percolation channels where the current density is very high. In the latter case, the incident electromagnetic energy is absorbed very intensively when the particle has a special shape. The comparison of the theoretical predictions with experimental results shows that the electron emission from IMFs can be interpreted as Richardson emission of the hot electrons which have their own temperature different from that of the lattice. The light emission from IMFs can also have its origin in the appearance of hot electrons. Its possible mechanisms can be the bremsstrahlung, inverse surface photoeffect, radiation generated by inelastic tunneling of electrons between the islands and the radiative decay of plasma excitations. Thus, from the point of view of electronic kinetics, the metal island films are more similar to semiconductors and gas plasmas, where hot electrons occur universally, than to bulk metals where they can be generated only for very short times.

The application potential of IMFs, used so far only to a minor extent, ranges from microcathodes and microsources of light to large-area cathodes which seem promising for novel information displays. It is also appropriate to mention that hot electrons have been shown to play an important role in stimulation of surface chemical reactions ("hot-electron femtochemistry at surfaces"). Thus, a deep insight into mechanisms of generation of hot electrons in nanoparticles may appear useful to better understand the known chemical behaviour and potentialities of various dispersed systems (such as supported catalysts). Hot electrons have also an important impact in semiconductor nanostructures.

Hopefully, advances in nanotechnologies will open new possibilities in the preparation of the island films with more controllable parameters which in turn will ensure further progress in this interesting field of nanoscale science.

Acknowledgements

We are grateful to Professor G. Comsa for the invitation to write this review. This work was supported in part by the Ministry of Science and Technologies of Ukraine (grant # 2.4/790). A.G.N. also gratefully acknowledges the support in the framework of the International Soros Science Education Program through grant #SPU072041. We are indebted to Mrs. O.L. Fedorovich, Dr. M.V. Paliy, Dr. V.N. Bykov and Mr. O.E. Kiyayev for their help in preparation of the typescript.

Abbreviations

IMF – Island metal film
IR – Infra-red
MIM – Metal-insulator-metal
STM – Scanning tunneling microscopy
VCNR – Voltage-controlled negative resistance

Appendix A

The solution of the Schrödinger equation linearized with respect to the amplitude of the electromagnetic wave is represented as

$$\psi(\boldsymbol{r},t)=\psi^{(0)}(\boldsymbol{r})\mathrm{e}^{-(\mathrm{i}\varepsilon/\hbar)t}+\psi^{(1)}(\boldsymbol{r},t)\ , \tag{A.1}$$

where the first term gives the solution in the absence of the wave and the second term accounts for the contribution of the wave field. The function $\Psi^{(1)}(\boldsymbol{r},t)$ can be found from the equation

$$\mathrm{i}\hbar\frac{\partial\psi^{(1)}}{\partial t}-\left\{\frac{\hat{\boldsymbol{p}}^2}{2m}+U(x)\right\}\psi^{(1)}(z,t)=-\frac{e}{mc}(\boldsymbol{A}\hat{\boldsymbol{p}})\psi^{(0)}(\boldsymbol{r})\mathrm{e}^{-(\mathrm{i}\varepsilon/\hbar)t}\ . \tag{A.2}$$

Taking into account the time dependence of $\boldsymbol{A}(t)$ (29), we can write

$$-(\boldsymbol{A}\hat{\boldsymbol{p}})\psi^{(0)}(\boldsymbol{r})\mathrm{e}^{-(\mathrm{i}\varepsilon/\hbar)t}=\mathrm{i}\hbar(\boldsymbol{A}^{(0)}\boldsymbol{\nabla})\psi^{(0)}(\boldsymbol{r})\left\{\mathrm{e}^{-(\mathrm{i}/\hbar)(\varepsilon-\hbar\omega)t}+\mathrm{e}^{-(\mathrm{i}/\hbar)(\varepsilon+\hbar\omega)t}\right\}\ . \tag{A.3}$$

This relationship allows Eq. (A.1) to be represented as

$$\psi^{(1)}(\boldsymbol{r},t)=\mathrm{i}\frac{2e}{\hbar}\sum_{(+,-)}\boldsymbol{A}^{(0)}\Phi^{(\pm)}(\boldsymbol{r})e\ . \tag{A.4}$$

Equations for functions $\Phi_i^{(\pm)}$ can be obtained by substituting (A.4) into (A.2) and equating the terms that contain the same components $A_i^{(0)}$. In particular, the equation for $\Phi_i^{(\pm)}$ is

$$\left\{\Delta+\frac{2m}{\hbar^2}(\varepsilon\pm\hbar\omega-U_{(x)})\right\}\Phi_x^{(\pm)}=\frac{\partial}{\partial x}\psi^{(0)}(\boldsymbol{r})\ . \tag{A.5}$$

Consider now in more detail the case of a rectangular barrier along x having a width a_0 and height U (see Eq. (45)).

With this barrier, one obtains

$$\psi^{(0)}(\boldsymbol{r}) = \psi^{(0)}(x)\mathrm{e}^{\mathrm{i}k_y y + k_z z}$$

$$\equiv \mathrm{e}^{\mathrm{i}(k_y y + k_z z)}\begin{cases}\mathrm{e}^{\mathrm{i}k_x x} + R_0\mathrm{e}^{-\mathrm{i}k_x x}, & x \le 0\ ,\\ B_1\mathrm{e}^{\kappa_0 x} + B_2\mathrm{e}^{-\kappa_0 x}, & 0 \le x \le a_0\ ,\\ C_0\mathrm{e}^{\mathrm{i}k_1 x}, & x \ge a_0\ .\end{cases} \tag{A.6}$$

The coefficients R_0, B_1, B_2 and C_0 are determined from conditions of joining the function (A.6) and its derivatives in the points $x = 0$ and $x = a_0$. The procedure of the joining gives a system of algebraic equations which determine the unknown coefficients:

$$\begin{aligned} &1 + R_0 = B_1 + B_2\ ,\\ &\mathrm{i}k_x(1 - R_0) = \kappa_0(B_1 - B_2)\ ,\\ &B_1\mathrm{e}^{\kappa_0 a} + B_2\mathrm{e}^{-\kappa_0 a_0} = C_0\mathrm{e}^{\mathrm{i}k_x a_0}\ ,\\ &\kappa_0(B_1\mathrm{e}^{\kappa_0 a_0} - B_2\mathrm{e}^{-\kappa_0 a_0}) = \mathrm{i}k_x C_0\mathrm{e}^{\mathrm{i}k_x a_0}\ . \end{aligned} \tag{A.7}$$

Considering the structure of function (A.6), the dependence of $\Phi_x(\boldsymbol{r})$ on the variables y and z can be separated into an isolated factor:

$$\Phi_x(\boldsymbol{r}) = \varphi(x)\mathrm{e}^{\mathrm{i}(k_y y + k_z z)}\ . \tag{A.8}$$

The substitution of (A.8) into Eq. (A.5) gives

$$\begin{aligned} &\frac{\mathrm{d}^2\varphi}{\mathrm{d}x^2} + \frac{2m}{\hbar^2}(\varepsilon_x \pm \hbar\varpi)\varphi(x) = \mathrm{i}k_x(\mathrm{e}^{\mathrm{i}k_x x} - R_0\mathrm{e}^{-\mathrm{i}k_x x}), \quad x \le 0\ ,\\ &\frac{\mathrm{d}^2\varphi}{\mathrm{d}x^2} + \frac{2m}{\hbar^2}(\varepsilon_x \pm \hbar\varpi - U)\varphi(x) = \kappa_0(B_1\mathrm{e}^{\kappa_0 x} - B_2\mathrm{e}^{-\kappa_0 x}), \quad 0 \le x \le a_0\ ,\\ &\frac{\mathrm{d}^2\varphi}{\mathrm{d}x^2} + \frac{2m}{\hbar^2}(\varepsilon_x \pm \hbar\varpi)\varphi(x) = \mathrm{i}k_0 C_0\mathrm{e}^{\mathrm{i}k_x x}, \quad x \ge a_0\ . \end{aligned} \tag{A.9}$$

It can be easily checked by immediate substitution into (A.9) that its solution can be represented as

$$\varphi(x) = \pm\frac{\hbar}{2m\omega}\frac{\partial\psi^{(0)}(x)}{\partial x} + \varphi^{(\pm)}(x)\ . \tag{A.10}$$

Here the shape of $\varphi^{\pm}(x)$ is given by formula (46). The first term in (A.10) is a partial solution of the nonuniform system of equations (A.9) and $\varphi^{\pm}(x)$ gives a solution of the uniform system.

The conditions of joining the function (A.10) and its derivative in the points $x = 0$ and $x = a_0$ give a system of algebraic equations which determine the coefficients d, f_1, f_2, and g:

$$\begin{aligned} &d = f_1 + f_2 \ , \\ &f_1 e^{\gamma a_0} + f_2 e^{-\gamma a_0} = g e^{iqa_0} \ , \\ &(\gamma + iq) f_1 + (-\gamma + iq) f_2 = \mp \frac{U}{\hbar\omega}(B_1 + B_2) \ , \\ &(\gamma - iq) e^{\gamma a_0} f_1 - (\gamma + iq) e^{-\gamma a_0} f_2 = \mp \frac{U_0}{\hbar\omega} e^{ik_x a_0} C_0 \ . \end{aligned} \tag{A.11}$$

The probability of inelastic tunneling is determined by the coefficient g and that of the inelastic reflection from the barrier by the coefficient d.

Let us illustrate this statement for the case of tunneling. As can be seen from Eqs. (A.1), (A.4), (A.6),(A.8) and (A.10), the electron wave function at $x \to \infty$ is given by

$$\begin{aligned} \psi(\boldsymbol{r}, t) = C_0 e^{+ik_x} e^{i(k_y y + k_z z)} e^{-(i\varepsilon/\hbar)t} + i\left(\frac{2e}{c\hbar} A_x^{(0)}\right)\left\{\left(\pm \frac{\hbar}{2m\omega}\right) C_0 i k_x e^{ik_x x} + g e^{iqx}\right\} \\ \times e^{i(k_y y + k_z z)} e^{-(i/\hbar)(\varepsilon \pm \hbar\omega)t} \ . \end{aligned} \tag{A.12}$$

- It should be recalled that the summands $\Phi_y^{(\pm)}(\boldsymbol{r})$ and $\Phi_z^{(\pm)}(\boldsymbol{r})$ do not contribute to the inelastic current if the dispersion of the electromagnetic wave is not considered. By substitution of function (A.12) into expression (41) for the current I_x we obtain

$$I_x = \frac{e\hbar k_x}{m}|C_0|^2 + \frac{e\hbar}{m}\left(\frac{2eA_x^{(0)}}{mc}\right)^2 \left\{q|g|^2 + \frac{1}{4}\frac{\hbar k_x}{m\omega}\left[\pm \frac{\hbar k_x}{m\omega} + 1\right]|C_0|^2\right\} . \tag{A.13}$$

The cross-contribution of the first and second terms in (A.12) to the current vanishes when averaged over the wave period. The first summand in (A.13) determines the probability of the elastic tunneling. In the braces, the first term accounts for the probability of the inelastic tunneling while the second one gives a correction to the probability of the elastic tunneling due to the presence of the wave field.

The intelastically reflected current can be calculated similarly to (A.13). In this case, $|d|^2$ appears instead of $|g|^2$ in the expression for the current. The coefficients g and d are found from (A.11) with allowance for (A.7). The expression for $|g|^2$ is given by (48). For $|d|^2$, we obtain

$$\begin{aligned} |d|^2 = 4\left(\frac{U}{\hbar\omega}\right)^2 \frac{k_x^2}{G(\kappa_0, k_x)G(\gamma, q)}\{[\gamma\kappa_0 - \gamma\kappa_0 \operatorname{ch}\gamma a_0 \operatorname{ch}\kappa_0 a_0 + qk_x \operatorname{sh}\gamma a_0 \operatorname{sh}\kappa_0 a_0]^2 \\ + [\gamma k_x \operatorname{ch}\gamma a_0 \operatorname{sh}\kappa_0 a_0 + (\kappa_0 q \operatorname{ch}\kappa_0 a_0 \operatorname{sh}\gamma a_0)]^2\} \ . \end{aligned} \tag{A.14}$$

The calculation method presented above can easily be generalized for the case of an asymmetric barrier.

Appendix B

As suggested in Section 7, the mutual effect of metal islands on the local field strength in a given island can be formally accounted for by replacing the depolarization factor L_j with $L_j - \Delta L_j$. Below, we will find the explicit form of ΔL_j for a particular model.

It should be noted that the problem of the exact determination of the local field presents considerable difficulties even in the simplest case of two identical spherical particles (see e.g. [229,230]). Usually, an approximation is applied in which the electrostatic potential induced by an island is expanded as a power series in multipoles. As a rule one restricts the consideration to the lowest multipoles (most often, the dipoles). Such an approximation is not very appropriate for an island film in which the distance between the islands is of the same order as their size. In what follows we describe a method of the calculation of the local field which does not apply the multipole expansion [231].

Consider a linear periodic chain consisting of identical metal islands. The mutual effect of the islands on each other will be maximum when the external electric field $\boldsymbol{E}$ is parallel to the chain axis. We assume just such an orientation of the field. Since both the size of the islands and spacings between them are in our case much smaller than the length of the incident wave, the problem of the determination of the resulting field reduces to the solution of the Laplace equation with appropriate boundary conditions:

$$\begin{aligned} &\Delta\varphi_{\mathrm{e}}(\boldsymbol{r}) = 0 \ , \\ &\varphi_{\mathrm{e}}^{(+)}(\boldsymbol{r})|_{\mathrm{s}} = \varphi_{\mathrm{e}}^{(-)}(\boldsymbol{r})|_{\mathrm{s}} \ , \\ &\varepsilon\left(\frac{\partial\varphi_{\mathrm{e}}^{(+)}}{\partial\boldsymbol{n}}\right)\Bigg|_{\mathrm{s}} = \left(\frac{\partial\varphi_{\mathrm{e}}^{(-)}}{\partial\boldsymbol{n}}\right)\Bigg|_{\mathrm{s}} \ . \end{aligned} \tag{B.1}$$

The signs $(+)$ and $(-)$ correspond here to the limiting values of the function φ_{e} inside and outside the surface S, respectively, and $\boldsymbol{n}$ is the outward normal to it. The dielectric susceptibility of the medium is taken equal to 1, and that of the islands to ε.

The solution of Eq. (B.1) can be represented as

$$\varphi_{\mathrm{e}}(\boldsymbol{r}) = -\boldsymbol{E}\boldsymbol{r} + \sum_{k=-\infty}^{\infty} \int \frac{\mathrm{d}s\,\rho_{\mathrm{s}}(\boldsymbol{r})}{|\boldsymbol{r} - \boldsymbol{r}' - \boldsymbol{a}k|} \ . \tag{B.2}$$

Here $\rho_{\mathrm{s}}(\boldsymbol{r})$ is the surface charge density which, with the account for the assumed periodicity of the chain, obeys the following integral equation [232]:

$$\rho_{\mathrm{s}}(\boldsymbol{r}) + \frac{1-\varepsilon}{1+\varepsilon}\int \mathrm{d}s\,\rho_{\mathrm{s}}(\boldsymbol{r}) \sum_{k=-\infty}^{\infty} \frac{\cos\theta_k}{2\pi|\boldsymbol{r} - \boldsymbol{r}' - \boldsymbol{a}k|^2} = -\frac{1}{2\pi}\frac{1-\varepsilon}{1+\varepsilon}\boldsymbol{E}\boldsymbol{n} \ . \tag{B.3}$$

θ_k is the angle between the vectors $\boldsymbol{r} - \boldsymbol{r}' - \boldsymbol{a}k$ and $\boldsymbol{n}_{r'}$, where $\boldsymbol{n}_{r'}$ is the outward normal to the surface in the point $\boldsymbol{r}'$ and $\boldsymbol{a}$ is a vector connecting the centers of two adjacent islands. The direction of the vector $\boldsymbol{a}$ to one or another side along the chain plays no role, since the summation is carried out over all k's.

Eq. (B.3) has an exact solution for the case of a sungle island, i.e. for $k = 0$ (or $a \to \infty$):

$$\rho_s = \frac{3}{4\pi}\frac{\varepsilon - 1}{\varepsilon + 2}\boldsymbol{E}\boldsymbol{n} \ . \tag{B.4}$$

The substitution of (B.4) into (B.2) with retaining only $k = 0$ gives the known result for a dielectric sphere in a uniform external electric field. It will be recalled once again that at frequencies much lower than the plasma frequency, a conducting metal island behaves as a dielectric.

In a linear chain of identical spherical islands, the surface charge density $\rho_s(\boldsymbol{r})$ depends only on the angle θ between the field $\boldsymbol{E}$ and the radius vector $\boldsymbol{r}$ in the point on the sphere surface. Therefore ρ_s can be expanded in the general case into a series

$$\rho_s = \sum_{m=1}^{\infty} C_m P_m(\cos\theta) \ . \tag{B.5}$$

As it is clear from the symmetry considerations, Eq. (B.5) contains only odd Legendre's polynomials. By substitution of (B.5) into (B.3), multiplying the result by $P_n(\cos\theta)\sin\theta$ and then by integration over all θ's, one obtains a system of algebraic equations which determine the unknown coefficients C_m:

$$\sum_{m=1}^{\infty}\left\{\frac{4}{(2m+1)(2n+1)}\frac{(n+m)!}{n!m!}\left(\frac{R}{a}\right)^{n+m+1}\sum_{k=1}^{\infty}\frac{1}{k^{n+m+1}}\right\}C_m$$
$$+\frac{1}{n(2n+1)}\left[\left(\frac{1+\varepsilon}{1-\varepsilon}\right)+\frac{1}{2n+1}\right]C_n = -\frac{E}{6\pi}\delta_{1,n} \ . \tag{B.6}$$

Here R is the island radius; besides, the indices m and n pass over odd numbers only. The sums over k's in (B.6) converge rapidly to unity. For example, $\sum_{k=1}^{\infty} 1/k^3 \approx 1.2$; $\sum_{k=1}^{\infty} 1/k^5 \approx 1.04$.

It can be easily found from Eq. (B.6) that when $a = 3R$, i.e. when the gap between the islands equals the island radius, the coefficient C_3 and all the subsequent ones are much smaller than C_1. The value of C_3 can be comparable to that of C_1 only in the case if the islands almost touch each other.

For a known charge distribution, the electrostatic potential can be found with the aid of Eq. (B.2). However, our problem is substantially simplified by the circumstance that it is sufficient to determine only the component of the local field inside the island normal to its surface. If the surface charge density is known, this component of the local fields is easily calculated from the boundary conditions:

$$\begin{aligned}(\boldsymbol{E}_i - \boldsymbol{E}_{Loc})\boldsymbol{n}_r &= 4\pi\rho_s(\boldsymbol{r}) \ , \\ \boldsymbol{E}_i\boldsymbol{n}_r &= \varepsilon\boldsymbol{E}_{Loc}\boldsymbol{n}_r \ .\end{aligned} \tag{B.7}$$

Here E_i is the field at the outward side of the island. It follows from (B.7) that

$$\boldsymbol{E}_{Loc}\boldsymbol{n}_r = 4\pi\rho_s/(\varepsilon - 1) \ . \tag{B.8}$$

The normal component of the local field will have its maximum value, equal to the full local field, when its direction coincides with that of the external field. It is just in this direction that the surface charge density induced by the field is maximum. This direction corresponds to $\theta = 0$ in expansion (B.5). In such a case

$$\rho_s|_{\theta=0} = \sum C_m \ . \tag{B.9}$$

By orienting n_r in Eq. (B.8) along the external field (i.e. taking $\theta = 0$), we obtain

$$E_{Loc} = \frac{4\pi}{\varepsilon - 1}\rho_s|_{\theta=0} = \frac{4\pi}{\varepsilon - 1}\sum_{m=1}^{\infty} C_m \ . \tag{B.10}$$

As noted above, the coefficient C_1 is much larger than C_3 and all the following coefficients even in the case when the gap between the adjacent islands is equal to the island radius. At larger gaps this tendency is all the more pronounced. Thus, one may retain in sum (B.10) only the coefficient C_1 which is determined by Eq. (B.6). As a result. one obtains from Eq. (B.10) the local field inside a metal island comprising a part of the periodic linear chain of identical islands:

$$E_{Loc} = E\left\{1 + (\varepsilon - 1)\left[\frac{1}{3} - \frac{4}{3}\left(\frac{R}{a}\right)^3 \sum_{k=1}^{\infty}\frac{1}{k^3}\right]\right\}^{-1} \ . \tag{B.11}$$

As the local field E_{loc} is rewritten in a standard shape

$$E_{Loc} = E\{1 + (\varepsilon - 1)[L = \Delta L]\}^{-1} \ , \tag{B.12}$$

its comparison with (B.11) gives $L = 1/3$ for a spherical island. The parameter ΔL for this situation is

$$\Delta L \approx \tfrac{4}{3}(R/a)^3 \ . \tag{B.13}$$

In a similar way one can consider a periodic chain of ellipsoidal islands. Suppose the islands are identical ellipsoids of revolution with their major axes oriented along the chain. Taking into account the explicit form of the right-hand side of (B.3), it is convenient to present the charge distribution over the ellipsoid surface as

$$\rho_s = \frac{(R_\perp R_\parallel)^{1/2}}{(R_\perp^2 \cos^2\theta + R_\parallel^2 \sin^2\theta)^{1/2}} \sum_{m=1}^{\infty} C_m P_m(\cos\theta) \ . \tag{B.14}$$

Here θ is the angle between the radius vector to a point at the surface and the major axis of the ellipsoid which coincides with the direction of the external fields; $R_\parallel$ and $R_\perp$ are the major and minor semiaxes of the ellipsoid. The coefficients C_m can also be found from a system of algebraic equations, similar to (B.6), which can be obtained in the same way as described above.

In the same approximation as that applied to derive Eq. (B.11), we find for the chain of ellipsoidal particles:

$$E_{Loc} = E\left\{1 + (\varepsilon - 1)\left[L_\parallel - \frac{4}{3}(1 - e_p^2)\left(\frac{R_\parallel}{a}\right)^3 \sum_{k=1}^{\infty}\frac{1}{k^3}\right]\right\}^{-1} \ , \tag{B.15}$$

where $L_{\|}$ is the depolarization factor, determined by formula (147), and $e_p^2 = 1 - R_{\perp}^2/R_{\|}^2$. The value a stands as before for the distance between the centers of the islands. For $\Delta L_{\|}$ we obtain the following expression from (B.15):

$$\Delta L_{\|} \approx \tfrac{4}{3}(1 - e_p^2)(R_{\|}/a)^3 \ . \tag{B.16}$$

If the gaps between the islands are very small, the values of the local fields can easily be determined more exactly by using (B.10) and retaining not only C_1, but also C_3 (and possibly C_5).

References

[1] P.G. Borziak, O.G. Sarbej, R.D. Fedorovich, Phys. Stat. Sol. 8 (1965) 55. ***
[2] L.I. Andreeva, A.A. Benditsky, L.V. Viduta, A.B. Granovskii, Yu.A. Kulyupin, M.A. Makedontsev, G.I. Rukman, B.M. Stepanov, R.D. Fedorovich, M.A. Shoitov, A.I. Yuzhin, Fizika Tverdogo Tela 26 (1984) 1519 (in Russian).
[3] A.A. Benditskii, L.V. Veduta, Yu.A. Kulyupin, A.P. Ostranitsa, P.M. Tomchuk, R.D. Fedorovich, V.A. Yakovlev, Izvestiya Akademii Nauk SSSR, Ser. Fiz. 50 (1986) 1634 (in Russian).
[4] A.A. Benditskii, L.V. Veduta, V.I. Konov, S.M. Pimenov, A.M. Prokhorov, P.M. Tomchuk, R.D. Fedorovich, N.I. Chapliev, V.A. Yakovlev, Poverkhnost Fiz. Khim. Mekh. No. 10 (1988) 48 (in Russian). ***
[5] D.A. Ganichev, V.S. Dokuchaev, S.A. Fridrikhov, Pisma v ZhTF 8 (1975) 386 (in Russian).
[6] P.G. Borziak, Yu.A. Kulyupin, Elektronnye Processy v Ostrovkovykh Metallicheskikh Plenkakh (Electron Processes in Island Metal Films), Naukova Dumka, Kiev, 1980 (in Russian). ***
[7] S.A. Nepijko, Fizicheskiye Svoistva Malykh Metallicheskikh Chastits (Physical Properties of Small Metal Particles), Naukova Dumka, Kiev, 1985 (in Russian). **
[8] H. Pagnia, N. Sotnik, Phys. Stat. Sol. (a) 108 (1988) 11. **
[9] R.D. Fedorovich, A.G. Naumovets, P.M. Tomchuk, Prog. Surf. Sci. 42 (1993) 189. *
[10] L.I. Maissel, R. Gland (Eds.), Handbook of Thin Film Technology, McGraw-Hill, New York, 1970.
[11] L.I. Maissel, in: Physics of Thin Films, Vol. 3, Academic Press, New York, 1966, p. 61.
[12] K.R. Lawless, in: G. Hass, R. Thun (Eds.), Physics of Thin Films, Vol. 4, Academic Press, New York, 1967.
[13] E. Yamaguchi, K. Sakai, I. Nomura, T. Ono, M. Yamanobe, N. Abe, T. Hara, K. Hatanaka, Y. Osada, H. Yamamoto, T. Nakagiri, J. Soc. Inform. Display 5 (1997) 345. **
[14] E. Bauer, H. Poppa, Thin Sol. Films 12 (1972) 167. **
[15] K.L. Chopra, Thin Film Phenomena, McGraw-Hill, New York, 1969.
[16] V.M. Ievlev, L.I. Trusov, V.A. Kholmiansky, Strukturnye prevraschenia v tonkikh plenkakh (Structure Transformations in Thin Films), Metallurgia, Moscow, 1982 (in Russian).
[17] L.I. Trusov, V.A. Kholmiansky, Ostrovkovye metallicheskiye plenki (Island Metal Films), Metallurgia, Moscow, 1973 (in Russian). *
[18] A. Barna, P. Barna, J. Pocza, Vacuum 17 (1967) 219.
[19] G. Honjo, K. Takeyanagi, K. Yagi, K. Kobayashi, Jpn. J. Appl. Phys. 2 (1974) 539.
[20] S.A. Nepijko, Mikroelektronika 5 (1976) 86 (in Russian).
[21] A. Barna, P. Barna, R. Fedorovich, H. Sugawara, D. Radnoczi, Thin Solid Films 36 (1976) 75.
[22] D. Leonard, M. Krishnamurthy, C.M. Reaves, S.P. Denbaars, P.M. Petroff, Appl. Phys. Lett. 63 (1993) 3203.
[23] J.M. Moison, F. Houzay, F. Barthe, L. Leprince, F. Andre, O. Vatel, Appl. Phys. Lett. 64 (1994) 196.
[24] P. Tognini, L.C. Andreani, M. Geddo, A. Stella, P. Cheyssac, R. Kofman, A. Miglori, Phys. Rev. B 53 (1996) 6992. *
[25] R. Kern, H. Niehus, A. Schatz, P. Zeppenfeld, J. George, G. Comsa, Phys. Rev. Lett. 67 (1991) 855. **
[26] E. Sondergard, R. Kofman, P. Cheyssac, A. Stella, Surf. Sci. 364 (1996) 467.
[27] M. Zinke-Allmang, in: M. Tringides (Eds.), Surface Diffusion: Atomistic and Collective Processes, Plenum Press, New York, 1997, p. 389. *
[28] G.R. Carlow, R.J. Barel, M. Zinke-Allmang, Phys. Rev. B 56 (1997) 12519.
[29] G. Rosenfeld, M. Esser, K. Morgenstern, G. Comsa, Mat. Res. Soc. Symp. Proc. 528 (1998) 111.
[30] G. Rosenfeld, K. Morgenstern, I. Beckmann, W. Wulfhekel, E. Laegsgaard, F. Besenbacher, G. Comsa, Surf. Sci. 401 (1998) 402–404.

[31] L. Haderbache, R. Garrigos, R. Kofman, E. Sondergard, P. Cheyssac, Surf. Sci. 411 (1998) L748. **
[32] G.R. Carlow, D.D. Petrovic, M. Zinke-Allmang, Appl. Surf. Sci. 704 (1998) 130–132.
[33] K.-H. Park, J.S. Ha, W.S. Yun, E.-H. Lee, Surf. Sci. 415 (1998) 320.
[34] V.I. Marchenko, A.Ya. Parshin, Sov. Phys. JETP 54 (1980) 129. **
[35] D. Andelman, F. Brochard, P.-G. De Gennes, J.-F. Joanny, Compt. Rend. Acad. Sci. Paris 301 (1985) 675. **
[36] J. Villain, A. Pimpinelli, Physique de la Croissance Cristalline, Eyrolles, Paris, 1995 (Chapter 15). **
[37] B.V. Alekseenko, R.D. Fedorovich, in: Ultradispersnye chastitsy i ikh ansambli (Ultradispersed Particles and Their Ensembles), Naukova Dumka, Kiev, 1982, p. 97 (in Russian).
[38] A. Blech, A. Sello, L. Gregor, in: Tekhnologia tonkikh plionok (Thin Film Technology), Sovetskoye Radio, Moscow, 1977 (in Russian).
[39] B.V. Alekseenko, P.M. Tomchuk, R.D. Fedorovich, Poverhnost, Fiz. Khim. Mekh. (USSR), 10 (1988) 42 (in Russian).
[40] S.K. Dey, G.D. Dick, J. Vac. Sci. Technol. 11 (1974) 97.
[41] B.V. Alekseenko, R.D. Fedorovich, Thin Sol. Films 92 (1982) 252. *
[42] G.I. Distler, V.P. Vlasov, Yu.M. Gerasimov, Dekorirovanie Poverkhnosti Tverdykh Tel (Decoration of Solid Surfaces), Nauka, Moscow, 1976 (in Russian).
[43] P.G. Borziak, Yu.A. Kulyupin, O.G. Sarbej, R.D. Fedorovich, Ukrain. Fiz. Zh. 14 (1969) 395.
[44] A.F. Bardamid, Yu.A. Kulyupin, K.N. Pilipchak, A.I. Shaldervan, Dispergirovannye Metallicheskiye Plenki (Dispersed Metal Films), Institute of Physics, Kiev, 1972 (in Russian).
[45] B.V. Alekseenko, R.D. Fedorovich, P.M. Tomchuk, Material Sci. 13 (3–4) (1987) 161. **
[46] F.M. d'Heurle, P.S. Ho, in: J.M. Poate, K.N. Tu, J.W. Mayer (Eds.), Thin Films Interdiffusion and Reactions, Wiley, New York, 1978, p. 243.
[47] P.S. Ho, T. Kwok, Rep. Prog. Phys. 52 (1989) 301. *
[48] A. Scorzoni, B. Neri, C. Caprile, F. Fantini, Mater. Sci. Rep. 7 (1991) 143.
[49] D.W. Malone, R.E. Hummel, Crit. Rev. Solid State Mater. Sci. 22 (1997) 199.
[50] M. Aguilar, A.I. Oliva, P. Quintana, Surf. Sci. 409 (1998) 501.
[51] H. Yasunaga, A. Natori, Surf. Sci. Rep. 15 (1992) 205.
[52] A.S. Sukharier, S.V. Zagrebneva, I.A. Sidorova, in: Dispergirovannye Metallicheskiye Plenki (Dispersed Metal Films), Institut Fiziki AN Ukr SSR, Kiev, 1972, p. 308 (in Russian).
[53] R.D. Fedorovich, O.E. Kiyayev, A.G. Naumovets, A.P. Ostranitsa, Abstracts of 3 International workshop on Electronic properties of metal/non metal microsystems, Kleinheubach, Germany, 1991, p. 81.
[54] B. Licznerski, A. Seweryn, Int. J. Electron. 73 (1992) 919.
[55] A.K. Ray, C.A. Hogarth, J. Electron. 57 (1984) 1. **
[56] J.E. Morris, in: B.W. Licznerski, A. Dziedzic (Eds.), Metal/Nonmetal Microsystem: Physics, Technology, and Applications, Proc. SPIE 2780, 1996, p. 64.
[57] R.M. Hill, Proc. Roy. Soc. A 309 (1969) 377. *
[58] J.E. Morris, T.J. Coutts, Thin Sol. Films 47 (1977) 1.
[59] N. Mostovetch, B. Vodar, in: Poluprovodnikovye Materialy (semiconductor materials), Izd. Inostr. Lit., Moscow, 1954, p. 338 (in Russian).
[60] C.A. Neugebauer, M.B. Webb, J. Appl. Phys. 33 (1962) 74. *
[61] M.N. Nifontoff, Compt. Rend. Acad. Sci. 237 (1963) 24.
[62] D.S. Herman, T.N. Rhodin, J. Appl. Phys. 37 (1966) 1594.
[63] T.E. Hartman, J. Appl. Phys. 34 (1963) 943.
[64] P.M. Tomchuk, R.D. Fedorovich, Fiz. Tverd. Tela 8 (1966) 3131; Sov. Phys. Solid State 8 (1966) 2510. ***
[65] M.N. Nifontoff, Compt. Rend. Acad. Sci. 236 (1953) 1538.
[66] R. Hrach, Int. J. Electronics 73 (1992) 1085.
[67] L. Eckertova, Phys. Stat. Sol. 18 (1966) 3. *
[68] A.A. Milgram, Chin-Shun Lu, J. Appl. Phys. 37 (1966) 4773.
[69] P.G. Borziak, D.B. Danko, R.D. Fedorovich, O.E. Kiyayev, A.G. Naumovets, Prog. Surf. Sci. 53 (1996) 171. **
[70] P.M. Tomchuk, R.D. Fedorovich, Fiz. Tverd. Tela 8 (1966) 276; Sov. Phys. Solid State 8 (1966) 226. ***
[71] W. Chen, H. Ahmed, J. Vac. Sci. Technol. B13 (1995) 2883.

[72] P.G. Borziak, O.E. Kiyayev, A.G. Naumovets, R.D. Fedorovich, Ukr. Fiz. Zhurn. 43 (1998) 1487 (in Ukrainian).
[73] G. Dittmer, Thin Sol. Films 9 (1972) 317.
[74] A.S. Sukharier, S.V. Zagrebneva, N.N. Ivanov, L.N. Timonina, Izv. Akad. Nauk SSSR, Ser. Fiz. 38 (1974) 302 (in Russian).
[75] Yu.A. Kulyupin, S.A. Nepijko, Fiz. Tverdogo Tela 17 (1975) 2747 (in Russian).
[76] Yu.A. Kulyupin, S.A. Nepijko, R.D. Fedorovich, Radiotekhnika i Elektronika, 20 (1975) 1898 (in Russian).
[77] Yu.A. Kulyupin, S.A. Nepijko, N.N. Sedov, V.G. Shamonia, Optik 52 (1978/79) 101.
[78] H. Pagnia, N. Sotnik, W. Wirth, Int. J. Electron. 69 (1990) 25.
[79] H. Araki, T. Hanawa, Vacuum 38 (1988) 31.
[80] Yu.A. Kulyupin, R.D. Fedorovich, A.S. Sukharier, in: M.I. Elinson (Ed.), Nenakalivaemye Katody (Nonheated Cathodes), Sovietskoye Radio, Moscow, 1974, p. 9 (in Russian).
[81] V.G. Dyukov, A.V. Emelyanov, N.N. Sedov, M.I. Kolomeytsev, Izvestiya Akad. Nauk SSSR, Ser. Fiz. 41 (1977) 891 (in Russian).
[82] Yu.A. Kulyupin, S.A. Nepijko, V.I. Styopkin, Izv. Akad. Nauk USSR, Ser. Fiz. 46 (1982) 2354 (in Russian). *
[83] P.G. Borziak, Yu.A. Kulyupin, S.A. Nepijko, Thin Solid Films 36 (1976) 235.
[84] P.G. Borziak, Yu.A. Kulyupin, S.A. Nepijko, V.G. Shamonya, Thin Solid Films 76 (1981) 359.
[85] L.V. Viduta, Yu.A. Kulyupin, Radiotekhnika i Elektronika 24 (1979) 823 (in Russian).
[86] Yu.A. Kulyupin, R.D. Fedorovich, Fiz. Tverdogo Tela 14 (1972) 3105 (in Russian).
[87] E.V. Klimenko, A.G. Naumovets, Sov. Phys. Sol. State 13 (1971) 25.
[88] A.G. Naumovets, Yu.S. Vedula, Surf. Sci. Rep. 4 (1985) 365. *
[89] A.S. Sukharier, S.V. Zagrebneva, V.M. Suchilin, V.M. Trusakov, Elektr. Tekhn., Ser. 5(2) (1969) 10 (in Russian).
[90] B.V. Alekseenko, R.D. Fedorovich, Structura i fizicheskije svojstva tonkikh plenok (Structure and Physical Properties of Thin Films), Uzhgorodskii universitet, Uzhgorod, 1977/78, p. 78 (in Russian).
[91] G.S. Kreynina, Soviet Phys. Radioengng. and Electron. 7 (1962) 1949.
[92] G. Dearnaley, A. Stoneham, D. Morgan, Rep. Progr. Phys. 33 (1970) 1129. *
[93] I. Emmer, Thin Solid Films 20 (1974) 43.
[94] H. Biderman, J. Plasek, Thin Solid Films 47 (1977) 3.
[95] H. Biderman, Vacuum 26 (1976) 513.
[96] M. Bischoff, H. Pagnia, Thin Sol. Films 29 (1975) 303. **
[97] B. Alekseenko, R. Fedorovich, Ukr. Fiz. Zhurn. 30 (1985) 1559 (in Russian).
[98] J.G. Simmons, J. Appl. Phys. 35 (1964) 2472. *
[99] B. Alekseenko, P. Tomchuk, R. Fedorovich, Izv. Akad. Nauk SSSR, ser. fiz. 50 (1986) 1601 (in Russian).
[100] A.P. Komar, A.A. Komar, Zhur. Tekhn. Fiz. 31 (1961) 231 (in Russian). *
[101] A.P. Komar, V.P. Savchenko, Fiz. Tverd. Tela 7 (1965) 759 (in Russian).
[102] I. Giaver, Surf. Sci. 29 (1972) 1.
[103] A.E. Owen, P.G. Le Comber, J. Hajto, M.J. Rose, A.J. Snell, Int. J. Electronics 73 (1992) 897.
[104] R. Blessing, H. Pagnia, Phys. Stat. Sol. B 110 (1982) 537. *
[105] M. Bischoff, H. Pagnia, J. Trickl, Int. J. Electron. 72 (1992) 1009.
[106] M. Bischoff, V. Olt, H. Pagnia, Thin Sol. Films 165 (1988) 49.
[107] M. Bischoff, Int. J. Electron. 70 (1991) 491.
[108] M. Borbous, H. Pagnia, N. Sotnik, Thin Solid Films 151 (1987) 333.
[109] E.M. Conwell, High Field Transport, Academic Press, New York, 1967. *
[110] V. Denis, Yu. Pozhela, Goryachie Elektrony (Hot Electrons), Mintis, Vilnius, 1971. *
[111] P.G. Borziak, O.G. Sarbej, R.D. Fedorovich, Fiz. Tverdogo Tela 6 (1964) 2249.
[112] M.S. Brodyn, V.N. Bykov, D.B. Danko, R.D. Fedorovich, A.A. Kipen, G.A. Naumovets, N.I. Yanushevskii, in: B.W. Licznerski, A. Dziedzic (Eds.), Metal/Nonmetal Microsystem: Physics, Technology, and Applications, Proc. SPIE 2780, 1996, 324.
[113] M.S. Brodyn, V.N. Bykov, D.B. Danko, R.D. Fedorovich, A.A. Kipen, G.A. Naumovets, N.I. Yanushevskii, Proc. MRS 405 (1996) 150.
[114] M.S. Brodyn, V.N. Bykov, D.B. Danko, R.D. Fedorovich, A.A. Kipen, G.A. Naumovets, N.I. Yanushevskii, Ukr. Fiz. Zhurn. 40 (1995) 933 (in Ukrainian).

[115] E.C. Boswell, M. Huang, G.D.W. Smith, P.R. Wilshaw, 8th Int. Vac. Microelectr. Conf. Technical Digest, EDS a. IEEE, Portland, OR, 1995, p. 37.
[116] J.R. Jessing, D.L. Parker, M.N. Weichold, 8th Inter. Vac. Microelectr. Conf. Technical Digest, IEEE, Portland, OR 1995, p. 32.
[117] Ph. Dumas, M. Gu, C. Syrykh, A. Hallimaoni, F. Salvan, J.K. Gimzewski, R.R. Schlittler, J. Vac. Sci. Technol. B 12 (1994) 2064.
[118] R.D. Fedorovich, A.G. Naumovets, A.P. Ostranitsa, P.M. Tomchuk, Int. J. Electron. 69 (1990) 179. **
[119] S.I. Anisimov, V.A. Benderskij, D. Farkash, Uspekhi Fiz. Nauk 122 (1977) 185 (in Russian).
[120] R.W. Schoenlein, W.Z. Lin, J.G. Fujimoto, Phys. Rev. Lett. 58 (1987) 1680.
[121] L.V. Viduta, O.E. Kiyayev, A.G. Naumovets, A.P. Ostranitsa, R.D. Fedorovich, Radiotekhnika i Elektronika 36 (1991) 1345 (in Russian); Sov. J. Common. Technol. Electron. 37 (1992) 98. *
[122] P.M. Tomchuk, Ukrain. Fiz. Zh. 24 (1979) 182 (in Russian). **
[123] S.A. Nepijko, S.A. Gorban, L.V. Viduta, R.D. Fedorovich, Int. J. Electron. 73 (1992) 1011.
[124] D.B. Danko, R.D. Fedorovich, A.V. Gaidar, V.N. Poroshin, Int. J. Electron. 73 (1992) 1005.
[125] A.A. Benditsky, L.V. Viduta, R.D. Fedorovich, V.A. Yakovlev, Abstracts of 12th All-Union Conference on High-Speed Photography, Photonics and Electronics of Fast Processes, Moscow, 1985, p. 196 (in Russian).
[126] E.D. Belotskii, P.M. Tomchuk, Surf. Sci. 239 (1990) 143. ***
[127] Yu.A. Kulyupin, K.N. Pilipchak, Phys. Stat. Sol. (a) 11 (1972) K15.
[128] T.-L. Hwang, S.E. Schwarz, R.K. Jain, Phys. Rev. Lett. 36 (1976) 379.
[129] J. Lambe, S.L. Mc Carthy, Phys. Rev. Lett. 37 (1976) 923.
[130] A. Adams, P.K. Hansma, Phys. Rev. B 23 (1981) 3597.
[131] E.M. Belenov, I.N. Kompanets, A.A. Krakhotkin, A.V. Lezhnev, I.A. Poluektov, Yu.M. Popov, S.I. Sagitov, E.M. Soboleva, A.V. Uskov, V.G. Tsukanov, Kvantovaya Elektronika 10 (1983) 729 (in Russian).
[132] J.R. Kirtley, T.N. Theis, J.C. Tang, D.J. Di Maria, Phys. Rev. B 27 (1983) 4601.
[133] P. Dawson, D.G. Walmsley, H. Quinn, A.J.L. Ferguson, Phys. Rev. B 30 (1984) 3164.
[134] R. Hrach, Thin Solid Films 15 (1973) 65.
[135] C. Barriac, P. Pinard, F. Davoine, Phys. Stat. Sol. 34 (1969) 621.
[136] R. Berndt, J.K. Gimzewski, P. Johansson, Phys. Rev. Lett. 67 (1991) 3796.
[137] R. Berndt, J.K. Gimzewski, Surf. Sci. 269/270 (1992) 556. *
[138] R. Berndt, A. Baratoff, J.K. Gimzewski, in: R.J. Behm, N. Garcia, H. Rohrer (Eds.), Scanning Tunneling Microscopy and Related Methods, NATO ASI Series E, vol. 184, Kluwer, Dordrecht, 1990, p. 269.
[139] J.H. Coombs, J.K. Gimzewski, B. Reihl, J.K. Sass, R.R. Schlitter, J. Microscopy 152 (1988) 325.
[140] R. Berndt, J.K. Gimzewski, R.R. Schlitter, Ultramicroscopy 42/44 (1992) 355.
[141] N. Venkateswaran, K. Sattler, J. Xhie, M. Ge, Surf. Sci. 274 (1992) 199. *
[142] T. Shimitsu, K. Kobayashi, M. Tsukada, Appl. Surf. Sci. 60/61 (1992) 454.
[143] A.W. McKinnon, M.E. Welland, T.M.H. Wong, J.K. Gimzewski, Phys. Rev. B48 (1993) 15250.
[144] R. Berndt, J.K. Gimzewski, Ann. Phys. 2 (1993) 133.
[145] R. Berndt, J.K. Gimzewski, P. Johansson, Phys. Rev. Lett. 71 (1993) 3493.
[146] R. Berndt, R. Gaisch, W.D. Schneider, J.K. Gimzewski, B. Reihl, R.R. Schlitter, M. Tschudy, Surf. Sci. 307–309 (1994) 1033.
[147] M.M.J. Bischoff, M.C.M.M. van der Wielen, H. Van Kempen, Surf. Sci. 400 (1998) 127.
[148] P. Borziak, I. Zapesochnyi, I. Konovalov, K. Pilipchak, Dispergirovanye Metallicheskiye Plenki (Dispersed Metal Films), Inst. Probl. Mater. AN Ukr. SSR, Kiev, 1976, p. 107 (in Russian).
[149] P. Borziak, I. Konovalov, Yu. Kulyupin, K. Pilipchak, Thin Solid Films 35 (1976) L9.
[150] M. Adelt, S. Nepijko, W. Drachsel, H.-J. Freund, Chem. Phys. Lett. 291 (1998) 425.
[151] P. Borziak, Yu. Kulyupin, Ukr. Fiz. Zhurn. 24 (1979) 214 (in Russian).
[152] S. Nepijko, R. Fedorovich, L. Viduta, D. Ievlev, W. Schulze, Ann. Physik, to be published.
[153] S. Nepijko, D. Ievlev, W. Schulze, Appl. Phys. A, submitted.
[154] S. Nepijko, W. Schulze, I. Rabin, L. Viduta, Ann. der Physik 7 (1998) 101.
[155] K.P. Charle, F. Frank, W. Schulze, Ber. Bunsenges. Phys. Chem. 88 (1984) 350.
[156] O.E. Kiyayev, A.G. Naumovets, B.V. Stetsenko, R.D. Fedorovich, Abstracts of Int. Conf. on Emission Electronics, New Methods and Technologies, Tashkent, 1997, p. 94 (in Russian).
[157] H.K. Henisch, Electroluminescence, Pergamon, Oxford, 1962. *

[158] I.K. Vereshchagin, Elektroluminescenciya Kristallov (Electroluminescence of Crystals), Nauka, Moscow, 1974 (in Russian). *
[159] Y.A. Ono, Electroluminescent Displays, World Scientific, Singapore, 1995. *
[160] S.I. Anisimov, Y.A. Imas, G.S. Romanov, Y.V. Chodyko, Powerful Radiation Effect on Metals, Nauka, Moscow, 1970, p. 272.
[161] B.B. Agrant, A.A. Benditskii, G.M. Gandelman, Sov. Phys. JETP 52 (1980) 27.
[162] Yu.K. Danileiko, A.A. Manenkov, V.S. Nechitailo, V.J. Khaimov-Malkov, Trudy FIAN SSSR (Proceedings of Physical Institute Acad. Sci. USSR) 101 (1998) 75 (in Russian).
[163] M.J. Buckingham, Proc. Phys. Soc. 66 (1953) 601. **
[164] V.I. Kaganov, I.M. Lifshits, L.V. Tanatarov, Sov. Phys. JETP 4 (1957) 173. **
[165] Yu.I. Petrov, Fizika Malykh Chastits (The Physics of Small Particles), Nauka, Moscow, 1982 (in Russian). **
[166] A.O. Govorov, W.R. Frank, S.A. Studenikin, Fizika Tverdogo Tela 40 (1998) 542 (in Russian).
[167] P.M. Tomchuk, in: Dispergirovanye Metallicheskiye Plenki (Dispersed Metal Films), Inst. Fiziki AN Ukr. SSR, Kiev, 1972, p. 238 (in Russian). *
[168] A.D. Davydov, Quantum Mechanics, Nauka, Moscow, 1968 [English Translation, Pergamon, Oxford, 1980].
[169] E.D. Belotskii, P.M. Tomchuk, Int. J. Electron. 73 (1992) 955.
[170] A. Kawabata, R. Kubo, J. Phys. Soc. Japan 21 (1966) 1765. ***
[171] A. Bohr, B.R. Mottelson, Nuclear Structure, Benjamin, New York, 1969.
[172] S.A. Gorban, S.A. Nepijko, P.M. Tomchuk, Int. J. Electron. 70 (1991) 485.
[173] R.D. Averitt, S.L. Westcott, N.J. Halas, Phys. Rev. B 58 (1998) 203. **
[174] E.A. Manykin, P.P. Poluektov, Yu.G. Rubezhnyi, Zh. Eksp. Teor. Fiz. 70 (1976) 2117; Sov. Phys. JETP 43 (1976) 1105.
[175] C.F. Bohren, D.R. Huffman, Absorption and Scattering of Light by Small Metal Particles, Wiley, New York, 1983. *
[176] U. Kreibig, M. Vollmer, Optical Properties of Metal Clusters, Springer, Berlin, 1995. *
[177] P.M. Tomchuk, Surf. Sci. 330 (1995) 350. **
[178] P.M. Tomchuk, B.P. Tomchuk, JETP 85 (1997) 360. ***
[179] R. Ruppin, H. Yaton, Phys. Stat. Sol. B 74 (1976) 647.
[180] D.M. Wood, N.W. Ashcroft, Phys. Rev. B 25 (1982) 6255. ***
[181] P.M. Tomchuk, Ukr. Fiz. Zhurn. 38 (1993) 1174 (in Ukainian).
[182] K. Uchida, S. Kaneco, S. Omi, C. Hata, H. Tanji, Y. Asahara, I. Ikushima, T. Tokizaki, A. Nakamura, J. Opt. Soc. Am. B 11 (1994) 7.
[183] P.K. Shukla, D.I. Mendis, T. Desai (Eds.), Advances in Dusty Plasmas, World Scientific, Singapore, 1997.
[184] B.M. Smirnov, Uspekhi Fiz. Nauk 167 (1997) 11.
[185] L.D. Landau, E.M. Lifshitz, Electrodynamics of Continuous Media, 2nd Edition, Pergamon Press, Oxford, 1960. *
[186] M.L. Levin, R.Z. Muratov, Zh. Tekh. Fiz. 38 (1968) 1623; Sov. Phys. Tech. Phys. 13 (1968) 1318.
[187] C. Pecharroman, J.E. Iglesias, Phys. Rev. B 49 (1994) 7137.
[188] E.D. Belotski, S.P. Luk'yanets, P.M. Tomchuk, Zh. Eksp. Teor. Fiz. 101 (1992) 163; Sov. Phys. JETP 74 (1992) 88. ***
[189] S. Yamaguchi, J. Phys. Soc. Japan 15 (1960) 1577. ***
[190] A.G. Lesskin, V.E. Pasterak, A.A. Yushkanov, Zh. Eksp. Teor. Fiz. 83 (1982) 310; Sov. Phys. JETP 56 (1982) 710.
[191] E.I. Austin, M. Wilkinson, J. Phys. Condens. Matter 5 (1993) 8451.
[192] V. Russier, M.P. Pileni, Surf. Sci. 425 (1999) 313. **
[193] S. Yamaguchi, J. Phys. Soc. Japan 17 (1962) 184. **
[194] T. Yamaguchi, S. Yosida, A. Kinbara, Thin Solid Films 18 (1973) 63.
[195] F. Stietz, M. Stuke, J. Viereck, T. Wenzel, F. Traeger, Surf. Sci. 389 (1997) L1153.
[196] A.Ya. Blank, A.Ya. Sharshanov, Fiz. Nizk. Temp. 21 (1995) 263 (in Russian).
[197] A.S. Sukharier, in: M.I. Elinson (Ed.), Nenakalivayemye Katody (Nonheated Cathodes), Sovietskoye Radio, Moscow, 1974, p. 39 (in Russian).
[198] P.G. Borziak, L.V. Viduta, P.E. Kandyba, D.P. Kolesnikov, A.D. Kostenko, Yu.A. Kulyupin, R.D. Fedorovich, V.G. Yyastrebov, Izv. Acad. Nauk SSSR, Ser. Fiz. 37 (1973) 2613 (in Russian).

[199] H. Araki, T. Hanawa, Thin Solid Films 158 (1988) 207.
[200] A.S. Sukharier, S.V. Zagrebneva, E.N. Petrov, V.M. Suchilin, V.M. Trusakov, Bulletin of Inventions of USSR, No 8, Certificate No 296179 (1971).
[201] A.S. Sukharier, S.V. Zagrebneva, V.A. Osipov, E.N. Petrov, V.M. Trusakov, B.L. Serebrjakov, Bulletin of Inventions of USSR, No 25, Certificate No 349044 (1972).
[202] R.D. Fedorovich, A.G. Naumovets, P.M. Tomchuk, 9th Intern. Conf. on Vacuum Microelectronics Digest, St Petersburg, 1996, p. 179.
[203] S.S. Ivanets, N.G. Nakhodkin, A.I. Novoselskaja, R.D. Fedorovich, Bulletin of Inventions of USSR, Certificate No 1271278 (1985).
[204] G.A. Vorobyov, V.V. Efimov, L.A. Troyan, S. Lubsanov, Abstr. 5th Symp. on nonheated cathodes, Tomsk, 1985, p. 240.
[205] C.A. Spindt, I. Brodie, L. Humphrey, E.R. Westerberg, J. Appl. Phys. 47 (1976) 5248. *
[206] P.R. Schwoebel, I. Brodie, J. Vac. Sci. Technol. B 13 (1995) 1391.
[207] R.D. Fedorovich, A.G. Naumovets, P.M. Tomchuk, Condensed Matter Physics, 7 (1996) 5. *
[208] L.V. Viduta, R.D. Fedorovich, Abstracts of the 16th All-Union Conference on Emission Elecronics, Makhachkala, 1976, p. 40 (in Russian).
[209] M.I. Elinson, A.G. Zhdan, G.A. Kudintseva, M.Ye. Chugunova, Radiotekhnika i Electronika 10 (1965) 1500 (in Russian). **
[210] V.V. Nikulov, G.A. Kudintseva, M.I. Elinson, L.A. Kosulnikova, Radiotekhnika i Electronika 17 (1972) 1471 (in Russian).
[211] G.A. Kudintseva, M.I. Elinson, in: M.I. Elinson (Ed.), Nenakalivayemye Katody (Nonheated Cathodes), Sovietskoye Radio, Moscow, 1974, p. 29 (in Russian). **
[212] K. Sakai, I. Nomura, E. Yamaguchi, M. Yamanobe, S. Ikeda, T. Hara, K. Hatanaka, Y. Osada, H. Yamamoto, T. Nakagiri, Proc. 16th Int. Display Res. Conf. (Euro Display 96) (1996) 569.
[213] A. Asai, M. Okuda, S. Matsutani, K. Shinjo, N. Nakamura, K. Hatanaka, Y. Osada, T. Nakagiri, Society of Information Display, Int. Symp. Digest Tech. Papers (1997) 127.
[214] A. Benditskii, D. Danko, R. Fedorovich, S. Nepijko, L. Viduta, Int. J. Electron. 77 (1994) 985.
[215] B.M. Singer, Patent USA No 3919555 (1975).
[216] R.L. Parker, A. Krinsky, J. Appl. Phys. 14 (1972) 2700.
[217] J.F. Morris, Thin Solid Films 11 (1972) 259.
[218] L.V. Viduta, A.P. Ostranitsa, R.D. Fedorovich, S. Chumak, Ultradispersnye chastitsy i ikh ansambli (Ultrdispersed Particles and Their Ensembles), Naukova Dumka, Kiev, 1982, p. 110 (in Russian).
[219] Yu.A. Kulyupin, K.N. Pilipchak, R.D. Fedorovich, Bulletin of Inventions of USSR, No 43, Certificate No 1193843 (1985).
[220] Yu.A. Kulyupin, K.N. Pilipchak, R.D. Fedorovich, Bulletin of Inventions of USSR, No 40, Certificate No 1279433 (1986).
[221] Yu.A. Kulyupin, K.N. Pilipchak, in: Dispergirovannye Metallicheskiye Plenki (Dispersed Metal Films), Institut Fiziki AN Ukr SSR, Kiev, 1972, p. 238 (in Russian).
[222] Jagdeep Shah (Ed.), Hot Carriers in Semiconductor Nanostructures: Physics and Applications, Academic, San Diego, 1992. **
[223] J.W. Gadzuk, L.J. Richter, S.A. Buntin, D.S. King, R.R. Cavanagh, Surf. Sci. 235 (1990) 317. *
[224] R.R. Cavanagh, D.S. King, J.C. Stephenson, T.F. Heinz, J. Phys. Chem. 97 (1993) 786.
[225] M. Brandbyge, P. Hedegard, T.F. Heinz, J.A. Misewich, D.M. Newns, Phys. Rev. B 52 (1995) 6042.
[226] R.G. Sharpe, St.J. Dixon-Warren, P.J. Durston, R.E. Palmer, Chem. Phys. Lett. 234 (1995) 354.
[227] J.W. Gadzuk, Surf. Sci. 342 (1995) 345.
[228] J.W. Gadzuk, J. Vac. Sci. Technol. A 15 (1997) 1520. *
[229] A. Goyette, N. Navon, Phys. Rev. B 13 (1976) 4320.
[230] R. Ruppin, J. Phys. Soc. Japan 58 (1989) 1125.
[231] E.D. Belotskii, P.M. Tomchuk, Int. J. Electronics 73 (1992) 915.
[232] D.Ya. Petrina, Zhurn. Vychislitelnoi matematiki i mat. fiziki 24 (1984) 709.